AN ABSTRACT OF THE THESIS OF

Nathan E. Harff for the degree of Doctor of Philosophy in Electrical and Computer Engineering presented on March 4, 1997. Title: Electron Transport in Coupled Double Quantum Wells and Wires

Redacted for Privacy

Abstract approved:

Stephen M. Goodnick

Redacted for Privacy

Jerry A. Simmons

Double quantum wells (QWs) provide an excellent platform for studying physics in coupled two-dimensional electron gases (2DEGs). Due to the coupling between the QWs, DQWs possess an extra degree of electronic freedom not found in single 2DEGs. Many new transport phenomena which result from this extra degree of freedom have been observed. The majority of the previous work has been with no applied magnetic fields or with a magnetic field perpendicular to the growth plane $B_{\perp}$. The present work focuses on DQWs subject to magnetic fields parallel to the growth plane $B_{||}$.

First, the conductance of closely coupled DQWs with $B_{||}$ is studied. $B_{||}$ shifts the momenta of electrons in one QW with respect to that of electrons in the other QW. Due to coupling , the two curves anticross and a partial energy gap opens. The Fermi surface now consists of a lens-shaped inner orbit and a peanut-shaped outer orbit. These distortions in the dispersion result in distortions in the density of states, electron effective mass, and other properties. Two features, a maximum followed closely by a minimum, are seen in the conductance as a result of this anticrossing. The density dependence of these features are examined and compared with theory. A small $B_{\perp}$ is added to measure the effective

mass through the temperature dependence of the magneto-resistance oscillations. The measured mass is in excellent agreement with the theoretically calculated mass.

Next, the resistance is studied in tilted magnetic fields. $B_{\|}$ distorts the Fermi surface and $B_{\perp}$ causes Landau level formation for both Fermi surface components. The magnetoresistance oscillations show complex beating as Landau levels from the two Fermi surface components cross the Fermi energy. A third set of oscillations, which result from magnetic breakdown, are also observed. These results are compared with a semiclassical calculation of the Landau level positions.

Finally, quantum wires and quantum point contacts on DQWs are investigated. Predicted anticrossings of the one-dimensional dispersion curves result in interesting transport effects in these devices. Difficulties in sample fabrication have prevented experimental verification of the predicted effects. However, techniques to overcome these difficulties are being developed.

Electron Transport in Coupled Double Quantum Wells and Wires

by

Nathan E. Harff

A THESIS

submitted to

Oregon State University

in partial fulfillment of
the requirements for the
degree of

Doctor of Philosophy

Completed March 4, 1997

Commencement June 1997

Doctor of Philosophy thesis of Nathan E. Harff presented March 4, 1997

APPROVED:

Redacted for Privacy

Co-Major Professor, representing Electrical and Computer Engineering

Redacted for Privacy

Co-Major Professor, representing Electrical and Computer Engineering

Redacted for Privacy

Head of Department of Electrical and Computer Engineering

Redacted for Privacy

Dean of Graduate School

I understand that my thesis will become part of the permanent collection of Oregon State University libraries. My signature below authorizes release of my thesis to any reader upon request.

Redacted for Privacy

Nathan E. Harff, Author

PREFACE AND ACKNOWLEDGMENTS

Several people have contributed directly to the success of this work. The individual contributions are as follows. The samples were grown by J. F. Klem, M. V. Weckwerth, L. N. Pfeiffer, and K. W. West. G. S. Boebinger was kind enough to provide the material grown by Pfeiffer and West, and also discussed the work of Chapter 5. The sample processing was mainly done by T. R. Castillo and W. E. Baca, with contributions by G. S. Boebinger and myself. The electron beam lithography for the QPCs in Chapter 6 was done by J. R. Wendt. I performed the majority of the measurements, with input from J. A. Simmons. The peanut mass measurements and the corresponding analysis were done by M. A. Blount. I did most of the data analysis, with guidance from J. A. Simmons. S. K. Lyo did all of the theoretical calculations, except for the gate bias dependence of the anticrossing features and the semiclassical calculation of the Landau level positions. The gate bias dependence model was developed by J. A. Simmons. I developed the semiclassical Landau level position calculations of Chapter 5. I am indebted to these people for their contributions to this work. All of the work presented here was done at Sandia National Laboratories in Albuquerque, NM.

A few people have greatly impacted my graduate career. Chief among them are my advisors, Professor Steve Goodnick, formerly at Oregon State University, and Dr. Jerry Simmons, a staff member at Sandia. Steve introduced me to magnetotransport measurements and taught me the theoretical basis of electron transport. Jerry was my research advisor and allowed me to work in his lab at Sandia. I am deeply indebted to Jerry for being my mentor and friend during my Ph. D. research. I would also like to thank two managers at Sandia; Tom Zipperian, for encouraging me to work with Jerry, and Tom Picraux, for allowing me to work in his organization.

Several others have helped make my stay at Sandia more rewarding. Ken Lyo took the time to discuss much of his theoretical work with me. Mark Blount, Jeong-Sun Moon, and Travis Eiles discussed many aspects of semiconductor physics with me and also listened to, and improved, my practice talks. Maxine Gallegos, Teresa Foster, Rita Wells, and Rebecca Romero helped with the endless paperwork. Over the years, Sally Samora, Pat Glarborg, and Gerry Lopez helped me with sample processing and patiently answered my questions about processing. I would like to thank these people for making my life at Sandia more enjoyable. I would also like to thank Associated Western Universities for the Laboratory Graduate Fellowship they bestowed upon me.

Other people have also contributed to this thesis indirectly. Many of these contributions have been in maintaining my mental health. I would like to thank my parents, Earl and Eileen, for encouraging me to get an education and for being patient when that took much longer than they expected. I also thank my girlfriend, Ramona Barr, for being so patient when I was working strange hours and when I was bouncing off the walls before giving talks. Tom Cooney helped me survive my last year of classroom work and the qualifying exam with at least a little of my sanity intact. Since then he has remained a great friend. I also thank Tom and Anu for taking such good care of me while I was in Oregon for my final defense. Finally, I would like to thank my soccer friends. They have helped make me and Ramona feel at home in Albuquerque.

TABLE OF CONTENTS

TABLE OF CONTENTS (Continued)

LIST OF FIGURES

LIST OF FIGURES (Continued)

LIST OF FIGURES (Continued)

LIST OF FIGURES (Continued)

LIST OF TABLES

ELECTRON TRANSPORT IN COUPLED DOUBLE QUANTUM WELLS AND WIRES

1. INTRODUCTION

The microelectronics industry has continuously sought to increase the operating speeds and complexity of integrated circuits and to reduce their power dissipation. One of the most important methods for accomplishing these goals has been to reduce the minimum feature sizes of electronic devices. This trend has pushed feature sizes from $\approx$ 3 μm in 1980 [1] to roughly 0.35 μm in present day commercial devices and minimum feature sizes are predicted to reach 0.1 μm by the year 2007 [2]. Fundamental limits to continued miniaturization, first recognized by Swanson [3] and Landauer [4], will be reached in one or two decades [5, 6]. To continue the trend of miniaturization and enhanced performance, new technologies must be developed to replace traditional transistor technology before these limits are met.

Several devices that utilize quantum mechanical effects have been proposed as alternatives to today's technology. These quantum effect devices can be divided into three categories [7]:

1. Quantum wave devices: these devices are based on the quantum mechanical interference of electron wavefunctions and use the wave-nature of electrons. In one possible device, the electron wavefunction is split in two, the phase of one part is changed relative to the other, typically with a Schottky gate, and then the two components are brought back together and interfere either constructively or destructively, similar to a Mach-Zehnder interferometer [8].

2. Quantum functional devices: these use quantum mechanical effects such as tunneling or size-quantization effects. Cellular automata and single electron devices fall into this category.

Cellular automata are arrays of cells used to perform logic functions in which each cell interacts only with its nearest neighbors and, in some implementations, its next-nearest neighbors [9]. The state of each cell is determined from the states of its neighbors using predefined interaction rules. All data enters and exits from the edge of the array. One implementation of cellular automata is based on a cell composed of five coupled quantum dots; four at the corners of a square and the fifth in the center of the square [10]. Electrons can tunnel between the dots within a cell but can not tunnel from one cell to another cell. The ideal cell has two free electrons in it and therefore has two possible states which are determined by quantum mechanics and Coulomb interaction. The electrons can occupy either the upper left/lower right dots or lower left/upper right dots. Neighboring cells respond to a cell through Coulomb interactions which can cause a cell to change state. Several of these cells are grouped together to perform various logic functions, including inversion, and programmable AND and OR gates [11].

Single electron devices are composed of small metallic islands that are weakly coupled to source/drain regions through tunnel junctions and capacitively coupled to nearby electrodes. These devices show charging effects when single electrons tunnel onto or off of the metallic island. For a tutorial review of this subject, see reference [12]. One realization starts with a two-dimensional electron gas (2DEG) and uses Schottky gates to electrostatically form the metallic island, known as a quantum dot, that is linked to the 2DEG through tunnel junctions formed by two quantum point contacts. Quantum point contacts have been extensively studied and a review is given in reference [13]. Electrons can tunnel onto the dot through one junction and off of the dot through the other when a small source/drain bias is applied across the dot. A nearby electrode, known as a control gate, which is capacitively coupled to the device, is used to control the tunneling by

changing the electrostatic potential of the dot. A new approach for the design of digital logic circuits utilizing these devices has been suggested [14].

3. Atomic or molecular devices: these devices would apply an external signal to change the state of a molecule in a detectable way. The existence of molecules that mimic the behavior of a relay has been suggested but has yet to be demonstrated [15]. Research in this area is in its infancy and no specific devices have been proposed yet.

A system that holds promise for future quantum effect electronic devices, and also photonic devices, is coupled double quantum wells (DQWs) in III-V compound semiconductors. This system consists of two quantum wells separated by a narrow barrier which electrons can tunnel through. Several quantum effect devices have already been proposed for DQWs. These include the Double Electron Layer Tunneling Transistor (DELTT) [16], the velocity modulated transistor (VMT) [17] and the resonant interband tunneling transistor [18]. The purpose of the present study is to further investigate transport phenomena in DQWs to facilitate development of new electronic devices. The main emphasis of this work is the effect of dispersion curve distortions on the transport properties of DQWs. The dispersion curve is distorted by applying a magnetic field ($B_{||}$) in the plane of the QWs.

There has already been much work on the transport properties of DQWs, including tunneling between the two QWs, a resistance resonance that occurs when the QW densities are equal to each other, and the Coulomb drag effect which occurs when a current flowing through one QW induces a voltage drop in the other QW. Before reviewing this work in the second half of Chapter 2, the first half of that chapter provides an introduction to the DQW system. The conduction band diagram and wavefunctions are discussed along with a description of the basic characterization of a DQW sample. Chapter 3 discusses sample preparation and the experimental setup for all of the experiments.

The next three chapters discuss the experimental results of this dissertation. Chapter 4 investigates features in the in-plane conductance ($G_{||}(B_{||})$) which result from an anticrossing

of the QW dispersion curves due to $B_{||}$. The main effect of $B_{||}$ is a linear transverse shift of one QW dispersion curve with respect to that of the other QW. For the case of strong coupling between the two QWs, the two dispersion curves anticross and a partial energy gap opens, resulting in a two-component dispersion curve. These distortions in the dispersion curve give rise to distortions in the density of states, Fermi velocity and other transport properties. The features in $G_{||}(B_{||})$ evolve with surface gate and this dependence is used in a model to extract the layer separation and the energy gap. The second part of the chapter deals with the measurement of the electron cyclotron mass (m^*) in this system. The mass is obtained from the temperature dependence of the magnetoresistance (Shubnikov - de Haas (SdH)) oscillations when a small perpendicular ($B_{\perp}$) component of magnetic field is added to $B_{||}$. Both parts of this chapter also present theoretical calculations by S. K. Lyo that show excellent agreement with the experimental results.

Chapter 5 extends the experiments of Chapter 4 to the case of crossed magnetic fields. The addition of a stronger $B_{\perp}$ causes Landau level formation for each branch of the distorted dispersion curve. There is complex beating in the magnetoresistance as the electron population in one branch of the dispersion curve increases while the electron population of the other decreases as $B_{||}$ is increased. A semiclassical calculation of the Landau level positions in $B_{\perp}$ and $B_{||}$ is also performed. This calculation takes into account the changing m^* with $B_{||}$ and shows excellent agreement with the data. As $B_{\perp}$ is increased this field causes electrons to tunnel across the gap in **k**-space formed by the anticrossing. This tunneling is known as magnetic breakdown and results in additional beating in the magnetoresistance data at higher $B_{\perp}$.

Experiments on one-dimensional structures formed on DQWs are discussed in Chapter 6. The two main structures are quantum point contacts and short quantum wires. For both structures, an anticrossing in the one-dimensional dispersion curve, similar to the anticrossing of the two-dimensional dispersion curve in Chapter 4, is expected with the in-plane magnetic field perpendicular to the current. In the quantum point contacts, this

anticrossing would result in quantized conductance steps as a function of $B_{||}$ when each QW has a single conducting channel through it. For short quantum wires, Lyo has predicted that a quenching of intra-wire back scattering would result in an enhancement of the conductance by orders of magnitude. Finally, Chapter 7 summarizes this dissertation and suggests further experimental work that could be done with this system.

2. BACKGROUND

There has been much interest in DQWs in the last several years. This interest stems from the additional degree of freedom, which results from tunneling between the two QWs, found in this system as compared to single QWs. This chapter discusses the basic features of DQWs and reviews some of the new phenomena previously observed in these structures.

2.1 Electronic Properties of Double Quantum Wells

Coupled DQWs are formed by bringing two 2DEGs close to each other and separating them by a thin barrier which electrons can tunnel through. Because of their relevance to DQWs, the main properties of single 2DEGs will be presented in this section, along with their extension to DQWs. Single 2DEGs have been extensively studied over the last two decades and a large body of literature exists on the subject [19]. This work focuses on electron transport only. Therefore, optical properties, the valence band, holes, and excitons will not be considered here. A discussion of these topics can be found in references [20] and [21].

2.1.1 Growth Structure

A DQW consists of two regions of a narrow band gap semiconductor embedded in a wide band gap semiconductor and separated by a thin barrier of the wide band gap material. Electrons are confined to two-dimensional planes in the quantum wells formed by the narrow band gap material. Typically, the narrow gap semiconductor is gallium arsenide (GaAs) and the wide gap semiconductor is aluminum gallium arsenide ($Al_xGa_{1-x}As$), where x is the mole fraction of Al and is usually about 0.3. The mole fraction $x = 0.3$ is

used for several reasons. First, larger x results in larger barrier heights and better confinement of the electrons. However, above $x \approx 0.35$, the presence of defect levels, known as DX centers [22], becomes important and is manifested in effects such as persistent photoconductivity. For $x < 0.35$, these levels move above the Fermi energy and their presence does not affect electron transport Also, when x is increased above 0.45, the

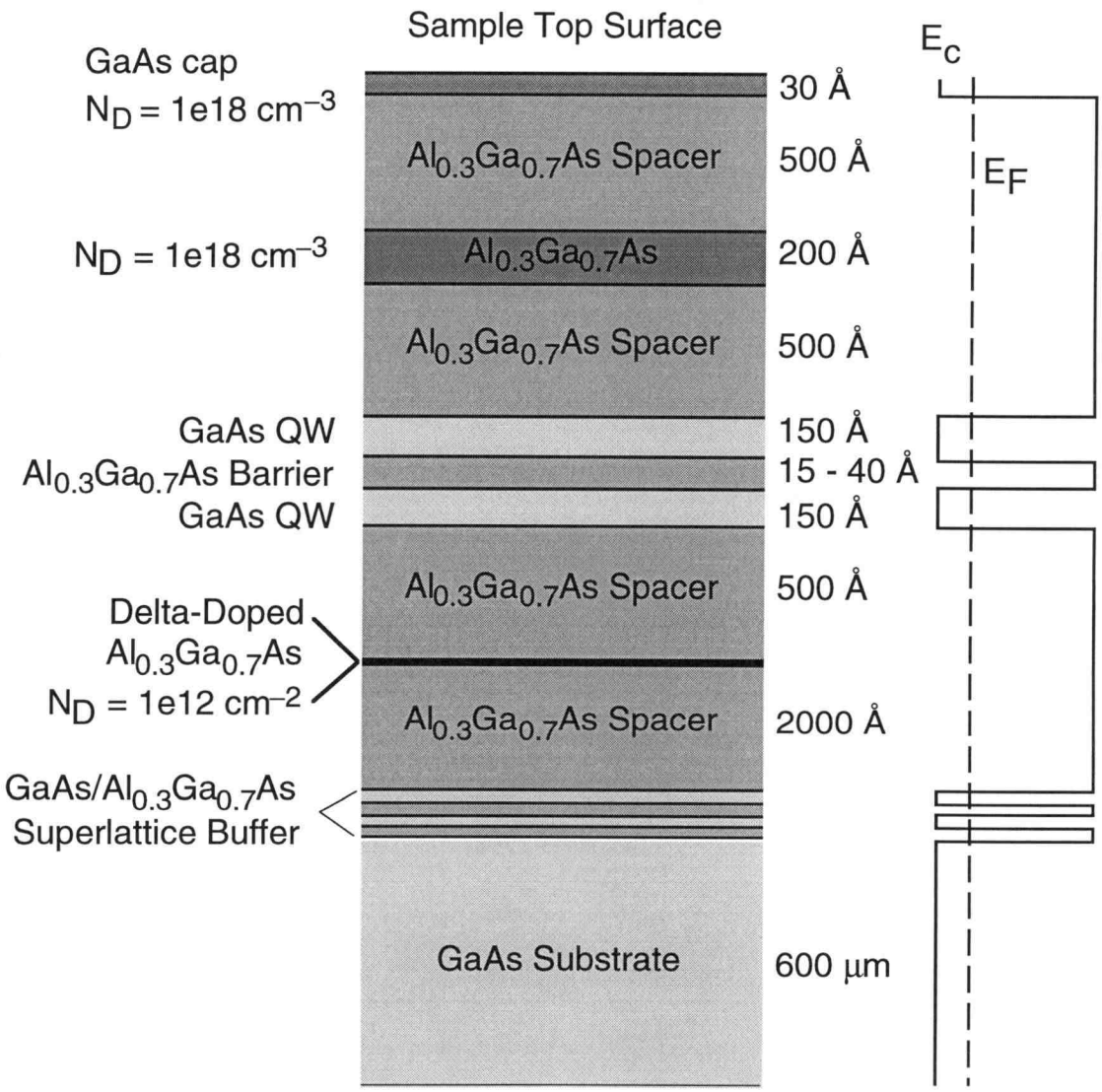

Fig. 2.1 Generic growth structure and conduction band schematic, with band bending ignored, for a double quantum well sample. Typical layer thicknesses and doping densities are also shown.

conduction band minimum goes from the Γ valley, which has a low effective mass, to the X valley which has a much higher effective mass [23]. These structures are most commonly grown by molecular beam epitaxy (MBE) but have also be grown using metalorganic chemical vapor deposition (MOCVD) [24, 25]. Both growth methods result in abrupt interfaces that are smooth on an atomic scale and high mobility material, with MBE material typically having considerably higher mobility than MOCVD material. Kelly [20] discusses both methods in detail and provides references to current research topics in semiconductor growth techniques. The mobility of DQW samples grown by either method is generally somewhat lower than single heterojunctions, due to the 'inverted' interface that occurs when switching from AlGaAs to GaAs during growth.

Fig. 2.1 shows a generic growth structure for a DQW sample with typical layer thicknesses shown. Modulation doping is employed to provide electrons for the QWs while keeping the mobility as high as possible by separating the dopants from the free electrons in the QWs, thereby reducing remote ionized impurity scattering. Narrower spacer layers result in higher electron densities but also in reduced mobility. In DQWs, the electron density is typically chosen such that only the two lowest subbands are occupied. The right side of Fig. 2.1 shows the sample's conduction band energy as a function of position, with band bending ignored. The conduction band offset (ΔE_c) between GaAs and $Al_xGa_{1-x}As$ is a strong function of mole fraction x. For $x < 0.45$, $\Delta E_c \approx (1.1\text{ eV}) \times x$ [23], where $\Delta E_c \approx 280 - 300$ meV for $Al_{0.3}Ga_{0.7}As$. At low temperatures, electron states are filled to the Fermi energy (E_F), which is shown as the dashed line.

2.1.2 Subband Energies and Wavefunctions

In the growth plane (x-y plane), the electrons are not confined and the wavefunctions for these directions can be taken as plane waves [20]. However, in the direction perpendicular to the growth plane (z-direction), the electrons are confined in the QWs and

the one-dimensional Schrödinger equation must be solved in the effective mass approximation to find the subband energies and wavefunctions. The one-dimensional Schrödinger equation is given by

$$\left(-\hbar^2/2m^*\left(\partial^2/\partial z^2\right) + V(z)\right)\Psi(z) = \varepsilon_n\Psi(z), \tag{2.1}$$

where $V(z)$ is the conduction band energy plus the electrostatic potential of the free electrons and ionized impurites, $\Psi(z)$ is the wavefunction, and ε_n is the eigenenergy. The electron effective mass is m^* (see Section 2.1.5), which for GaAs is $m^*_{GaAs} = 0.067m_e$ and for $Al_{0.3}Ga_{0.7}As$ is $0.073m_e$, where m_e is the free electron mass. For convenience, m^*_{GaAs} is typically used for both the QWs and the barriers. Due to band bending caused by ionized impurities and free electrons, the potential $V(z)$ must be found by solving Poisson's equation. In one-dimension, Poisson's equation is given by

$$d^2V(z)/dz^2 = -\rho(z)/\varepsilon_r, \tag{2.2}$$

where $\rho(z)$ is the charge density and ε_r is the relative dielectric constant. The free electron contribution to the charge density is obtained from the electron wavefunction obtained from the solution of the Schrödinger equation, where $\rho(z) = e|\Psi(z)|^2$. Therefore, these equations are solved iteratively, with the $V(z)$ found from Poisson's equation being used to solve the Schrödinger equation and the resulting electron wavefunction being used to modify the solution of Poisson's equation [26]. The iteration continues until in the change in the electron wavefunction, the subband energy levels, or the potential is small and meets a convergence criterion. This is known as a self-consistent solution. Electron-electron interactions can also be included using the Hartree approximation [27]. Closed-form, self-consistent solutions for DQW structures are not possible, so the solution must be obtained numerically. Finite difference and finite element techniques can be employed in the numerical solution of these equations [28].

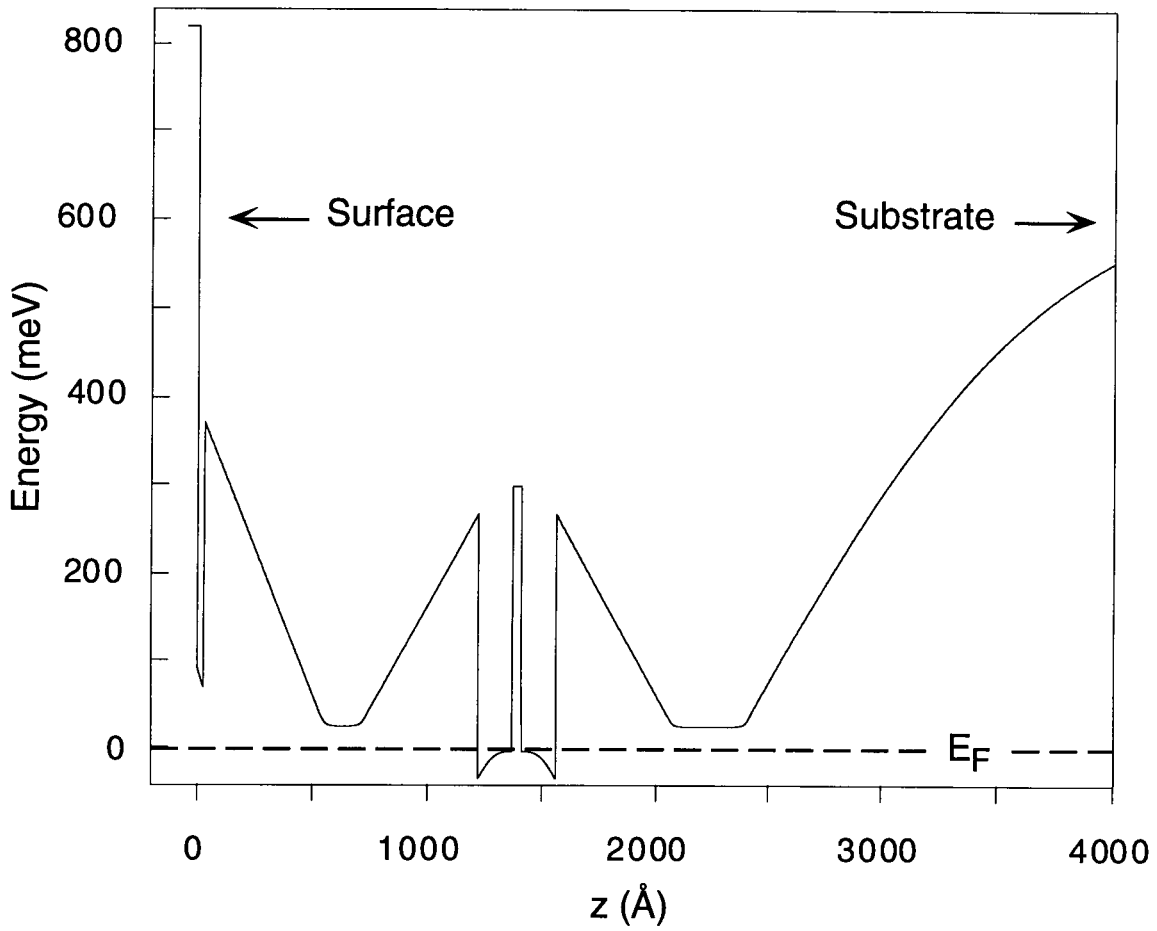

Fig. 2.2 Plot of the calculated conduction band energy as a function of position for a DQW.

Fig. 2.2 shows the results of a finite difference calculation which I performed for the structure shown in Fig. 2.1 with a barrier d = 25 Å. There are several features of the conduction band to note. First, and most important, is that the bottoms of the QWs, and only the QWs, are below the Fermi energy, ensuring that, at sufficiently low temperatures, there are free electrons in the QWs and no free electrons in other parts of the sample. As stated previously, electrons fill available states up to E_F while states above E_F remain unfilled at temperature T = 0. Also due to the electrons in the QWs, the bottoms of the QWs are not flat. This band bending pushes the electrons in one QW away from electrons

in the other QW, resulting in weaker coupling between the two QWs. At the surface of the sample, the Fermi energy is pinned near mid-gap by surface states [29]. This pinning can deplete the top QW if the top dopant layer is not doped heavily enough or if the total spacer thickness is too small. In the doped regions, the conduction band is pulled down close to the Fermi energy by the dopants. The energy required to promote an electron from a bound state in an impurity to the conduction band is the dopant ionization energy ε_D, where $\varepsilon_D \approx 8$ meV in $x = 0.3$ AlGaAs [23]. Thus the conduction band is pulled to within roughly 8 meV from the Fermi energy in the doped regions. Finally, in the bulk of the material, the Fermi energy approaches mid-gap as one goes deeper into the bulk because this region is undoped. This region may be unintentionally doped to $\approx 10^{14}$ cm^{-3} due to residual dopants in the system.

Expanded views of the bottoms of the QWs and the wavefunctions for two different gate biases (V_G) are shown in Fig. 2.3. Negative gate biases raise the conduction band at the surface of the sample and deplete electron layers under the gate, while positive biases lower the conduction band and increase the electron density. In the first case (Fig. 2.3(a)), $V_G \approx 0$ V and the two QWs have equal electron densities. In this case, the system is said to be 'in balance' or 'in resonance' and the band bending in one QW is nearly identical to the band bending in the other QW, except reflected about the center of the barrier. If there is no tunneling between the two QWs, the eigenenergies for the lowest two states are equal and the wavefunctions are localized in one QW or the other. However, when tunneling is permitted, the wavefunctions are delocalized across both QWs and the two energy levels repel each other, forming symmetric and antisymmetric states. These states have unequal electron densities but the two QWs still have equal electron densities. The energy difference between these subbands is $\Delta E = \varepsilon_2 - \varepsilon_1 = \Delta_{SAS}$, the symmetric-antisymmetric gap. For the structure simulated, $\Delta_{SAS} \approx 1.32$ meV and is too small to be resolved in Fig. 2.3(a). Tunneling is strong when the sample is in balance because energy and momentum are conserved in a tunneling event, as will be discussed below.

As V_G is made more negative, the density of the top QW decreases while the density of the bottom QW remains unchanged [30] and the sample is now said to be 'out of balance' or 'out of resonance'. Fig. 2.3(b) shows the same sample for the case where V_G « 0 V, where the sample is out of balance. Energy and momentum conservation are no

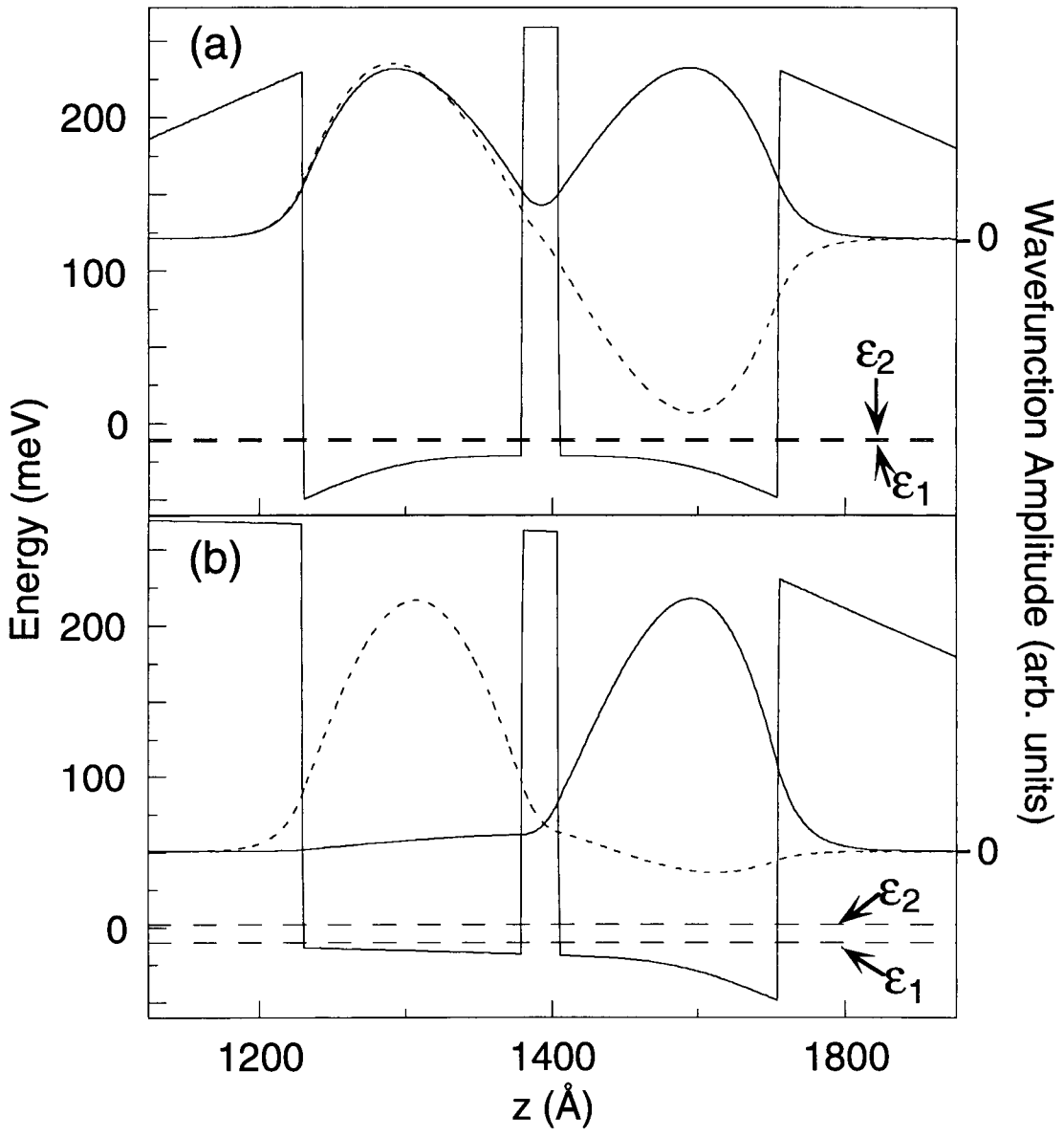

Fig. 2.3 Plot of the conduction band energies and wavefunctions (solid = φ_1, dotted = φ_2) for (a) balanced DQW and (b) unbalanced DQW. The dashed lines indicate the eigenenergies of the two states.

longer met and tunneling between the two QWs is now reduced. The ground-state wavefunction is mostly confined to the bottom QW with eigenenergy $\varepsilon_1 = -10.2$ meV and the next higher subband is mainly confined to the top QW with eigenenergy $\varepsilon_2 = 1.8$ meV. This subband is totally depleted of electrons because its eigenenergy is above the Fermi energy ($E_F = 0$). The energy difference is now given by $\Delta E = \varepsilon_2 - \varepsilon_1 = [\Delta E_{QW}^2 + \Delta_{SAS}^2]^{-1/2}$ [31], where $\Delta E_{QW} = \varepsilon_2^i - \varepsilon_1^i$ and $\varepsilon_{2,1}^i$ are the eigenenergies of the isolated single QWs, which are obtained by solving the Schrödinger equation. When Δ_{SAS} is small compared to ΔE_{QW}, the two wavefunctions become totally localized in one QW or the other. In the balanced, unbalanced, and intermediate regimes, the system forms two parallel 2DEGs.

An approximate solution to the Schrödinger equation can be obtained using a tight-binding perturbation calculation where the single isolated square QW wavefunctions ($|\psi_1\rangle$, $|\psi_2\rangle$) are used as basis wavefunctions [20, 21]. The isolated QWs are assumed to be identical, each with eigenenergy ε_{QW}. The wavefunctions are obtained from analytic solutions of the Schrödinger equation for finite wells, which can be found in introductory quantum mechanics books [21, 32]. The infinite well approximation cannot be used in this situation because the wavefunctions are zero outside of the QWs, resulting in no coupling between the QWs when they are brought close to each other. The coupled-QW wavefunction ($|\Psi\rangle$) is assumed to be a linear combination of the isolated-QW wavefunctions; $|\Psi\rangle = \alpha|\psi_1\rangle + \beta|\psi_2\rangle$. The Schrödinger equation is expanded in terms of this basis and is written in matrix form as:

$$\begin{pmatrix} \varepsilon_0 + V_1 - E & V_{12} \\ V_{12} & \varepsilon_0 + V_1 - E \end{pmatrix} \begin{pmatrix} \alpha \\ \beta \end{pmatrix} = \begin{pmatrix} 0 \\ 0 \end{pmatrix}, \tag{2.3}$$

where the matrix elements are: $V_1 = \langle\psi_1|V_2(z)|\psi_1\rangle = \langle\psi_2|V_1(z)|\psi_2\rangle$ and $V_{12} = \langle\psi_1|V_2(z)|\psi_2\rangle = \langle\psi_2|V_1(z)|\psi_1\rangle$.

This equation is solved to give the energy levels $\varepsilon_{1,2} = \varepsilon_o + V_1 \pm |V_{12}|$ resulting in $\Delta_{SAS} = 2|V_{12}|$. The lower energy state is the symmetric combination of basis wavefunctions and the higher energy state is the antisymmetric combination. This method over-estimates Δ_{SAS} because it ignores band bending which moves the wavefunctions to the outsides of the QWs (*i.e.* farther apart), reducing their overlap and thus Δ_{SAS}.

2.1.3 Symmetric-Antisymmetric Energy Gap

Δ_{SAS} is a measure of the coupling strength between the two QWs and depends strongly on the width and height of the barrier between them and to a lesser extent on the QW width and electron densities. For wider, higher barriers, the wavefunction of one QW does not extend as far into the other QW, which results in a smaller Δ_{SAS}. The height of the barrier is lowered by reducing x, the Al concentration of the $Al_xGa_{1-x}As$ barrier. The wavefunctions of wider QWs do not extend as far into the barriers as those of narrower QWs and this also results in a smaller Δ_{SAS}. Increasing the electron densities in the QWs results in increased band bending which pushes the wavefunctions farther apart and reduces Δ_{SAS}. For closely coupled DQWs, Δ_{SAS} is on the order of 1 meV and decreases with increasing barrier thickness.

Table 2.1 lists the four general regimes of coupling: (1) No coupling: in this regime the

Table 2.1: Coupling regimes in double quantum wells.

COUPLING REGIME	Δ_{SAS} (meV)	BARRIER (Å)
No Coupling	0	$b > 1000$
Coulomb Coupling	≈ 0	$200 < b < 1000$
Weak Tunneling	< 1	$50 < b < 200$
Strong Tunneling	> 1	$b < 50$

electron wavefunctions in the individual QWs do not overlap and the Coulomb interaction between electrons in opposite QWs is negligible. (2) Coulomb coupling: the Coulomb coupling regime is characterized by Coulomb interactions between electrons in opposite QWs but tunneling does not occur between the two QWs. (3) weak tunnel coupling. (4) strong tunnel coupling. In the two tunneling regimes, electron wavefunctions from the two QWs overlap and tunneling is allowed between the two QWs. The boundaries between these different regimes are not abrupt. For weakly coupled DQWs, Δ_{SAS} approaches zero and for strongly coupled systems it can be as high as 15 – 20 meV. For the samples in this work Δ_{SAS} = 1 – 3 meV, which represents fairly strong coupling. There are several methods used to determine Δ_{SAS} and these will be discussed later.

2.1.4 Dispersion Curve and Fermi Surface

In Section 2.1.2, the subband energy (ε_n) associated with confinement in the z-direction was calculated. The kinetic energy associated with motion in the x-y plane is $\hbar^2/2m(k_x^2 + k_y^2)$, giving a total energy of $E = \varepsilon_n + \hbar^2/2m(k_x^2 + k_y^2)$ where k_x and k_y are the wave vectors in the x- and y-directions, respectively. The resulting energy versus wave vector diagram for a given n (fixed ε_n), also known as a dispersion curve, is a paraboloid with states existing only on the surface of the paraboloid. In three-dimensions, the dispersion curve is also a paraboloid, but in that case, states exist on the surface and within the volume of the paraboloid. Fig. 2.4(a) shows the dispersion curve for a DQW with two subbands occupied. The dispersion curve has the same form when the system is in either the balanced or unbalanced state. The Fermi surface (FS) is the intersection of the dispersion curve with a plane at the Fermi energy (E_F) and, for DQWs, the two-dimensional Fermi surface consists of two concentric circles. Electrons fill available states up to E_F while states above E_F remain unfilled at temperature $T = 0$. The Fermi surface is

important because transport occurs within a few k_BT of E_F so only electrons on the Fermi surface need to be considered when studying conduction at low temperatures [33].

2.1.5 Density of States, Effective Mass, and Fermi Velocity

Several important quantities are calculated from the dispersion curve. The first is the density of states (DOS), which is important because many transport, optical, and thermodynamic quantities are closely related to the DOS and, in particular, to the functional form of the DOS near band edges [20]. The DOS is defined as the number of states per

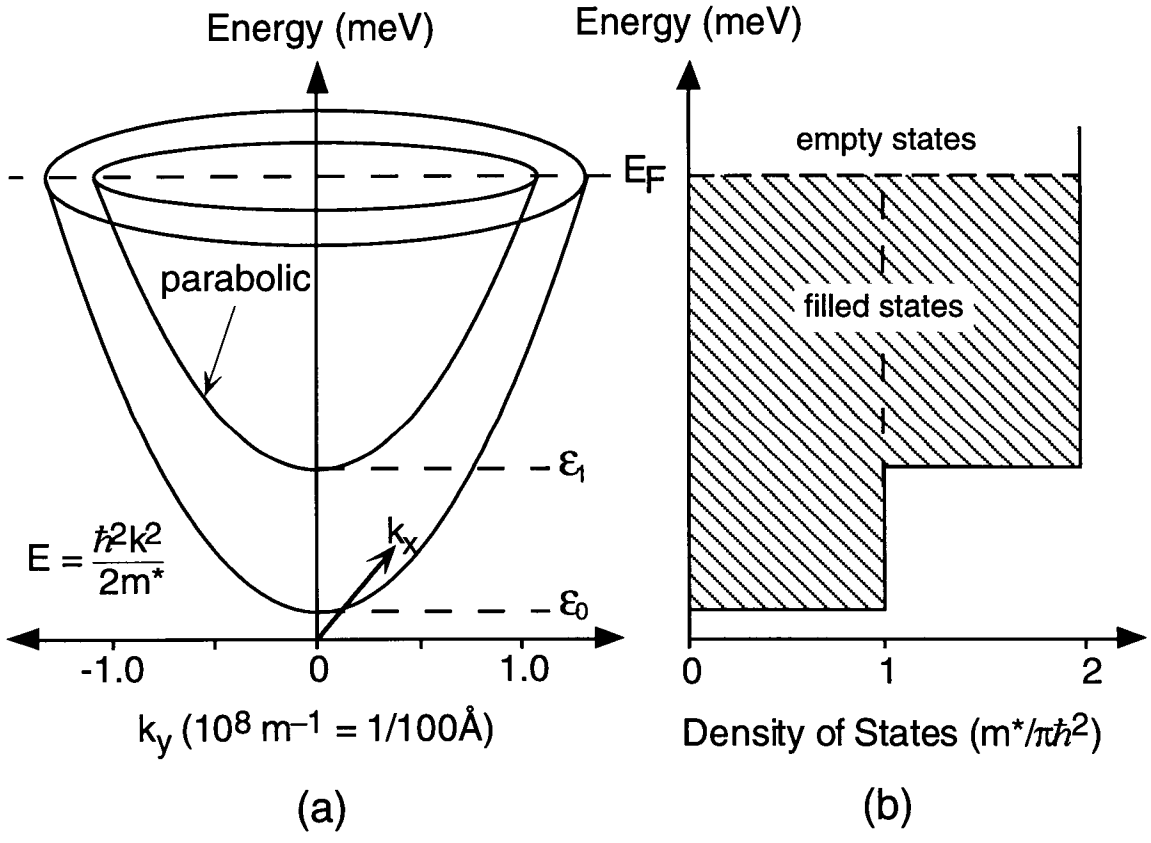

Fig. 2.4 (a) Dispersion curve for a DQW with two subbands occupied. (b) The density of states for the dispersion curve shown.

unit area per unit energy and is equal to $1/A_c(dN_T(E)/dE)$, where A_c is the area of the conductor and $N_T(E)$ is the number of states with energy less than E [33]. For 2DEGs, $N_T(E) = g_s \times$ (FS area) / (area/state) $= 2 \times (\pi k^2)/(4\pi^2/A_c) = m^*A_c/(\pi\hbar^2) \times (E-\varepsilon_n)$, where g_s is the spin degeneracy ($g_s = 2$ when there is no spin splitting), ε_n is the subband energy, and the areas are **k**-space areas. From this, DOS $= m^*/(\pi\hbar^2)\ \vartheta(E-\varepsilon_n)$, where ϑ is the unit step function. The DOS is constant for each subband and the total DOS has a step increase when another subband is occupied. Fig. 2.4(b) shows the DOS for a DQW with two subbands occupied.

The second quantity obtained from the dispersion curve is the electron effective mass m^*. The effective mass accounts for the effects of the periodic potential of the semiconductor crystal on the electrons and is given by: $1/m^* = 1/\hbar^2(d^2E(\mathbf{k})/d\mathbf{k}^2)$. Thus, m^* is inversely proportional to the curvature of the dispersion curve and for a parabolic dispersion it is constant. A third important quantity that is calculated from the dispersion curve is the group velocity, which is $v = 1/\hbar(dE(\mathbf{k})/d\mathbf{k})$ [21]. Thus the velocity is determined by the slope of the dispersion curve and for parabolic dispersion it is linear with **k** ($v = \hbar k/m^*$).

2.1.6 Conduction and Mobility ($B = 0$)

The response of electrons in a 2DEG to an applied electric field is the same as that of electrons in metals. With no applied field, the electrons move in random directions with no net current flow. When the external field **E** is turned on, the electrons acquire an average drift velocity v_d in the direction of the field. At steady-state, the rate at which momentum is gained from the field is equal to the rate at which momentum is lost in scattering processes [33]; $(d\mathbf{p}/dt)_{field} = (d\mathbf{p}/dt)_{scattering}$. $(d\mathbf{p}/dt)_{field} = -e\mathbf{E}$ and $(d\mathbf{p}/dt)_{scattering} = m^*v_d/\tau_m$, where τ_m is the momentum relaxation time. The mobility μ of a sample is a measure of how easily electrons respond to applied fields and is defined as $\mu = |v_d / \mathbf{E}|$ and from the

above equations, $\mu = e\tau_m/m^*$. Due to reduced ionized impurity scattering, 2DEGs have low scattering rates and thus have high mobilities.

Another related quantity is the sample conductivity σ, which is defined as $\mathbf{j} = \sigma\mathbf{E}$, where $\mathbf{j}$ is the current density, $\mathbf{j} = -ev_d n_s$, where n_s is the electron density. Using the equations from above, $\sigma = n_s e^2\tau_m/m^* = e\mu n_s$. From this, the product μn_s can be obtained from measurements of the conductivity at zero magnetic field. However, conductivity measurements in perpendicular magnetic fields can give both n_s and μ, as will be discussed

In DQWs, these quantities have the same definitions, but there is the added complications of having two electron channels. Measurements with $B = 0$ can give the conductivity, and thus product of mobility and density, of both subbands in parallel ($\sigma_{total} = e\mu_{total}n_{total}$) or, by depleting the top QW with a gate bias, the conductivity of the bottom QW (σ_{bottom}) can be measured, assuming σ_{bottom} is when carriers exist in the top QW as it is when there are no carriers in the top QW. The top QW conductivity (σ_{top}) can then be calculated from $\sigma_{total} = \sigma_{top} + \sigma_{bottom}$. When the DQW is in balance, the electron wavefunctions occupy both QWs equally and the total conductivity is approximately equal to the lower of the two QW conductivities.

2.1.7 Hall Effect and Quantum Hall Effect in Single 2DEGs

Conductivity measurements in weak magnetic fields (Hall effect) and in strong magnetic fields (quantum Hall effect) are important techniques for separately determining the mobility and density of 2DEGs. In both cases, the magnetic field is applied perpendicular to the plane of the 2DEG. Both techniques can be used to characterize DQWs, although the Hall effect gives only the mobility and density for both QWs in parallel, while the quantum Hall effect, on the other hand, can be used to obtain the densities and mobilities for the individual QWs.

In magnetic fields ($\mathbf{B}$ = (0, 0, $B_\perp$)), the momentum relationship, $(d\mathbf{p}/dt)_{field}$ = $(d\mathbf{p}/dt)_{scattering}$, now becomes $-e(\mathbf{E} + v_d \times \mathbf{B}) = m^* v_d/\tau_m$. This can be rewritten as[33]:

$$\begin{bmatrix} m^*/e\tau_m & -B_\perp \\ B_\perp & m^*/e\tau_m \end{bmatrix} \begin{pmatrix} v_x \\ v_y \end{pmatrix} = \begin{pmatrix} E_x \\ E_y \end{pmatrix}, \tag{2.4}$$

where v_x, v_y and E_x, E_y are the x- and y-components of the velocity and electric field, respectively. Using $\mathbf{j} = -ev_d n_s$, $\sigma = e\mu n_s$, and $\mu = e\tau_m/m^*$, and rearranging

$$\begin{pmatrix} E_x \\ E_y \end{pmatrix} = \begin{bmatrix} \rho_{xx} & \rho_{xy} \\ \rho_{yx} & \rho_{yy} \end{bmatrix} \begin{pmatrix} J_x \\ J_y \end{pmatrix}, \tag{2.5}$$

where the resistivities are $\rho_{xx} = \rho_{yy} = \sigma^{-1}$ and $\rho_{xy} = -\rho_{yx} = B_\perp/en_s$. In two dimensions, the longitudinal resistance (R_{xx}) is $R_{xx} = \rho_{xx}$ (W/L), where W/L are the width and length of the sample, respectively, and the Hall resistance (R_{xy}) is equal to ρ_{xy}. This model predicts that R_{xx} will be constant with $B_\perp$ and R_{xy} will increase linearly with $B_\perp$. Experiments on single 2DEGs (Fig. 2.5) show that this is true for low magnetic fields ($B_\perp < \approx 0.5$ T). However, at higher $B_\perp$, R_{xy} has plateaus and R_{xx} oscillates. The model presented above can not explain this behavior; so a new model will have to be devised. This measurement can be used to obtain n_s from the slope of ρ_{xy} versus $B_\perp$ when this trace is linear at low $B_\perp$. However, if conduction also occurs through the doped regions (parallel conduction), the slope of ρ_{xy} changes and the correct value of n_s in the QW is not obtained.

To properly describe these results, the Schrödinger equation including a vector potential to represent the magnetic field must be solved. This calculation is done elsewhere [34]; here, however, a more physical explanation will be given. Classically, the magnetic field will cause electrons to move in circular orbits in the plane of the 2DEG with radius r_c = v/ω_c, where $\omega_c = eB_\perp/m^*$. Classically, r_c can have any value, but quantum mechanically, the circumference of the orbit must be an integer number of de Broglie wavelengths (h/m^*v). Thus $2\pi r_c = ih/m^*v$ where i is an integer. This restriction quantizes the kinetic energy ($m^*v^2/2 = i\hbar\omega_c/2$) and predicts that the total energy is E =

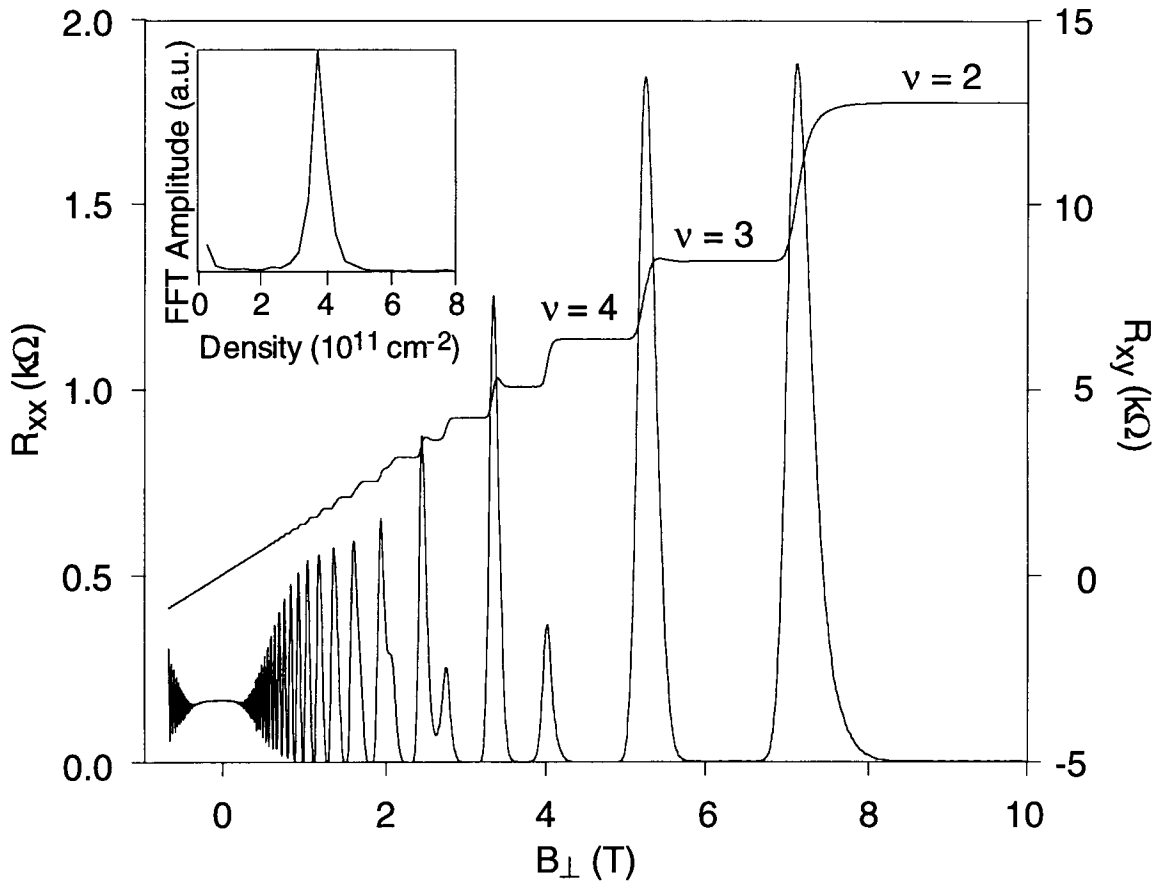

Fig. 2.5 Measured R_{xx} and R_{xy} for a single 2DEG. The Landau level filling factors are indicated for ν = 2, 3, and 4. The inset shows a fast Fourier transform of R_{xx} versus $1/B_\perp$.

$\varepsilon_n + i(\hbar\omega_c/2)$. This result is similar to the energy predicted by the full quantum mechanical calculation, where $E = \varepsilon_n + (i + 1/2)\hbar\omega_c$. These energy levels are known as Landau levels (LLs).

Fig. 2.6(a) shows the DOS of the system which now has peaks at the Landau levels. These peaks are delta functions when there is no broadening or disorder, and take on a finite width when scattering is present. The DOS at a Landau level with broadening is sketched in Fig. 2.6(b). As is shown, the tails of the peak contain localized states, due to the presence of disorder, while the center of the peak consists of extended states,

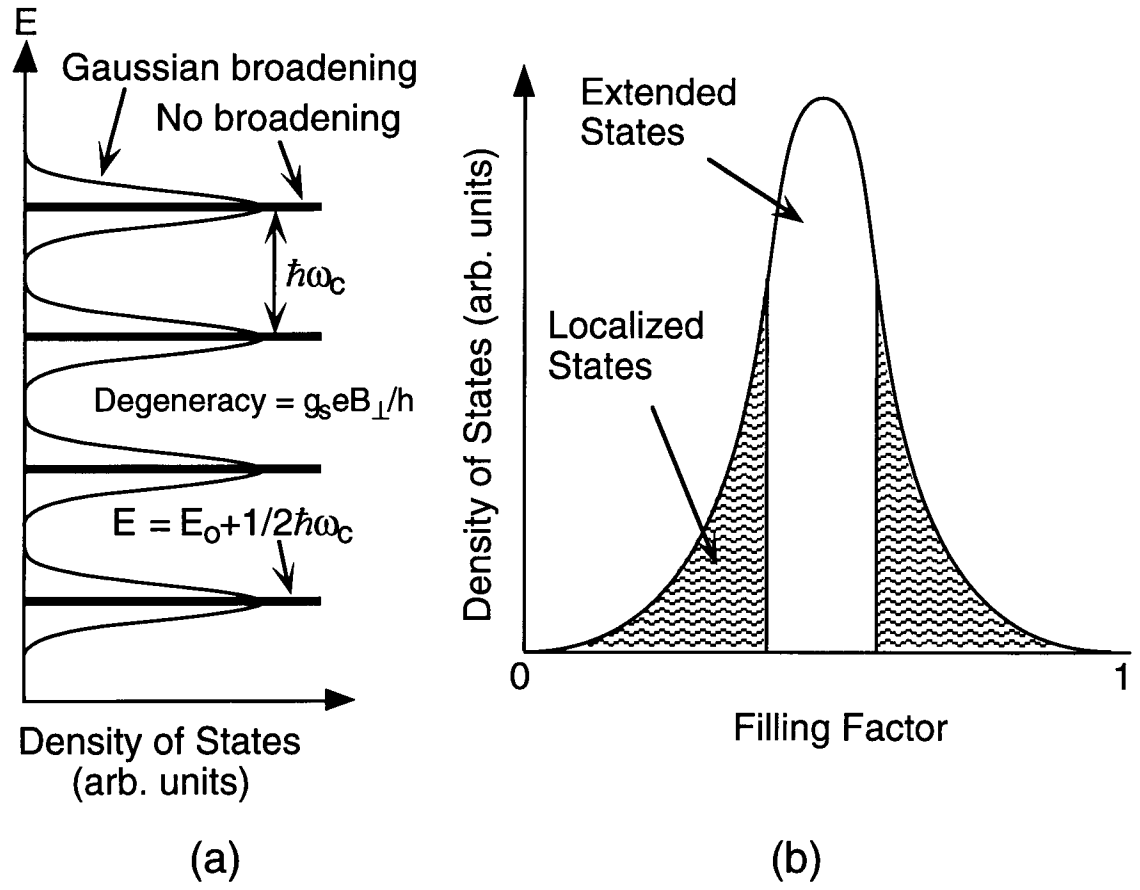

Fig. 2.6 (a) Density of states of a single 2DEG in $B_\perp$. (b) Expanded view of the DOS for a single Landau level showing the localized and extended states.

broadened due to scattering. The energy spacing between Landau levels is $\hbar\omega_c$, which is proportional to $B_\perp$, and the degeneracy of each level is $g_s eB_\perp/h$, where g_s is the spin degeneracy. (At low $B_\perp$, the levels are not spin split and $g_s = 2$ while at high $B_\perp$, they are spin split and $g_s = 1$.) Therefore, as $B_\perp$ increases, the spacing between the Landau levels and the number of electrons in each level increases.

The oscillations in R_{xx} and the plateaus in R_{xy} can be explained in terms of these Landau levels. When E_F is in a Landau level, current-carrying electrons can scatter from one extended state to another, resulting in a high resistance. However, when $B_\perp$ is

increased so that E_F is between two Landau levels, there are no available extended states for current-carrying electrons to scatter into and the resistance decreases. The Fermi energy can reside between two Landau levels because there are localized, non-current carrying states which pin E_F here (see Fig. 2.6(b)). If these states did not exist, E_F would jump from one Landau level to the next higher Landau level as $B_\perp$, and hence the Landau level degeneracy, was decreased. Rather, as $B_\perp$ is increased Landau levels move up in energy and pass through E_F. Hence, R_{xx} goes through one cycle of oscillation when the system changes from the center of one Landau level being at E_F to the center of the next Landau level being at E_F. At lower $B_\perp$, the Landau levels are still fairly close together and their tails overlap, so the resistance does not go to zero. But at higher $B_\perp$, the spacing between Landau levels is sufficiently large that the resistance drops to zero.

The Hall resistance has plateaus when E_F is between Landau levels because the number of current-carrying states is constant while the localized states are swept through E_F. The Hall resistance is quantized at values of $R_{xy} = B_i/en_s = (h/g_se^2)/i$, where B_i is the field in the middle of a plateau, i is an integer, and $n_s = i(g_seB_i/h)$ (see below) was used. R_{xy} depends on fundamental constants only and not on any material parameters. This effect is known as the quantum Hall effect and was first observed by von Klitzing *et al.* in 1980 [35]. In ultra-pure samples, plateaus in R_{xy} and minima in R_{xx} can appear when a certain fraction of a Landau level is filled. This is the fractional quantum Hall effect and was first seen by Tsui *et al.* in 1982 [36]. Several review articles give more details on these two phenomena [34, 37, 38].

The Landau level index i can be determined by inspection from the plateaus in R_{xy} and the minima in R_{xx}. At high $B_\perp$, where ρ_{xy} = 25.8 kΩ, ρ_{xx} is at a minimum, and at magnetic field $B_\perp = B_1$, only one Landau level (index i = 1) is occupied (the lowest index seen in Fig. 2.5 is i = 2). The next minimum in R_{xx} occurs when two Landau levels are occupied at $B_\perp = B_1/2$ and R_{xy} = 25.8 kΩ / 2 = 12.9 kΩ. As $B_\perp$ is decreased, successive minima in R_{xx} and plateaus in R_{xy} occur at B_1/i. The electron density can then be calculated

by multiplying the number of occupied Landau levels by the Landau level degeneracy; $n_s = i\,(g_s e B_i/h)$, where B_i is the magnetic field at the minima in R_{xx}. The Landau level filling factor (ν) is the ratio of the total density to the Landau level degeneracy, where $\nu = n_s/g_s e B_\perp/h$. The filling factor is an integer when the highest Landau level is completely filled and it is a real number when the highest level is partially filled. The filling factors for several completely filled Landau levels are labeled in Fig. 2.5.

The density can be calculated from the oscillations in R_{xx} in another way. The number of occupied Landau levels is given by $n_s/(\,g_s e B_i/h)$ and if B_1 and B_2 are the magnetic field values of two successive peaks,

$$\frac{n_s}{g_s e B_1/h} - \frac{n_s}{g_s e B_2/h} = 1, \text{ then}$$

$$n_s = \frac{g_s e}{h}\,\frac{1}{(1/B_1) - (1/B_2)} = \frac{g_s e}{h}\,\frac{1}{\Delta(1/B)}\,. \tag{2.6}$$

This holds for any two successive peaks and shows that the oscillations are periodic in $1/B_\perp$ and the density can be calculated from that period. The period can be calculated by inspection by reading values off of the graph or it can be obtained from the Fourier power spectrum of R_{xx} versus $1/B_\perp$. The inset to Fig. 2.5 shows the results of a fast Fourier Transform (FFT) performed on the data of Fig. 2.5. The densities calculated by this method and from the positions of the minima agree to within roughly 10%.

2.1.8 Quantum Hall Effect in Double Quantum Wells

The above description for single 2DEGs in a perpendicular magnetic field also holds for DQWs with a slight modification. The description above was for a system with only one subband occupied. When a second subband is occupied, there are oscillations in R_{xx} due to the first subband and oscillations from the second subband superimposed on the first set of oscillations. Due to the density difference between these two subbands, the two sets

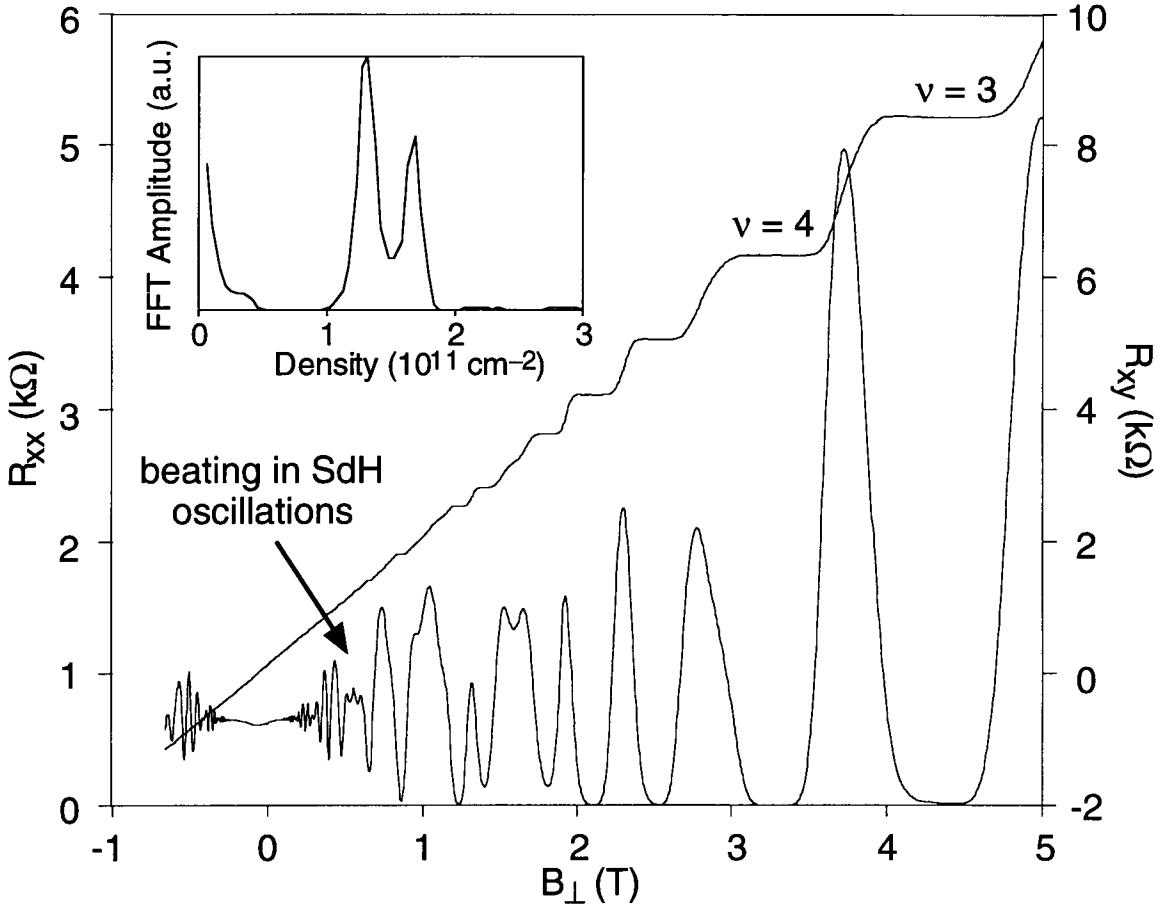

Fig. 2.7 Measured R_{xx} and R_{xy} for a DQW. The oscillations in R_{xx} show beating due to the two component Fermi surface. The Landau level filling factors are indicated for $\nu = 3$ and 4. The inset shows a fast Fourier transform of R_{xx} versus $1/B_\perp$. The FFT has a peak for each occupied subband.

of oscillations have different frequencies which results in beating in the oscillations as shown in Fig 2.7 for a DQW. Similar beating is seen in single QWs with two subbands occupied. The Hall resistance again has plateaus where R_{xx} has minima. The total density can be obtained from the positions of minima in R_{xx} and plateaus in R_{xy}, as done for single 2DEGs. To obtain the densities for both subbands, the Fourier power spectrum of R_{xx} versus $1/B_\perp$ must be calculated. The results of an FFT on the data of Fig. 2.7 are shown as an inset to that figure. There are two sharp peaks in the FFT, corresponding to the

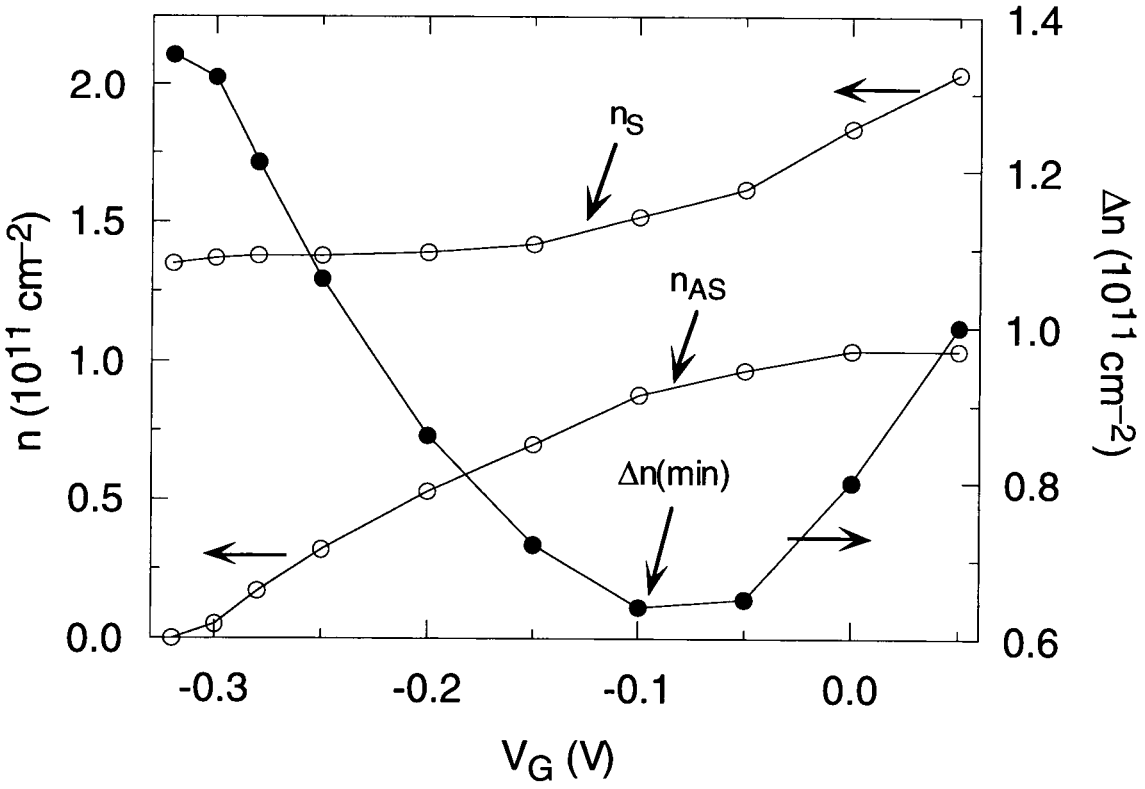

Fig. 2.8 Measured density (open circles) and density difference (closed circles) for the two lowest subbands of sample E.

densities of the two subbands and the sum of these agree to within roughly 10% with the total density calculated from the Landau level positions.

The densities obtained from the SdH oscillations can be used to determine Δ_{SAS} [39]. The symmetric-antisymmetric energy gap is given by $\Delta_{SAS} = E_S - E_{AS}$, where $E_{S,AS} = \hbar^2 k_{S,AS}^2/2m^*$ and $k_{S,AS} = (2\pi n_{S,AS})^{1/2}$ are the radii of the two Fermi circles. From these, $\Delta_{SAS} = \pi\hbar^2\Delta n/m^*$, where $\Delta n = n_S - n_{AS}$ is the minimum density difference between the two subbands. The densities of the two subbands are found as a function of gate bias and the minimum density difference is used to calculate Δ_{SAS}. The density and density difference as a function of gate bias for sample E (see section 3.1) are shown in Fig. 2.8. The minimum $\Delta n \approx 0.64 \times 10^{11}$ cm^{-2} at $V_G \approx -0.1$ V gives $\Delta_{SAS} = 2.3$ meV, in good

agreement with the calculated value of 2.1 meV. Near $V_G \approx -0.1$ V, the system is balanced and therefore, the two QWs have equal electron densities and the wavefunctions are equally shared by the QWs. Near $V_G \approx -0.3$ V and $V_G \approx 0.5$ V, the QWs have unequal densities and the wavefunctions are becoming localized in the QWs. Another method for calculating Δ_{SAS} from transport measurements is presented in Chapter 4. Raman spectroscopy, which is a resonant inelastic light scattering technique, can also be used to determine Δ_{SAS} optically [40, 41].

2.2 Literature Review

Improvements in MBE growth in the last five years have allowed the growth of DQWs with mobilities approaching those found in single 2DEGs. This improvement in sample quality has made a variety of transport experiments in DQWs possible. Here, several of the key experimental results will be summarized.

In transport experiments in high perpendicular magnetic fields, both the integer and fractional quantum Hall effects have been observed in DQWs [39] and other multi-layer structures [42, 43]. What sets DQWs apart from single 2DEGs is that odd-integer quantum Hall states can be missing under certain conditions [39] and the $\nu = 1/2$ fractional state [44], which is not seen in single 2DEGs can appear. The missing odd-integer quantum Hall states have been investigated both experimentally [39, 45, 46] and theoretically [47, 48]. The odd-integers in DQWs are caused by the Δ_{SAS} energy gap, which is the single-particle tunneling gap. When the interlayer Coulomb interactions dominate, the Δ_{SAS} gap collapses and the ground-state is a gapless correlated bilayer state. That is, the electrons correlate their interlayer positions so as to reduce their Coulomb energy. This leads to the disappearance of the $\nu = 1$, and 3 states. The appearance of the fractional state at $\nu = 1/2$ is also thought to be caused by interplay between intralayer and interlayer Coulomb correlations [44]. The possibility of correlated states in Coulomb-coupled DQWs has also

been extensively studied theoretically [49 – 52]. These phenomena have also been observed in wide single 2DEGs with two subbands occupied [53, 54].

In a precursor to the work presented here, Boebinger *et al.* measured the magneto-resistance of a DQW in small tilted magnetic fields [55], with $0 < B_{\perp} < 0.8$ T and $0 < B_{||} <$ 1.4 T, where $B_{||}$ is the in-plane magnetic field component. For constant, non-zero $B_{||}$ and changing $B_{\perp}$, the magnetoresistance shows SdH oscillations with beating, similar to the $B_{||}$ = 0 T case. Nodes in the beating occur when phases of the oscillations from the two subbands differ by an odd multiple of π. The $B_{\perp}$-positions of these nodes change with $B_{||}$, indicating that the density difference between the two subbands increases with $B_{||}$. A calculation of the dispersion curve showed that $B_{||}$ distorts the dispersion. These distortions are the emphasis of the present work and will be discussed in greater detail in Chapter 4. The $B_{\perp}$-positions of the nodes can also be calculated semiclassically and. for low $B_{\perp}$, good agreement between measured and calculated node positions was obtained, while deviations from semiclassical behavior are observed at higher $B_{\perp}$. These deviations were later attributed to magnetic breakdown [56] Magnetic breakdown is tunneling across gaps in **k**-space from one Fermi surface component to another, and is caused by $B_{\perp}$. Magnetic breakdown will be discussed in Chapter 5. We note that, surprisingly, Boebinger *et al.* failed to realize that, at sufficiently high $B_{\perp}$, the Fermi surface distortions take on a completely different character, resulting in an anticrossing and singularities in the density of states, effective mass, and group velocity. The work described in this thesis was the first observation of that effect.

One of the main areas of research in DQWs has been tunneling from one QW to the other, which is tunneling from 2D to 2D. Resonant 3D-2D tunneling has been widely studied in double barrier structures [57]. The first 2D-2D tunneling experiments were done on GaAs/AlGaAs heterostructures with an inversion layer and an accumulation layer separated by a doped AlGaAs barrier [58]. Due to conservation of in-plane momentum, resonant tunneling only occurs when the QW subbands are aligned. This means that the

parabolic dispersion curves of the two QWs must sit on top of one another. The tunneling conductance can be directly measured by making electrical connection to the individual QWs [59], typically using front and back depletion gates. A variety of methods have been used to make back gates on DQWs [60 – 62]. By using a surface gate, the density, and therefore subband energy, of the top QW can be varied and the DQW brought in to resonance. Sharp peaks in the conductance are observed when the system is in resonance and electrons tunnel from one QW to the other [59]. 2D-2D tunneling has also been studied in parallel [63 – 65] and perpendicular [66, 67] magnetic fields. Resonant tunneling between a 2DEG and a quasi -1D wire has been investigated on DQWs [68]

Another resonant phenomenon found in DQWs is the resistance resonance [69]. The resistance of both QWs in parallel is measured as a function of gate bias and, when the two QWs are in resonance, a local maximum in the resistance occurs. When the system is out of resonance, the lowest subband's wavefunction is localized in the higher density QW and the next higher subband's wavefunction is localized in the other QW. The resistance of the system is the parallel combination of the resistance of the two QWs and approaches the resistance of the lower resistance QW. When the system is in resonance, the wavefunctions of the two lowest subbands extend across both QWs equally and the resistance approaches that of the higher resistance QW [69]. The resistance peak is enhanced when the two QWs have drastically different mobilities[70, 71]. The resistance resonance is suppressed in an in-plane magnetic field [72] and the characteristic field necessary for the suppression of the resonance can be used to study electron-electron scattering rates in this system [73].

Electron-electrons interactions in DQWs can also be measured through Coulomb drag studies [74]. In Coulomb coupled DQWs with electrically isolated QWs, a frictional drag voltage is induced in one QW when a current is passed through the other. The voltage results from momentum transfer due to Coulomb scattering between electrons in the different QWs. This phenomenon was first observed in a 2D-3D system [75] and has since

been observed in electron-electron [74] and electron-hole [76, 77] DQWs and in normal metal-superconducting film structures [78].

Finally, several other structures on DQWs have been theorized and fabricated. These include antidot arrays [79], quantum dots [80], and 1D surface superlattices [81, 82]. The work on DQWs continues to increase due to the promise of new devices from these structures and due to the new phenomena that may be observed in them.

3. EXPERIMENTAL DETAILS

This chapter discusses the experimental details of this work. Section 3.1 lists the samples used and their basic characteristics. Sample processing is described in section 3.2 and finally section 3.3 describes the measurement systems used in this work.

3.1 Samples

Eight closely-coupled DQW samples were used in this work. All of the samples are symmetric (QWs of equal width) but they are somewhat out-of-balance at zero gate bias. Table 3.1 lists the sample characteristics, the sample geometry, and the chapter in which the measurements are discussed. The densities were determined by performing FFTs on R_{xx} versus $1/B_{\perp}$ as discussed in section 2.1.8. The mobilities are for both QWs in parallel with

TABLE 3.1. Sample parameters. For Δ_{SAS}, the measured values were obtained from (a) the anticrossing features, (b) the minimum density difference as a function of gate bias.

Sample	w / t (Å)	n (10^{11} cm^{-2})		μ_{total} (10^3 cm^2/Vs)	Δ_{SAS} (meV)		Geometry	Chapter
		n_1	n_2		meas.	theor.		
A	150 / 25	1.4	1.5	244	1.1[a]	1.4	H	4
B	100 / 35	1.2	1.2	90	1.8[a]	2.0	H	4
C	150 / 15	0.7	0.9	40	3.0[a]	3.4	H	4
D	125 / 10	2.2	0.0	215	---	7.6	H	4
E	150 / 15	1.0	1.9	310	2.3[b]	2.1	H	5
F	139 / 28	1.9	2.4	740	1.5[b]	1.5	VdP	5
G	150 / 15	1.0	1.9	310	2.3[b]	2.1	QPC	6
H	150 / 25	1.4	1.5	244	1.1[a]	1.4	QPC	6

no gate bias. The measured Δ_{SAS} were determined from the minimum density difference as a function of gate bias or from the anticrossing features as discussed in Chapter 4. The theoretical Δ_{SAS} were determined from a self-consistent Hartree calculation. Finally, the geometry is the channel geometry resulting from processing, where H is a Hall bar, VdP is a Van der Pauw square and QPC is a quantum point contact. The various geometries will be discussed in more detail later in this chapter.

3.2 Sample Processing

The purpose of processing is to define the conducting channel geometry, make ohmic contacts to the electron layers, and make Schottky gates. Standard semiconductor processing techniques are used in the fabrication of these samples. Details on GaAs processing may be found in Reference [83]. The steps necessary to fabricate a Hall bar are discussed in detail in the next few paragraphs. Then slight variations of these steps are discussed for the fabrication of Van der Pauw squares, quantum point contacts, and quantum wires.

The first step in fabricating a Hall bar is to define the conducting channel. Photoresist (PR) is spun (5 kRPM for 30 sec.) on a 5×9 mm sample and soft baked on a hot plate at 90°C for 90 seconds. Next the PR is exposed with UV light for 3.3 seconds with the conducting channel part of the sample covered by a mask. The PR is then developed in developer (1:5 400k:H_2O) for 60 seconds. The developer removes the exposed PR; while the unexposed PR remains on the sample surface as shown in Fig. 3.1(a). An oxygen plasma descum at 5 W for 90 seconds at 650 mTorr is used to remove any organic material in the exposed areas. Next the exposed semiconductor material is etched with phosphoric acid (1:4:45 H_3PO_4:H_2O_2:H_2O) for 90 seconds (etch rate $\approx$ 50 Å / sec) to remove the conducting layers. The PR protects the layers under it and, after the PR is removed in acetone, a bar-shaped mesa, with conducting layers in it, remains.

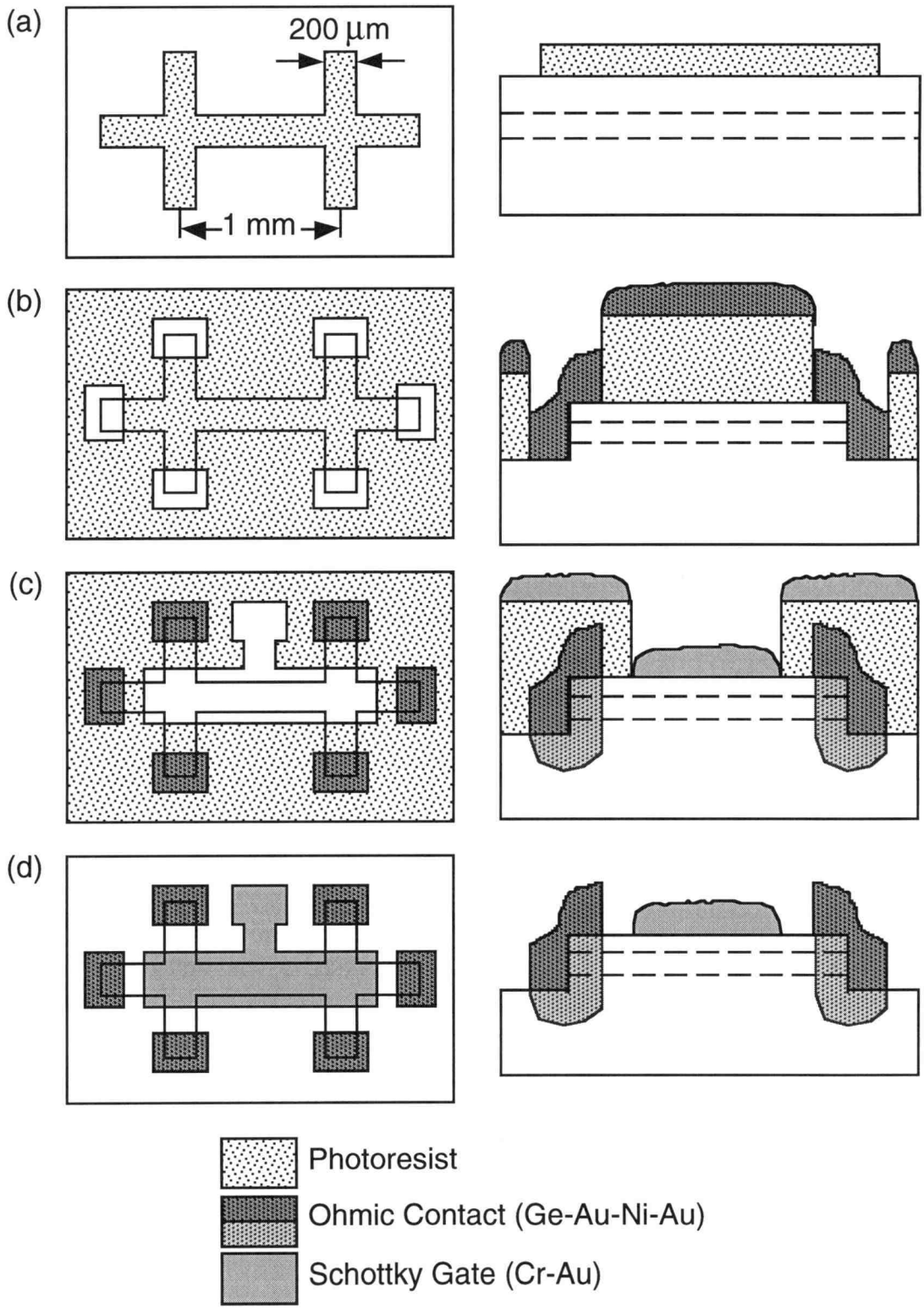

Fig. 3.1 Schematic top view (left column) and cross-sectional view (right column) of Hall bar during the various processing steps. (a) Mesa step before etching; (b) contact step before lift-off; (c) gate step before lift-off; and (d) finished sample.

The next step is to make ohmic contact to the conducting layers. Again PR is spun on the sample and baked on a hot plate. Then a mask with small openings at the ends of the arms of the Hall bar is aligned to the Hall bar and the PR is exposed with UV light through these holes. The PR is developed to remove the exposed PR as shown in Fig. 3.1(b). A plasma descum is done again to clean up the corners of the holes and a light etch is done in 20:1 H_2O:NH_4OH for 30 seconds to remove the native oxide on the exposed surface of the sample. The sample is then blown dry and immediately placed in the vacuum evaporator before the oxide can form again. Next, metal is evaporated over the entire sample and the PR is then removed in acetone. Metal on top of the PR is removed with the PR; while metal remains on the semiconductor surface. This process is known as lift-off and the right side of Fig. 3.1(b) shows the cross-section of the sample before the metal is lifted-off. The PR must be thicker than the metal and must have a side-wall profile that is vertical or has an over-hang so that the metal on the PR and that on the semiconductor are not connected.

For ohmic contacts to n-type GaAs, fours layers of metal are used: Ge (270 Å), Au (540 Å), Ni (140 Å), and Au (2000 Å) in that order. After the lift-off process is complete, the metal is annealed in an infrared rapid thermal annealer (RTA) at 420 °C for 90 seconds. The anneal causes the Ge and first layer of Au to diffuse into the semiconductor while the Ni acts as a barrier to prevent the top layer of Au from diffusing. The top layer of Au acts as a contact pad for soldering wires to the ohmic contact after sample fabrication is complete.

The final fabrication step is to make a Schottky gate for changing the sample electron density during experiments. A lift-off process is used in this step also. PR is spun and baked, and then exposed using a gate mask that is aligned to the previous levels. The PR is developed to open holes where the gate metal is desired as shown in Fig. 3.1(c). A descum and oxide etch are done before evaporating Ti (250 Å) and Au (2000 Å) onto the sample. The PR and unwanted metal are then lifted-off. The Ti is used to help the Au stick to the semiconductor surface. Fig. 3.1(d) shows the completed Hall bar.

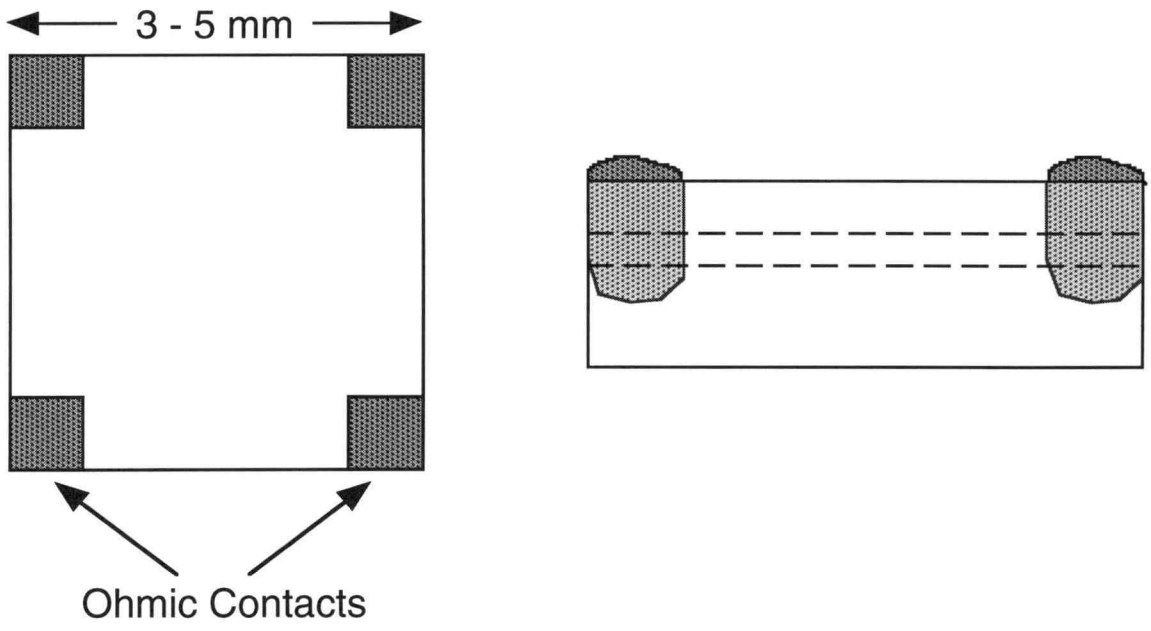

Fig. 3.2 Top view and cross-sectional view of Van der Pauw square.

Van der Pauw squares are easier to process because only ohmic contacts are needed. A Van der Pauw square is just a small, roughly square piece of semiconductor with ohmic contacts diffused into the corners as shown in Fig. 3.2. The metal used is typically In or In/Sn that is put on the corners with a small soldering iron, or alternatively small cylindrical slices of In/Sn wire that are placed on the corners with a pair of tweezers. After the metal is placed on the corners, it is diffused into the semiconductor using a thermal anneal. The anneal is done on a hot plate at 420° C for 5 minutes with 85% N_2 / 15% H_2 gas flowing over the sample. For high magnetic field experiments, the ohmic contacts must hang over the corners of the sample; otherwise, a Corbino-type geometry is inadvertantly produced and electrons in their cyclotron orbits will circle the contacts but not go into them [84]. Gates can also be deposited on the sample, but in the repesent work they are not used on the Van der Pauw squares. The fabrication of Van der Pauw squares is simpler than Hall

bars, but Van der Pauw squares have several drawbacks that will be discussed in the next section.

Quantum point contacts and quantum wires are similar to Hall bars, except the gate is very short with a tiny opening in it as shown in Fig. 3.3. This geometry is known as a split gate and the opening between the gates is less than 1 μm wide. The split gates are used to deplete the electron layers beneath them; leaving a very short, narrow conducting channel connecting two large reservoirs. The difference between quantum point contacts

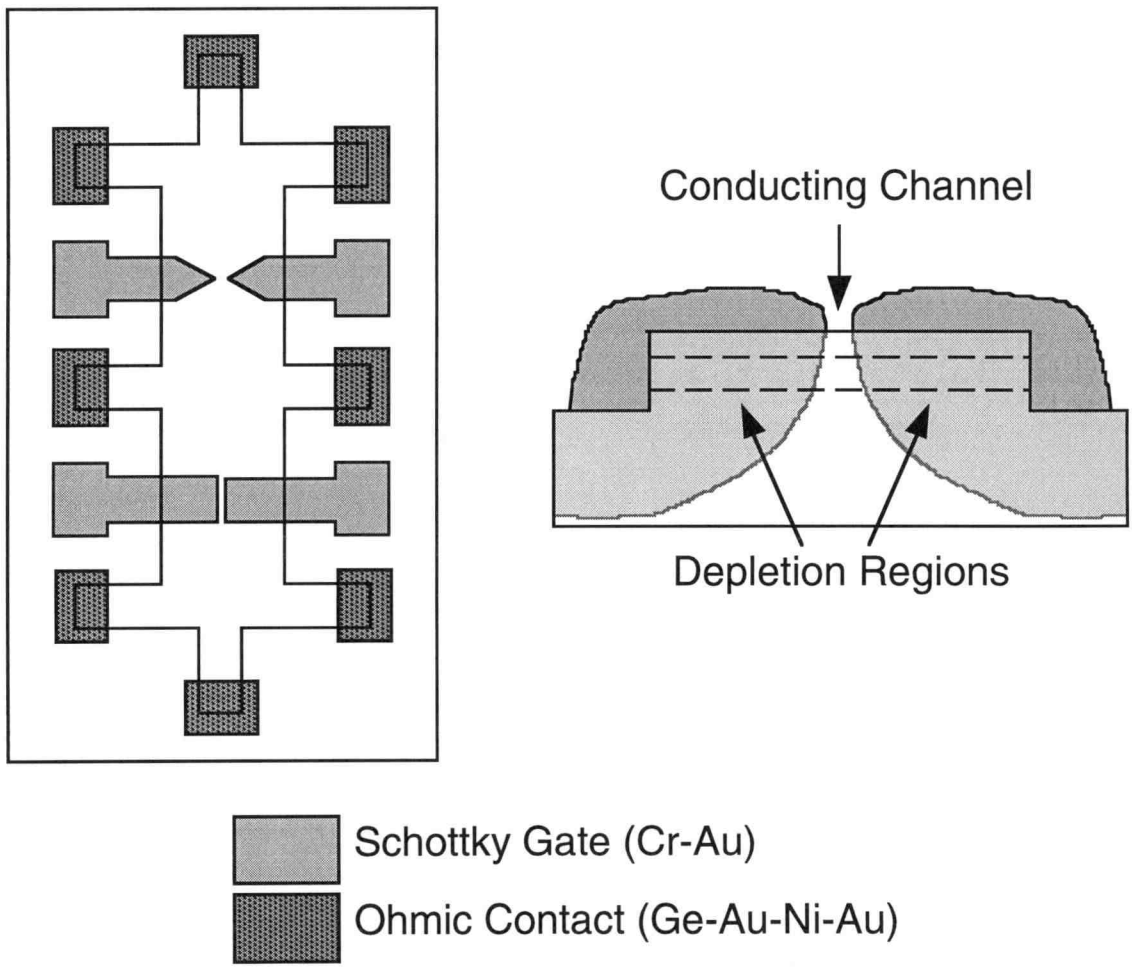

Fig. 3.3 Left: Top view of a quantum point contact (upper gates) and quantum wire (lower gates). Right: cross-sectional view of these devices showing a schematic of the approximate depletion region and the resulting conducting channel.

and quantum wires is the channel length, where quantum wires are longer than quantum point contacts The operation of quantum point contacts, which results in the quantization of the longitudinal resistance even at $B = 0$, and quantum wires will be discussed in detail in Chapter 6. The mesa etch and ohmic contact evaporation and anneal are the same for these devices as they are for Hall bars. The gate processing is slightly different because the opening between them is too small to define using optical lithography. Instead, electron beam lithography is used to define the gates because it has a much better resolution than optical lithography [20].

3.3 Experimental Setup

The experiments were performed in a pumped ^{3}He system with a base temperature T = 0.3 K and a 15 Tesla superconducting magnet . There are two main areas of concern in the experimental setup. The first is the measurement circuit, where here standard lock-in measurement techniques were used and will be discussed in section 3.3.1. The influence of the sample geometry will also be discussed in that section. The second area of concern is the orientation of the magnetic field with respect to the sample, where the various experiments require different magnetic field orientations. The different methods used to achieve these orientations are discussed in section 3.3.2.

3.3.1 Measurement Circuit

The measurement circuit must accurately measure R_{xx} and R_{xy} while using a sufficiently small excitation that the conduction electrons in the sample remain near equilibrium. In theory, this is accomplished by using an excitation that is on the order of $k_BT \approx 26$ μV for $T = 0.3$ K, where k_B is Boltzmann's constant. In practice, measurements are done at different excitation voltages and the highest voltage at which the results are

unaffected by the excitation is identified. Performing the measurements at equilibrium ensures that the Fermi surface concept can be used to analyze the results and that hot electron effects do not have to be considered. The wires from the instruments to the sample in the cryostat have a resistance of roughly 300 Ω, which can be comparable to the sample resistance at $B = 0$. To remove this lead resistance from the measurements, all of the measurements are done using four terminals. As shown in the schematic of Fig. 3.4, a small current is passed between two terminals at the ends of the Hall bar and a voltage is measured across two other terminals of the Hall bar. The current is generated by adding a large ballast resistor ($\approx 10 - 100$ MΩ) in series with the Hall bar and applying $V_{in} = 1$ V across this circuit. If the ballast resistor is much larger than the other resistances in the circuit ($\approx 10 - 20$ kΩ at high B), nearly all of the input voltage is dropped across the ballast resistor and the current through the sample is independent of the sample resistance.

The signal to noise ratio is increased by using phase sensitive detection. In this technique, an A.C. voltage at a frequency f_{ref} is used as the input voltage V_{in}. f_{ref} is typically in the range 5 – 100 Hz and is not a multiple of 60 Hz to avoid picking up 60 Hz line noise. The response of the sample at f_{ref} is then measured in-phase with the input voltage. Noise signals at frequencies other than f_{ref} are rejected and voltages smaller than 0.1 μV can be measured even when much larger noise signals are present. Using this technique, small voltage drops across the sample can be accurately measured while keeping the sample at equilibrium. In this case, the current can be $\approx 10 - 100$ nA and is determined by the values of V_{in} and the ballast resistor. The 10 kΩ resistor is used to measure the current flowing through the sample. V_{in} is generated with a lock-in amplifier and all of the voltages are measured with lock-in amplifiers referenced to V_{in}. The outputs from the lock-in amplifiers are measured with DMMs which are, in turn, read by a computer over the GPIB bus. This allows the data to be easily saved and analyzed on computer.

Hall bars are the standard geometry used in measurements on 2DEGs because they allow the accurate measurement of both R_{xx} and R_{xy}. The number of squares ($S = L/W$) of

the electron channel is defined as the ratio of the channel length (L) to width (W) and, for Hall bars, the number of squares can be accurately determined. Knowing the number of squares and R_{xx} allows the calculation of the sample mobility. In Van der Pauw squares, on the other hand, the number of squares is not well defined and thus it is more difficult to determine the mobility from the measurement of R_{xx}. In Van der Pauw squares, R_{xx} is measured by flowing current between the two contacts on one side of the sample and measuring the resistance along the opposite side. Due to fringing fields, S is not well-

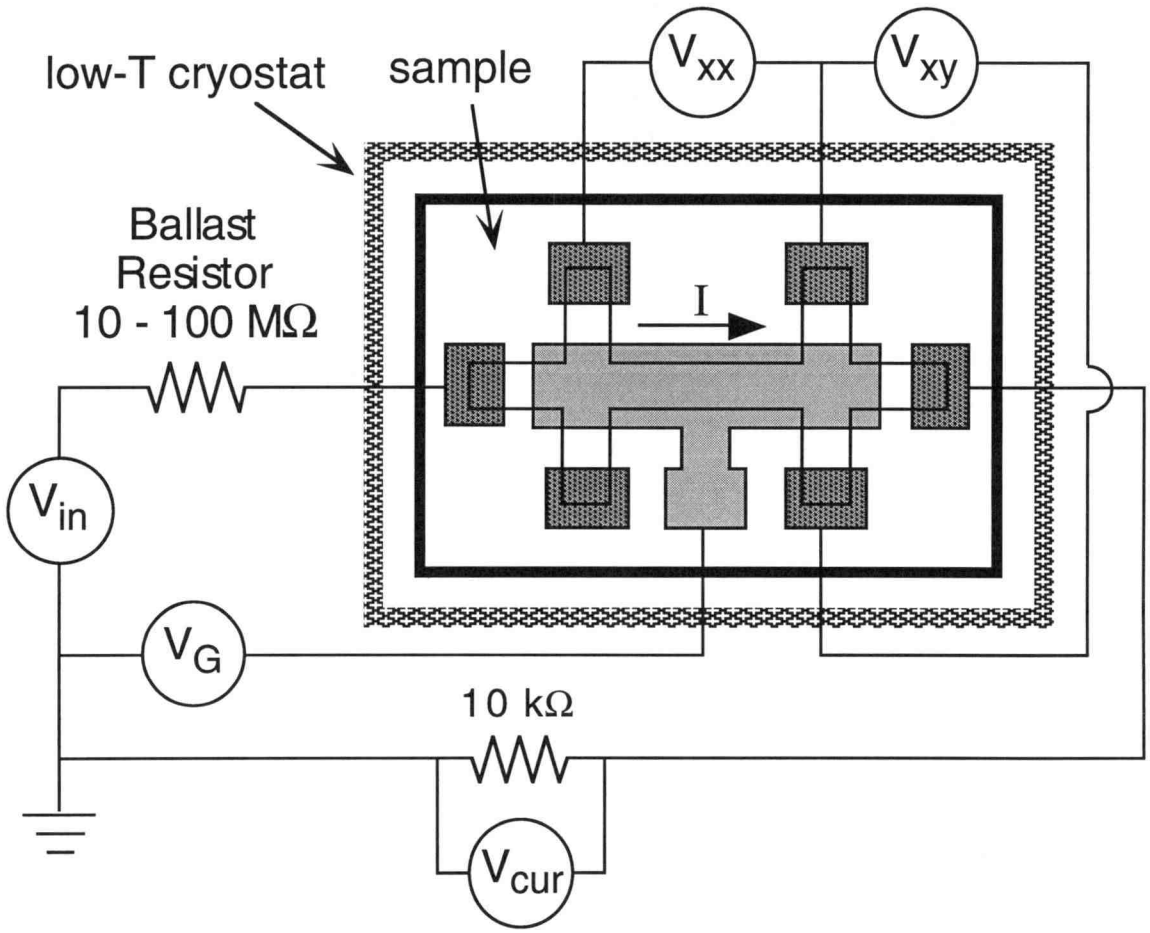

Fig. 3.4 Schematic diagram of the measurement circuit with the Hall bar being tested. V_{in} is the input A.C. signal, V_G is the D.C. gate bias, and the other voltages are measured in-phase with the input signal. Only the sample is in the low-T cryostat.

defined and is given by [85] $S = \ln(2)/(\pi f)$, where f is a correction factor for non-square samples and $f \approx 1$ for a square sample. A more accurate determination of R_{xx} is possible by repeating this measurement for each side of the sample. R_{xy} can not be independently measured with this technique; however, the combination of R_{xy} and R_{xx} can be measured by flowing current through opposite corners of the sample and measuring resistance between the other two corners.

3.3.2 Magnetic Field Orientation

The experiments or this thesis require several different magnetic field components ranging from parallel ($B_{||}$) to the plane of the QWs to perpendicular ($B_{\perp}$) to the plane and different angles between these two extremes. The sample is mounted on a stage that can be rotated from parallel to perpendicular to the magnetic field. First the rotation system will be described and then the rotation schemes for the different experiments will be discussed.

The rotation system was manufactured by Oxford Instruments and consists of a stepper motor outside the cryostat that turns a rod which extends into the cryostat and has a rotating mechanism at its end. The rotating mechanism is a Swedish rotator which consists of a spiral gear at the end of the rotating rod and a disk with gear teeth around its circumference as shown in Fig. 3.5. The sample is mounted on the disk along with a Hall probe that measures $B_{\perp}$ only. A second Hall probe is mounted on a stationary platform near the sample to measure B_T. These Hall probes are the only way for the computer to determine the angle of the sample. The angle can also be visually read from an analog display on the stepper motor with a resolution of 0.1° but an accuracy of only ≈ 0.5°. However, this display cannot be read by the computer and so is useful only for experiments in which a single, fixed angle is required.

The stepper motor is controlled with the rotator control box which can be run either manually or via a computer equipped with a signal generator board. Manual control gives

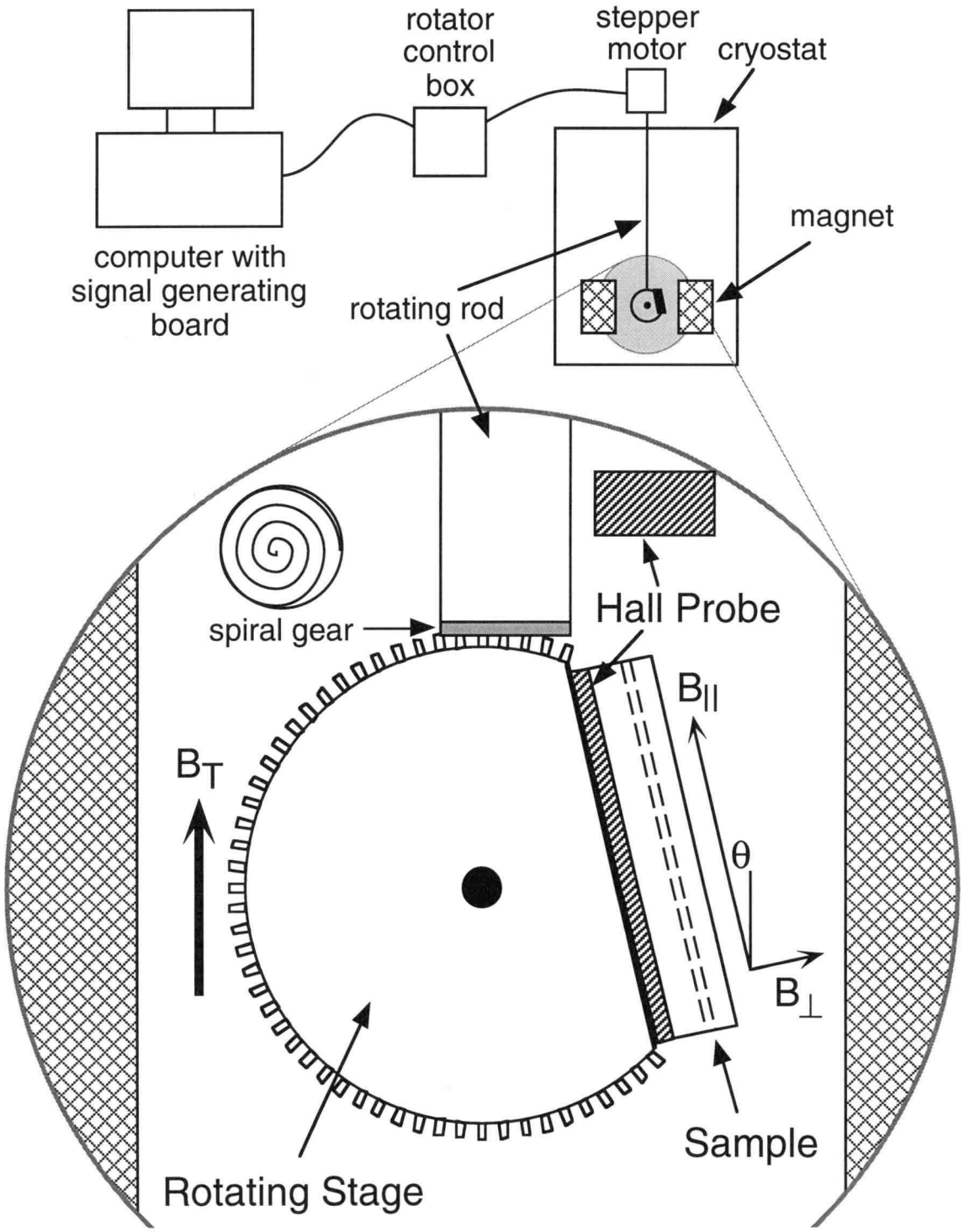

Fig. 3.5 Schematic of the rotation system with a blow-up of the rotating sample holder and magnetic field components.

a constant rotation rate, whereas computer control can give a variable rate. The signal generator board must be capable of producing both a D.C. voltage and a 5 V p-p square wave signal. The D.C. voltage determines the direction of rotation while the frequency of the square wave determines the rotation rate of the sample. Each pulse of the square wave signal rotates the sample an infinitesimal angle ($\Delta\theta \ll 0.1°$) and thousands of pulses are necessary to rotate the sample a measurable amount. However, with the signal generator board used here, the computer cannot count the number of pulses output by the signal generating board.

This leaves two methods for computer-controlled rotation to a specific angle or by a specific amount. The first is to use the Hall probes to measure the angle and rotate to a set angle. This method suffers from overshoot due to delays in the system. Back rotation at a slower rate can compensate for this but oscillation about the set point is a possibility which reduces the sample hold time at the base temperature. The other method uses a timed rotation at a given rate. Using this method, the sample can be reliably rotated by angles on the order of 0.1°.

Basic characterization of the samples requires only $B_\perp$, while $B_\parallel$ only is used in the experiments of Chapters 4 and 6. These are easily achieved in a single magnetic field and rotation is typically done manually in these cases. One of the experiments of Chapter 4 requires a large $B_\parallel$ with a small $B_\perp$-component. This is achieved by rotating the sample manually to the desired angle. However, for the experiments of Chapter 5, a constant $B_\parallel$ with changing $B_\perp$ is desired. Achieving this is difficult in a single magnetic field and two methods for doing this are discussed next.

In the first method, B_T is swept at a constant rate and the sample is simultaneously rotated at a variable rate determined by a feed-back loop so as to keep the measured $B_\parallel$ constant. $B_\parallel$ could be held constant within +0.003 and –0.011 T [86]. The rotation resulted in heating due to friction and for these measurements the sample temperature was $T = 0.5 \pm 0.2$ K. The rotating mechanism eventually failed due to poor gear design and was

replaced with a new mechanism from the manufacturer. However, the new mechanism had more friction and thus sample heating became a problem for this method and it could no longer be used reliably. Several measurements were done using this technique and but will not be discussed due to the higher quality data obtained using the second technique.

The other rotation method was inspired by Boebinger *et al.*'s work [55]. In this technique, the angle is held constant while B_T is swept and R_{xx} and R_{xy} are recorded. When the sweep is complete, θ is changed by a small amount ($< \approx 0.1°$) and, after the sample recools to the base temperature, another B_T sweep is done. While Boebinger *et al.* used only 50 different angle in their experiment, our use of the independently mounted Hall probes allowed us to use several hundred angles, achieving much greater resolution. Between scans the sample was rotated sufficiently slowly to keep the sample temperature below $\approx$ 1 K. After the series of scans is complete, traces of R_{xx} and R_{xy} for constant $B_{||}$ can be extracted from the data. To change the sample's angle, timed rotation at a constant rotation rate of $\approx 0.1°$ per minute was used. When the sample was nearly parallel to the magnetic field, where $B_{\perp}$ is relatively small and R_{xx} oscillates rapidly, a small $\Delta\theta \approx 01.°$ was used. While for $\theta \approx 45°$ and beyond a $\Delta\theta$ as large as $\approx 0.5°$ was used.

4. DOUBLE QUANTUM WELLS IN PARALLEL MAGNETIC FIELDS

This chapter describes electron transport experiments in DQWs subject to in-plane magnetic fields only. Previous experiments performed on DQWs subject to $B_{||}$ include measuring the in-plane conductance ($G_{||}$) in small $B_{||}$ [55], studying the $\nu = 1$ state in tilted magnetic fields [46], and also studying tunneling between the two QWs as a function of $B_{||}$ [63 – 65]. However, there is no previous work in which $G_{||}$ is experimentally studied as a function of large $B_{||}$. For this work, the theory and experiments went hand-in-hand. Lyo predicted that $G_{||}$ would exhibit one sharp feature as a function of $B_{||}$ [87]. However, in our experiments, two features were observed [88] and after modifying his theory, Lyo was able to accurately reproduce the experimental results [31]. Next, the electron effective mass was measured as a function of $B_{||}$ [86, 89, 90] and Lyo was able to reproduce these results also [91]. For the sake of clarity, Lyo's theoretical work on $G_{||}(B_{||})$ is presented in the first section followed, in the second section, by our experimental work. The last section discusses the experimental measurement and theoretical calculation of the electron cyclotron effective mass as a function of $B_{||}$. This work is exciting because, as will be seen in the next section, $B_{||}$ distorts the Fermi surface, giving it multiple components, whose sizes and occupancies are tunable with $B_{||}$.

4.1 Anticrossing of Dispersion Curves

In a DQW with the direction of current flow parallel to $B_{||}$, electrons moving within each QW will not feel a Lorentz force ($= -e\boldsymbol{v}_d \times \mathbf{B}$) because they are moving parallel to the magnetic field. However, during a tunnel event, electrons are moving perpendicular to the magnetic field and thus experience a Lorentz force, which gives them a momentum boost. Fig. 4.1 schematically shows electron motion in a DQW with the current parallel to $B_{||}$. Boebinger *et al.* [55] showed that the main effect of $B_{||}$ on a DQW is a linear

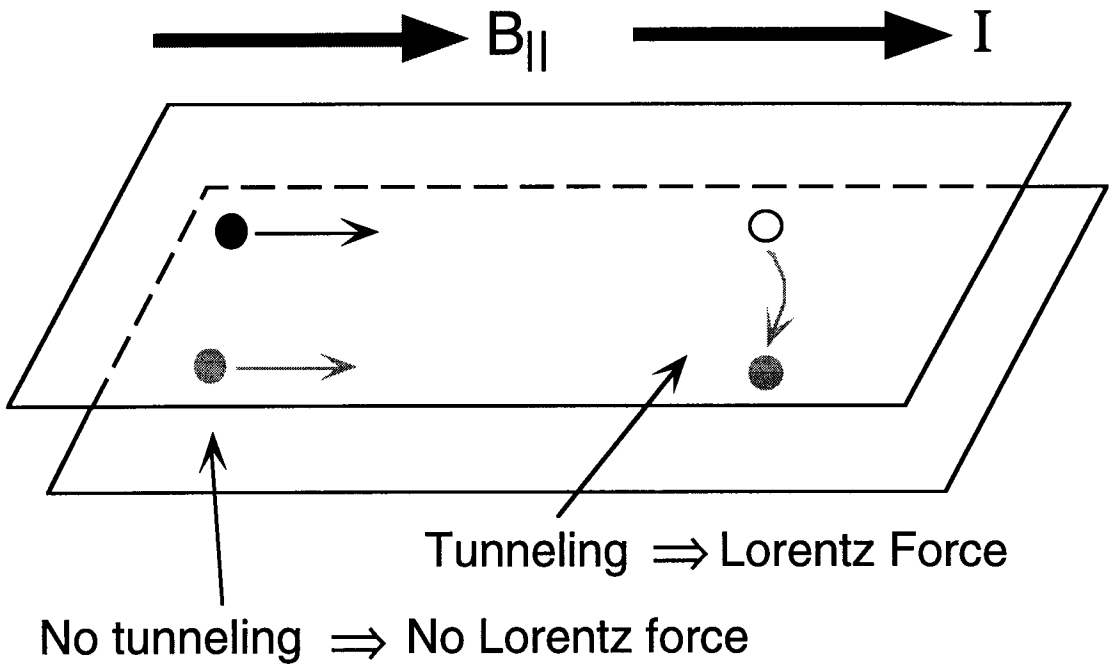

Fig. 4.1 Schematic depicting electron motion in DQW with the current parallel to $B_{||}$. The black circles represent electrons in the top QW and the gray circles represent electrons in the bottom QW. The open circle shows an electron that has tunneled from the top QW to the bottom QW.

transverse shift in the canonical momentum $\hbar\mathbf{k}$ of electrons in one QW relative the other, where the amount of shift is given by $\Delta k = edB_{||}/\hbar$. d is the distance between the two electron layers, which is typically determined from the distance between the two QW wavefunction maxima. Boebinger *et al.* [55] also showed that the resulting dispersion curve is slightly distorted at low $B_{||}$ and Lyo extended this work to the case of high $B_{||}$ [31]. The following analysis of DQWs subject to $B_{||}$ closely follows Lyo's work with some details added. For this work, $B_{||}$ is in the x-direction, y is the other in-plane direction, and z is perpendicular to the QW planes. The current can be run in either the x- or y-direction and the difference between these two variations will be discussed.

The kinetic energy in the direction of $B_{||}$ is $\varepsilon_x = (\hbar k_x)^2/2m^*$ and the Hamiltonian for the y- and z-directions is given by [31]

$$H = \frac{p_z^2}{2m^*} + \frac{\hbar^2}{2m^*}\left(k_y - \frac{z}{l^2}\right)^2 + V(z), \tag{4.1}$$

where for simplicity, an isotropic mass ($m^* = 0.067m_e = m^*_{GaAs}$) is used for both the QWs and the barriers and $l = (\hbar/eB_{||})^2$ is the magnetic length. The confinement potential ($V(z)$) is the superposition of the QW potentials $V_1(z)$ for QW1 and $V_2(z)$ for QW2. This Hamiltonian can, in general, be diagonallized numerically. However, only approximate solutions using a tight-binding solution, similar to that presented in Chapter 2, will be considered here. The narrow QW approximation will be used; meaning only the lowest subband in each QW will be considered.

The basis functions, $\varphi_1(z)$ and $\varphi_2(z)$, used in the tight-binding solution are the field-free ground subband eigenfunctions of the isolated single QWs. These subbands have eigenvalues ε_1 and ε_2, respectively. The tight-binding solution yields eigenvalues [31]

$$\varepsilon_{\pm}(k_y) = \frac{1}{2(1-S^2)}\left(H_{11} + H_{22} - 2SH_{12} \pm \sqrt{D}\right) \tag{4.2}$$

and

$$D = (H_{11} - H_{22})^2(1-S^2) + \left[(H_{11} + H_{22})S - 2H_{12}\right]^2, \tag{4.3}$$

where $S = \langle\varphi_1|\varphi_2\rangle$ and the matrix elements are given by

$$H_{nm} = \varepsilon_m\langle\varphi_n|\varphi_m\rangle + \langle\varphi_n|V_{m'}(z)|\varphi_m\rangle + \langle\varphi_n|V_B(z)|\varphi_m\rangle \quad (n, m=1, 2). \tag{4.4}$$

The prime on the subscript m indicates that $1' = 2$ and $2' = 1$, $V_B(z)$ is the potential due to the magnetic field and is given by $\hbar^2/2m^*(k_y - z/l^2)^2$, and $H_{12} \approx H_{21}$ is assumed.

The dispersion curve resulting from this calculation for a structure similar to sample A at high $B_{||}$ is shown as a three-dimensional plot in Fig. 4.2 [92]. As can be seen, the two QW dispersion curves are shifted with respect to each other in the k_y-direction. However, rather than crossing, the two QW dispersion curves anticross and a partial energy gap opens in the k_y-direction. In the k_x-direction, the dispersion remains parabolic. The

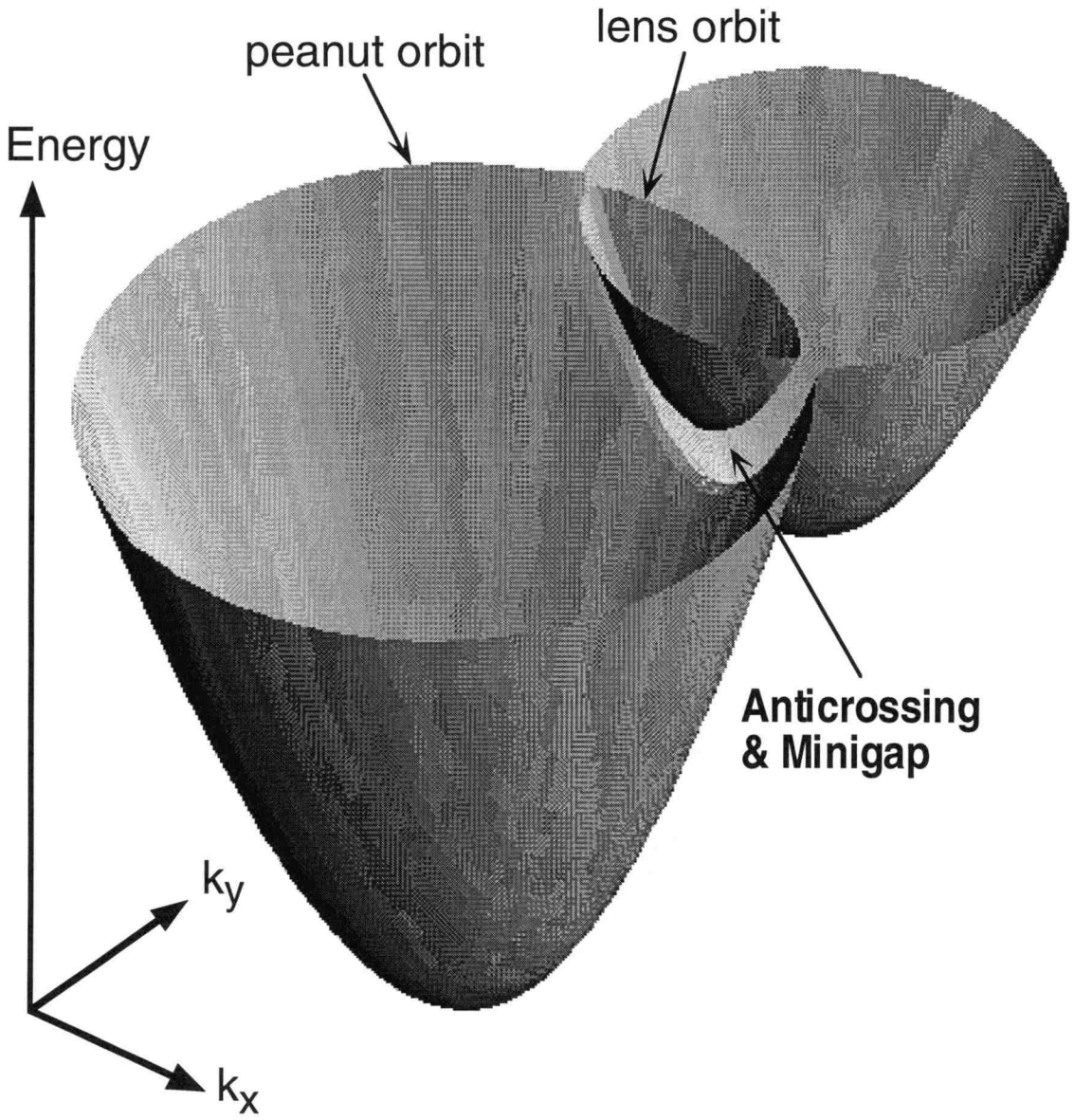

Fig. 4.2 Three-dimensional view of the dispersion curve of a closely coupled DQW subject to an in-plane magnetic field.

anticrossing results in a non-circular, multi-component Fermi surface consisting of an inner lens-shaped orbit and an outer peanut-shaped orbit when the chemical potential μ is above the energy gap. The point at the bottom of the gap is a saddle point, *i.e.*, its dispersion has positive curvature in the k_x-direction and negative curvature in the k_y-direction. The distortions in the dispersion result in distortions in the density of states (DOS), the Fermi

velocity and the electron effective mass. In particular, the DOS logarithmically diverges at the saddle point, as will be discussed shortly.

Fig. 4.3 shows the k_y-dispersion (column a) and DOS (column b) at three values of $B_{||}$ for a balanced DQW with d = 110 Å, w = 60 Å, and $V_1 = V_2$ = 280 meV. The dashed lines are for the case where tunneling is turned off and the DQWs are uncoupled. The solid lines are for coupled DQWs where tunneling is allowed. The upper panel is for $B_{||} = 0$ T, where the two uncoupled parabolas sit on top of one another. Coupling between the two QWs causes these two parabolas to repel one another and form the symmetric and antisymmetric states, as discussed in Chapter 2. The DOS is constant for each subband as expected.

The middle panel of Fig. 4.3 shows the case of $B_{||}$ = 6 T, where the two QWs have shifted with respect to one another and the energy gap has formed. Away from the anticrossing, the dispersion is similar to the uncoupled QWs and electrons are in QW states. While near the anticrossing, electrons occupy both QWs and are in the symmetric and antisymmetric states. The DOS shows significant distortions due to the distortions in the dispersion curve. At high energy, when both Fermi surface orbits are occupied, the total density of states is constant, but the DOS for each orbit varies slightly. As the energy is decreased, the lens orbit becomes de-occupied and just below 5 meV it is totally empty and the DOS shows a step decrease at this point. As the energy is further decreased, the saddle point is approached and the DOS has a logarithmic singularity.

The lower panel is for $B_{||}$ = 9 T and shows that as $B_{||}$ is increased the energy gap moves to higher energy. In practical cases, the energy is constant at μ, and increasing $B_{||}$ increases the size of the peanut orbit, decreases the lens orbit, and moves the energy gap and the corresponding features in the DOS to higher energy. The gap can be moved up so that μ resides in the gap and the resulting Fermi surface consists of only the peanut orbit. Further increasing $B_{||}$, moves the gap above μ and the dispersion becomes two uncoupled parabolic branches which have a constant DOS.

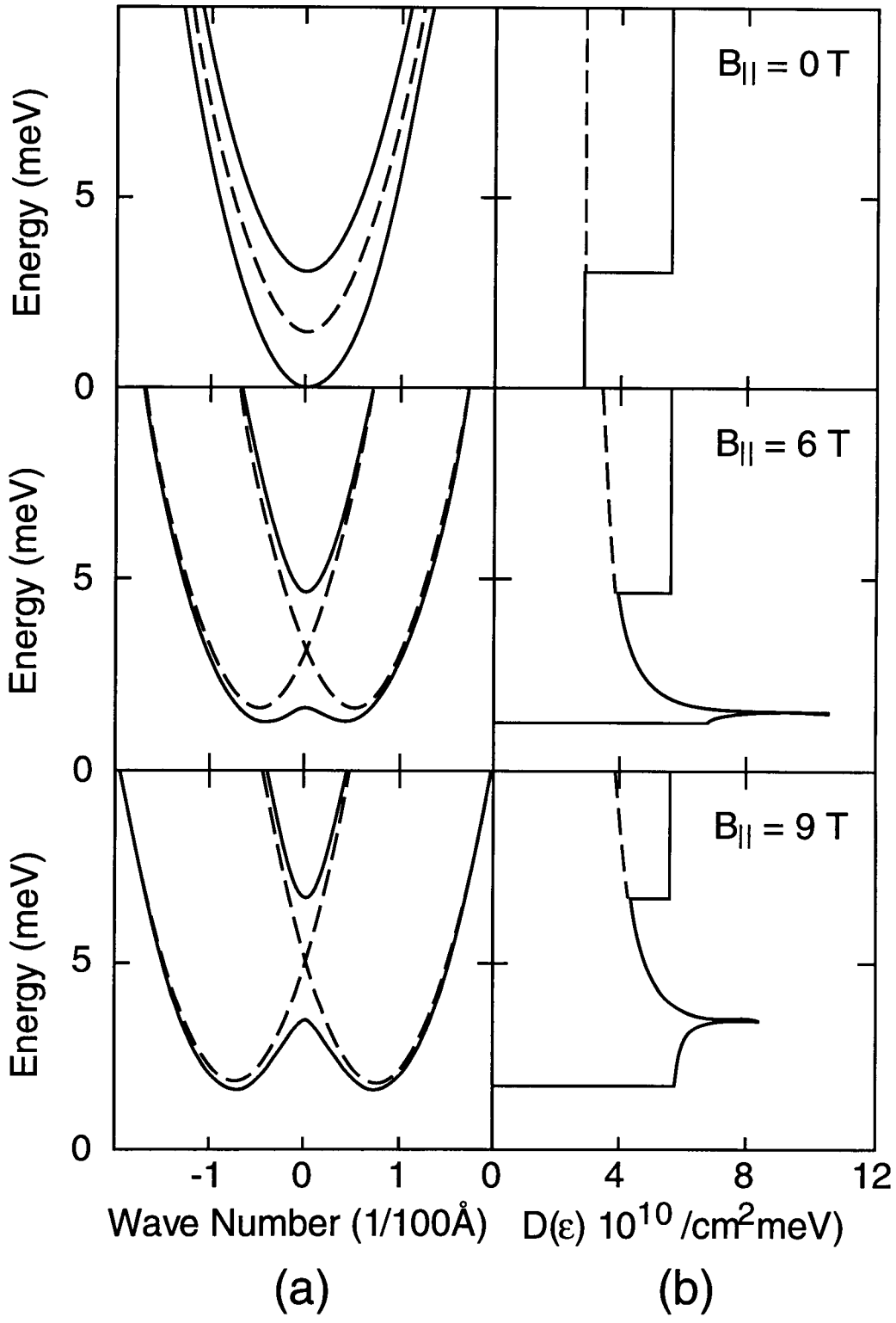

Fig. 4.3 Calculated dispersion curve (a) and density of states (b) for a balanced DQW structure at three different magnetic fields. top: $B_{||} = 0$ T; middle: $B_{||} = 6$ T; lower: $B_{||} = 9$ T.

Another feature of Fig. 4.3 is that the energy gap remains roughly constant with $B_{||}$. From equation 4.2, we see that the energy gap E_G is given by $\sqrt{D}/(1-S^2)$, which is $\approx \sqrt{D}$ because $S \approx 0.01$ and $S^2 \ll 1$. For balanced DQWs at $B_{||} = 0$ T, $E_G = \Delta_{SAS}$ and it can be shown from equations 4.2 – 4.4 that $E_G \approx 2[\langle\varphi_1|V_2|\varphi_1\rangle - \langle\varphi_1|V_1|\varphi_2\rangle]$. This approximation also holds for $B_{||} \neq 0$ and therefore, $E_G \approx \Delta_{SAS}$ at all $B_{||}$ for balanced DQW. Also, the minimum energy gap always occurs half way between the two displaced parabloids, which is defined here as $k_y = 0$.

The situation is slightly more complicated for unbalanced DQWs and is shown in Fig. 4.4 for three characteristic values of $B_{||}$. This calculation is for a DQW with w = 150 Å, t = 25 Å, V_1 = 280 meV, and V_2 = 278 meV, corresponding closely to sample A with $V_G \approx$ –0.1 V [88]. The upper panel again shows $B_{||}$ = 0 T. In this case, $E_G \approx (E_{1,2}^2 + \Delta_{SAS}^2)^{1/2}$ [31], where $E_{1,2} = |\varepsilon_1 - \varepsilon_2|$ and the same definition of Δ_{SAS} is used as above. The middle panel shows the case where $B_{||}$ = 0.7 T and the two uncoupled Fermi circles touch tangentially on the inside. The two curves anticross, but an energy gap does not form and the total DOS is unchanged, although the individual subband DOS change slightly. This behavior is known as a type I anticrossing [31]. In the lower panel ($B_{||}$ = 7.5 T), the uncoupled circles touch tangentially on the outside and the energy gap has formed. The anticrossing in this case is known as a type II anticrossing. The energy gap has decreased and becomes $E_G \approx \Delta_{SAS}$. For this unbalanced DQWs, the gap does not occur midway between the two parabloids ($k_y = 0$), but occurs at $k_y \approx$ 1e7 m^{-1}, with the gap approaching $k_y = 0$ as $B_{||}$ increases. The DOS is similar to the balanced DQW case, except that at low energy there is a step decrease when one QW becomes de-occupied before the other QW.

Lyo [31] calculates the in-plane conductance $G_{||}(B_{||})$ in the relaxation-time approximation. (Another group later calculated the conductivity using Boltzmann kinetic equations [93] with similar results.) In the direction of applied electric field $\mathbf{u}=\mathbf{E}/|\mathbf{E}|$,

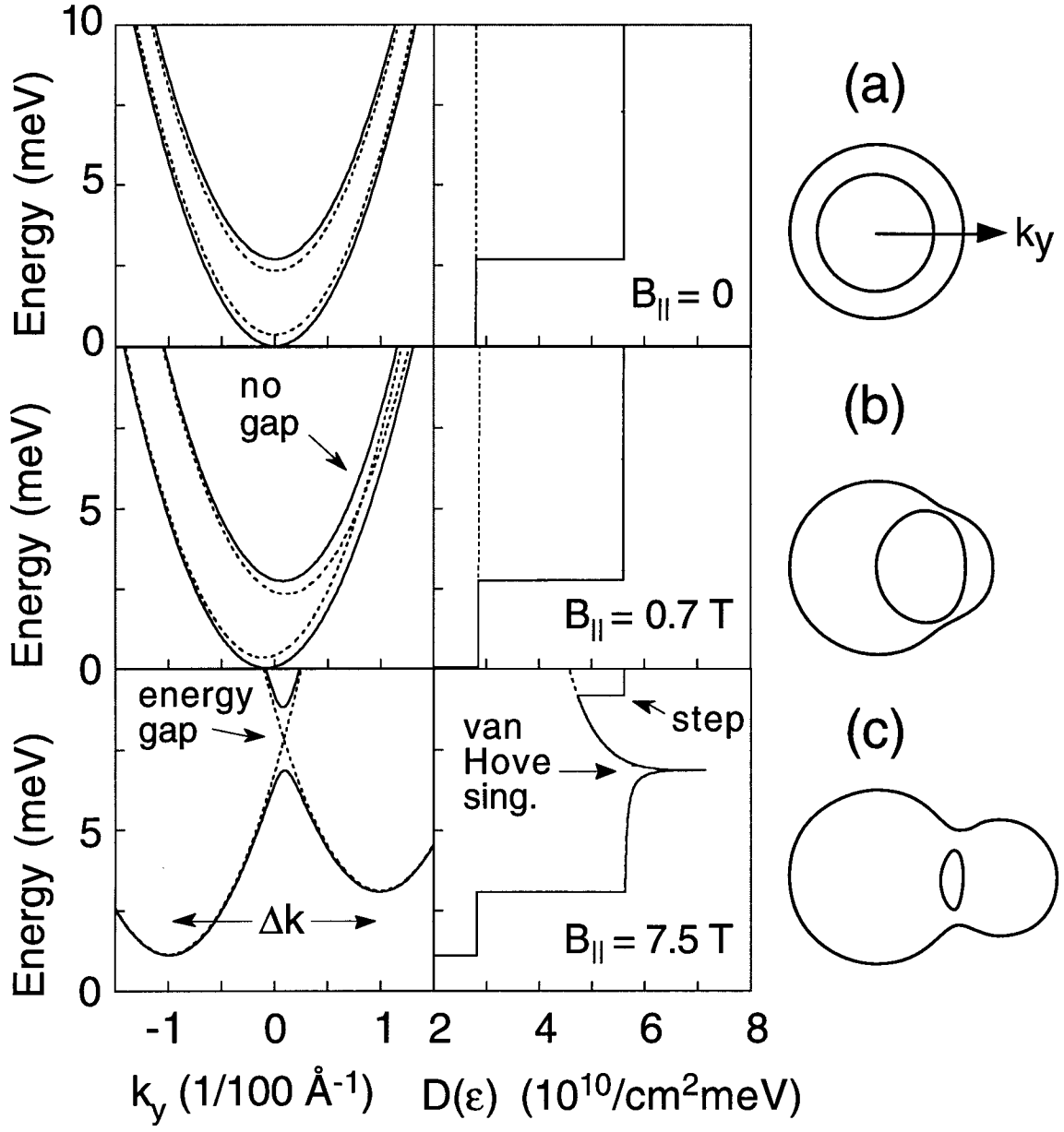

Fig. 4.4 Calculated dispersion curve (left column), density of states (middle column), and Fermi surfaces (right column) for an unbalanced DQW structure at three characteristic magnetic fields. top: $B_{||}$ = 0 T; middle: $B_{||}$ = 6 T where the uncoupled Fermi circles touch tangentially on the inside; lower: $B_{||}$ = 9 T where the uncoupled Fermi circles touch tangentially on the outside.

$$G_{||} = \frac{2e^2}{A}\sum_{\mathbf{k}} \left(\mathbf{u}\cdot\mathbf{v}_{\mathbf{k}}\right)^2\left[-f'_{\mathrm{k}}\right]\tau_{\mathbf{k}}, \tag{4.5}$$

where

$$\tau_{\mathbf{k}}^{-1} = \frac{2\pi N_I}{\hbar} \sum_{\mathbf{k}} \left\langle |V_{\mathbf{k}'\mathbf{k}}(z_i)|^2 \right\rangle \delta(\varepsilon_{\mathbf{k}} - \varepsilon_{\mathbf{k}'}) \tag{4.6}$$

for delta-potential impurities (surface roughness or short-range impurity potentials), $\mathbf{v}_{\mathbf{k}} = \hbar^{-1}\nabla_{\mathbf{k}}\varepsilon_{\mathbf{k}}$, $\varepsilon_{\mathbf{k}} = \varepsilon_x(k_x) + \varepsilon_{\pm}(k_y)$, $\mathbf{k}$ includes implicitly the indices $\pm$ for the upper and lower energy branches, A is the cross-sectional area of the QWs, and $f'_{\mathbf{k}}$ is the energy derivative of the Fermi function. Here N_I is the total number of static scattering centers randomly

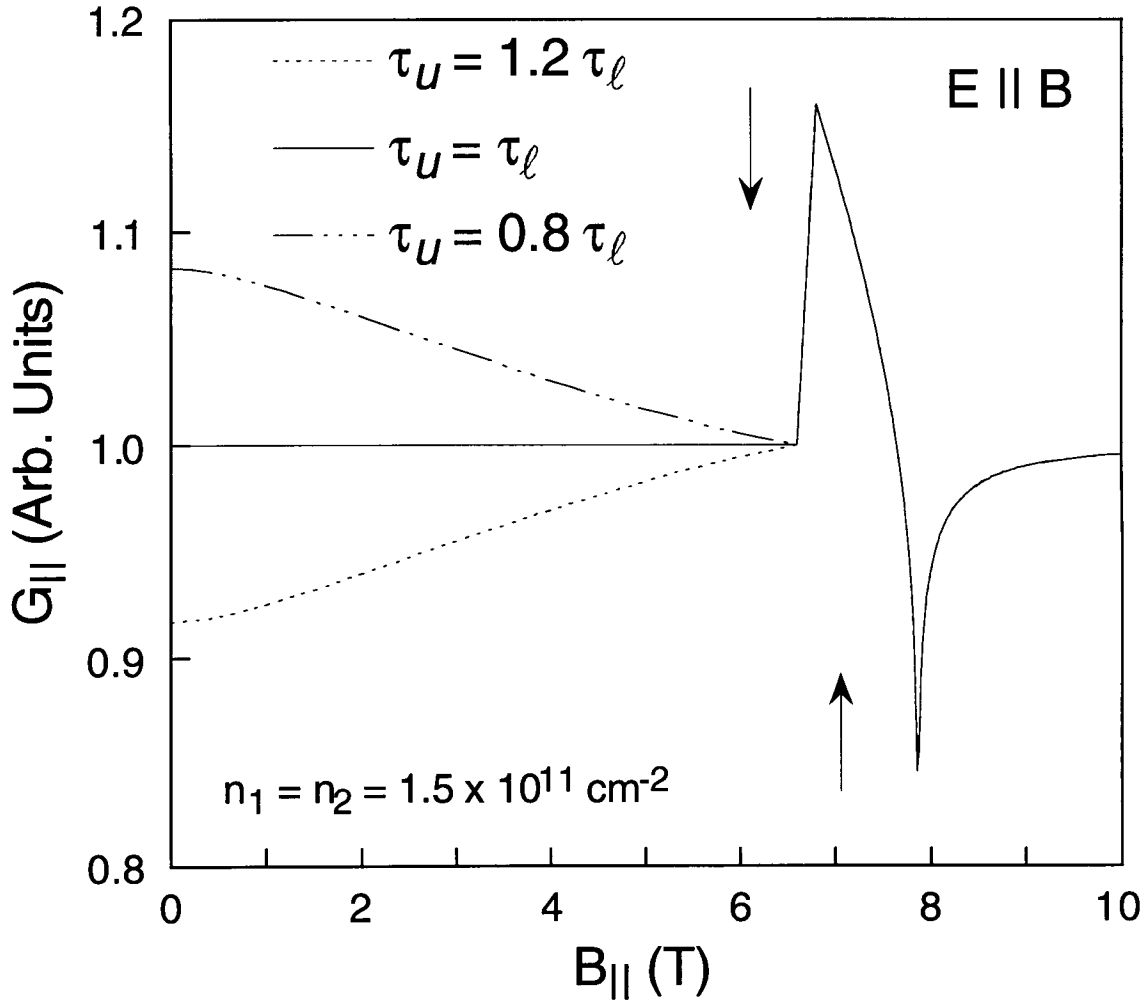

Fig. 4.5 Calculated $G_{||}$ as a function of $B_{||}$ for a symmetric DQW similar to sample A at $V_G \approx 0$ V. Three different ratios of scattering times in the upper τ_u and lower τ_l branches are shown. The arrows indicate positions of the maximum and minimum when the Hartree potential is included.

distributed in the x-y directions but distributed in a certain probability distribution in the z-direction. $V_{\mathbf{k}'\mathbf{k}}$ represents the matrix element of the potential from an impurity at $z = z_i$ and has a slow momentum dependence through B-induced k_y-sublevel mixing. The angular brackets in equation 4.6 denote the average over the impurity distribution. Lyo obtains $\tau^{-1}(\varepsilon) = \pi V_I^2 N_I D(\varepsilon)$ by ignoring the momentum dependence of $V_{\mathbf{k}'\mathbf{k}} = V_I$ where $D(\varepsilon)$ is the DOS including spin.

Fig. 4.5 shows an evaluation of equation 4.5 [88] for w = 150 Å, t = 25 Å, and $n_1 = n_2 = 1.5 \times 10^{11}$ cm^{-2}, corresponding to sample A at $V_G \approx 0$ V. Three different ratios of the scattering times in the upper (τ_u) and lower (τ_l) energy branches are shown. $G_{||}(B_{||})$ shows two sharp features at high $B_{||}$. The first is a maximum and corresponds to the lens orbit moving above μ. When the lens orbit is occupied there is significant scattering into low velocity states in this subband. As the lens moves above μ, the scattering rate suddenly decreases and a maximum occurs in $G_{||}$. The second feature is a minimum that occurs when the saddle point reaches μ. The DOS at the saddle point has a logarithmic divergence and these states have zero velocity, thus increasing the scattering rate and causing a minimum in $G_{||}$. There are no distinct features at the type I anticrossing, as expected. The calculation uses the QW center-to-center distance for d (= 175 Å). However, electron-electron interactions will push the two electron layers away from one another, causing d to increase. In a self-consistent Hartree calculation, the effective d is increased from 175 Å to 195 Å. The positions of the features using the increased d are indicated by the arrows in Fig. 4.5.

The velocity $\mathbf{v}_\mathbf{k}$ is equal to $\hbar^{-1}\nabla_\mathbf{k}\varepsilon_\mathbf{k}$, where for parabolic dispersion, this reduces to $\mathbf{v}_\mathbf{k} = (\hbar k_x/m^*)\mathbf{x} + (\hbar k_x/m^*)\mathbf{y}$. Here, the velocity is proportional to the wavevector. Far from the anticrossing, the DQW dispersion is parabolic and this expression holds. Fig. 4.6 shows the velocity for a symmetric DQW, with the effects of the anticrossing ignored. As can be seen, electrons on the lens have a much lower velocity, and thus carry less current, than electrons on the peanut orbit. As $B_{||}$ increases and the size of the lens decreases, the

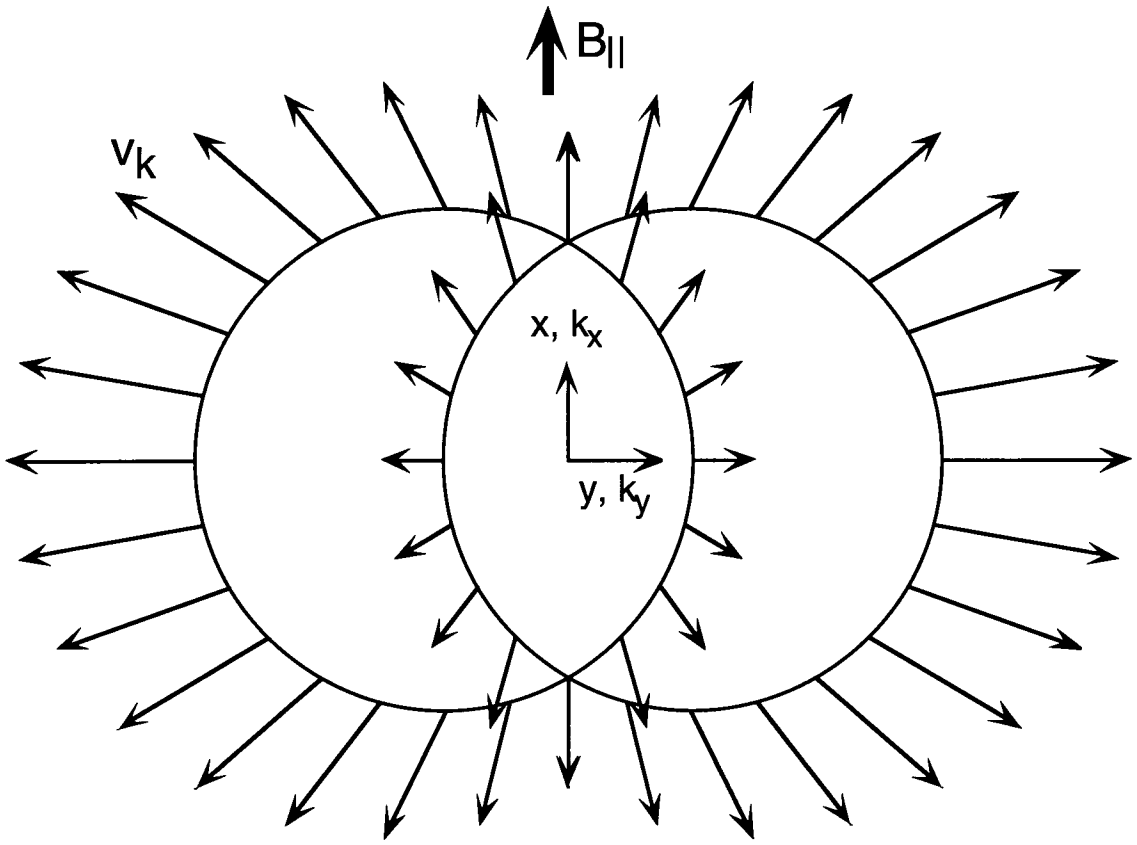

Fig. 4.6 Plot of the magnitude and direction of $\mathbf{v_k}$ as a function of wavevector superimposed on the Fermi surface. The velocity of electrons on the lens is much smaller than that on the peanut orbit. Also, The y-components of $\mathbf{v_k}$ are seen to be larger than the x-components.

velocity of electrons on the lens orbit will decrease correspondingly. This graphically shows how the lens orbit suppresses the conductance when it is occupied and the nature of the conductance peak that occurs when the lens moves above the chemical potential.

4.2 Experimental Observation of Anticrossing

In the previous section, the theoretical framework for these experiments is presented. Next, the experimental measurement of the in-plane conductance as a function of in-plane

magnetic field is presented, with comparison to Lyo's calculations. After that, the density dependence of the in-plane conductance is examined and a method for measuring Δ_{SAS} is described.

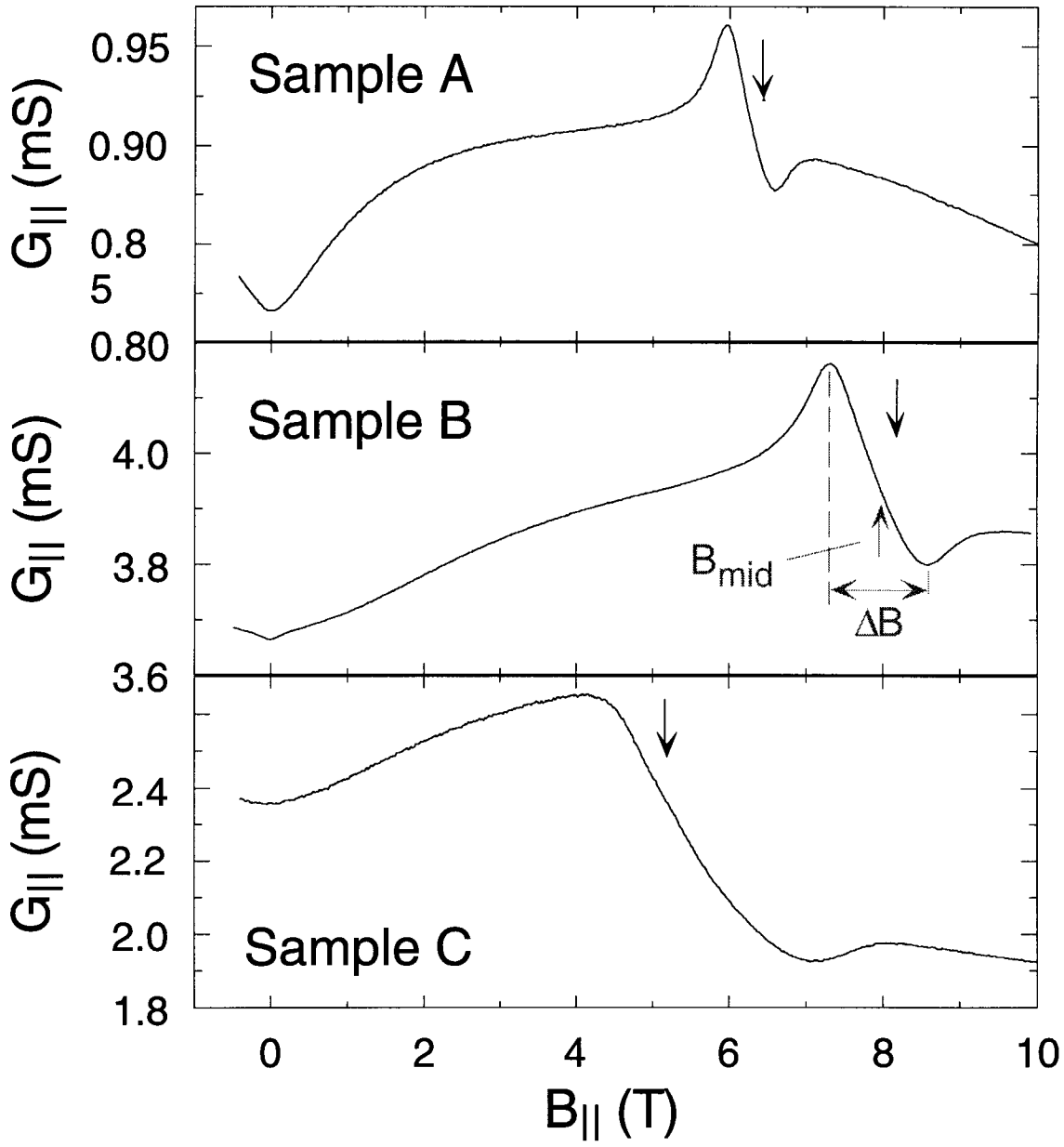

Fig. 4.7 Measured $G_{||}$ as a function of $B_{||}$ for samples A, B, and C. The dark arrows indicate where the uncoupled Fermi circles touch tangentially on the outside. The definitions of B_{mid} and ΔB are shown in gray on sample B.

4.2.1 In-Plane Conductance as a Function of In-Plane Magnetic Field

The in-plane conductance of Hall bars on samples A, B, and C was measured as a function of in-plane magnetic field and gate bias [88]. Fig. 4.7 shows $G_{||}(B_{||})$ for these samples. As can be seen, all three show the features due to the edges of the energy gap crossing the chemical potential. The features are smaller and rounded compared to theory due to damping. For sample A, the maximum appears at $B_{\max} \approx 5.8$ T, followed by a sharp minimum at $B_{min} \approx 6.4$ T. The calculated $G_{||}$, including corrections due to the Hartree potential (see Fig. 4.5), gave values of $B_{max,min} \approx 6.0$ T and 7.0 T, which are in excellent agreement with the measured data. The arrows in Fig. 4.7 indicate the field at which the two uncoupled Fermi circles touch tangentially on the outside, where $B_{||} = ed(k_1+k_2)/\hbar$ and $k_{1,2}^2 = 2\pi n_{1,2}$. These are very close to the mid-point between the two features (B_{mid}). This point is discussed in more detail below. As will be seen in the second half of this section, when the top QW is depleted, $G_{||}$ is weakly dependent on $B_{||}$ and is monotonic for $B_{||} < 14$ T. This indicates that the features are due to inter-QW interactions. Also, these features can not be due to the formation of cyclotron orbits within the individual QWs which are semiclassically expected when $B_{||} > 4\hbar/ew^2$ ($\approx$ 12 T for sample A).

The above results were obtained for an angle $\theta = 0°$ between $B_{||}$ and the direction $\mathbf{u}$ of the applied electric field $\mathbf{E}$. A large anisotropy is expected in $G_{||}$ with θ due to the highly anisotropic Fermi surface [93], which causes anisotropy in the $(\mathbf{u} \cdot \mathbf{v_k})^2$ factor in equation (4.5). The origin of this anisotropy can be seen from a plot of the velocity $\mathbf{v_k}$ as a function of wavevector and superimposing it on a graph of the Fermi surface, as is done in Fig. 4.6. As can be seen in the figure, the velocity components in the y-direction are much larger than the velocity components in the x-direction. Therefore, the $(\mathbf{u} \cdot \mathbf{v_k})^2$ factor is larger when the electric field is perpendicular to $B_{||}$, which results in a larger conductance for this orientation. The angular dependence of $G_{||}$ is investigated using a piece of sample B that is

processed with a Hall bar that has several arms at different angles. The inset of Fig. 4.8 shows the modified Hall bar along with the directions of **E** and $B_{||}$. Because these measurements were all done on the same sample, the residual $B_{\perp}$ due to angular offset was equal for all of these measurements and was kept below 0.005 T [88]. Fig. 4.8 shows the results of these measurements for all four angles used [88]. As expected, $G_{||}$ shows a large degree of anisotropy. The size of the anticrossing features for $\theta = 90°$ are nearly a factor of three larger than for $\theta = 0°$. At a point just below $B_{||} = 4$ T, the conductances for all four

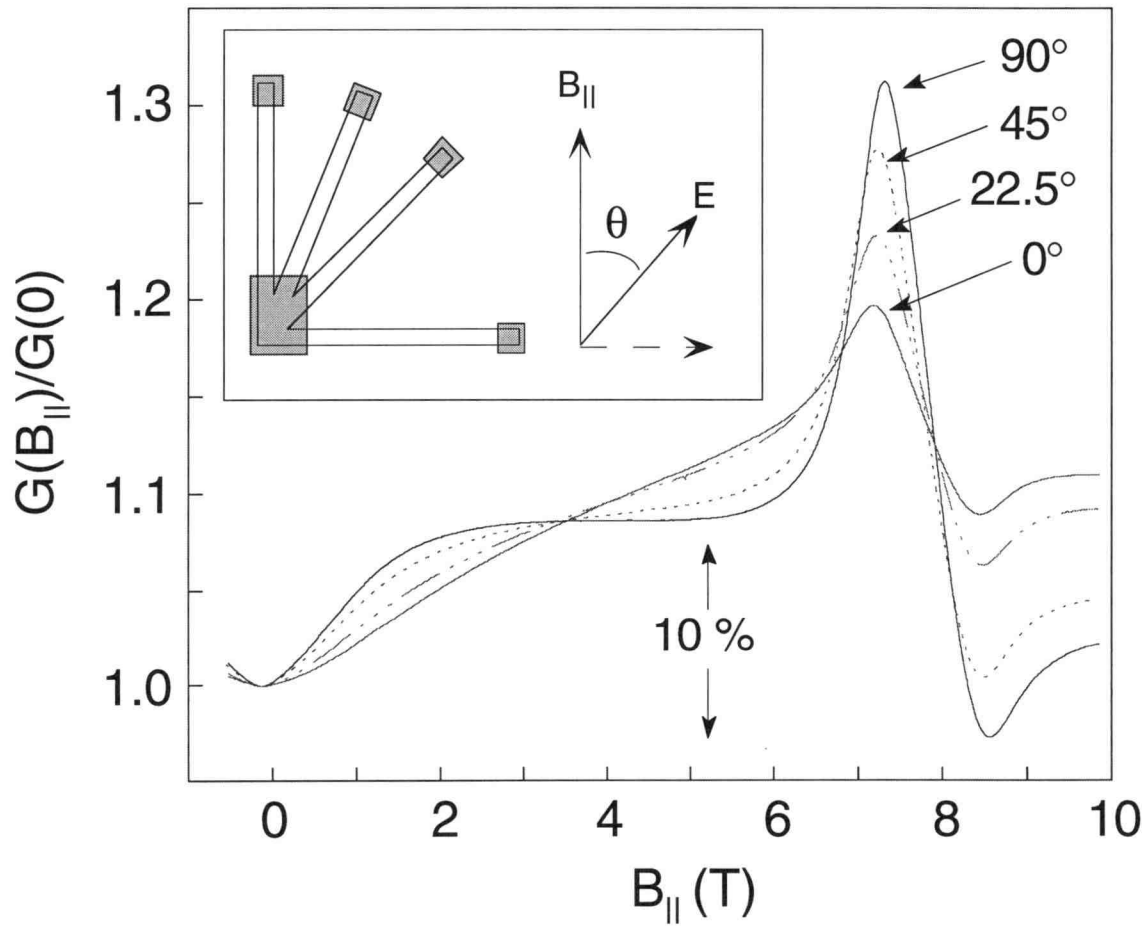

Fig. 4.8 Normalized $G_{||}$ of sample B at four different angles θ between the direction **u** of the electric field and $B_{||}$. The inset shows the modified Hall bar to investigate the angular dependence of the anticrossing features. The directions of $B_{||}$ and **E** are also shown.

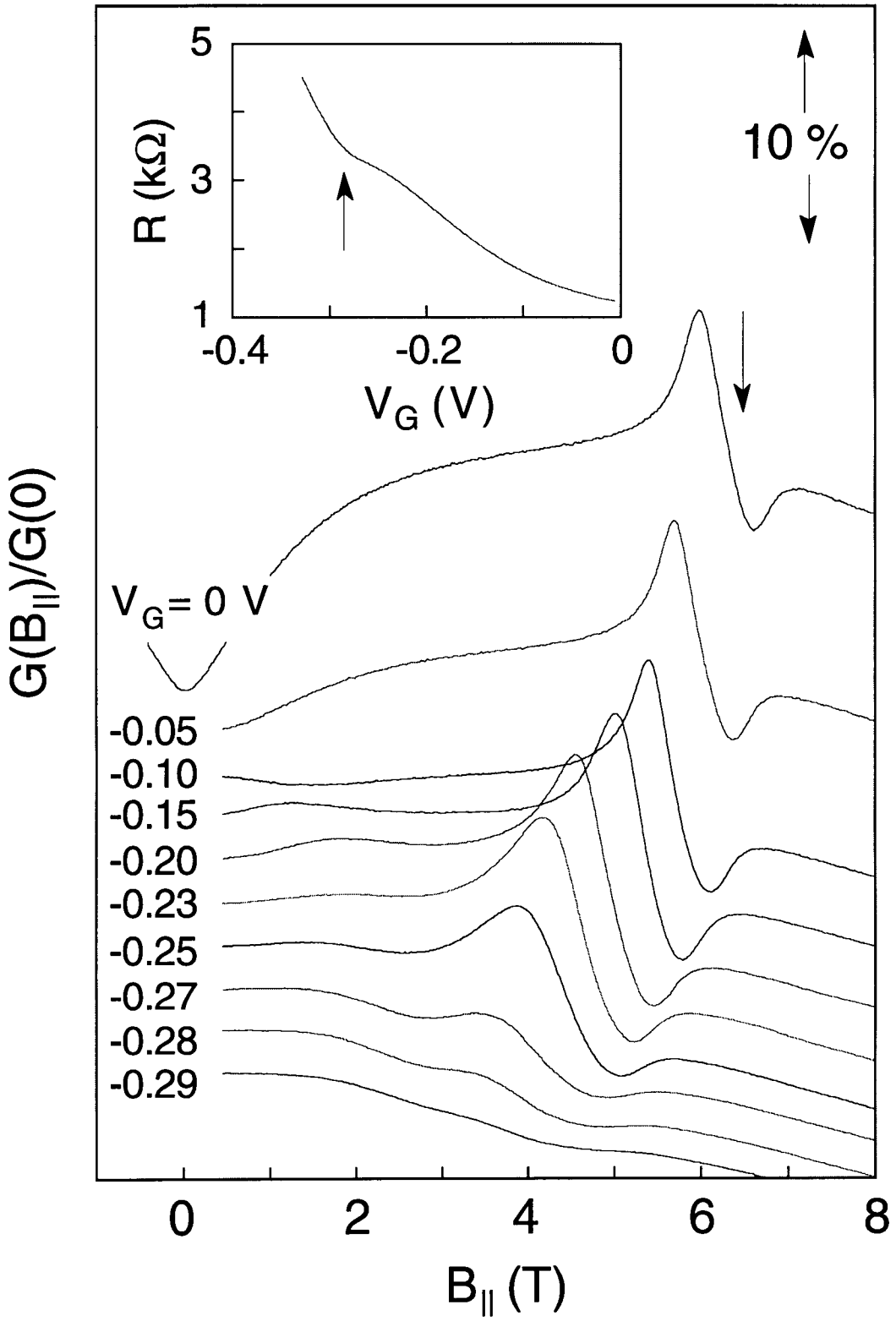

Fig. 4.9 Normalized $G_{||}$ of sample A at several different gate biases, offset from one another by 2%. Inset: zero-field resistance versus gate bias.

angles used are equal to each other, indicating that G is independent of angle at this point [94].

4.2.2 Gate Bias Dependence of In-Plane Conductance

This sub-section discusses the gate bias dependence of the anticrossing features. Fig. 4.9 shows the anticrossing features for several values of top gate bias V_G for sample A with $\theta = 0°$ [88]. The mid-point between the features is defined as B_{mid} and the separation is $\Delta B = B_{min} - B_{max}$ as indicated in Fig. 4.7. As V_G decreases, both features move to lower $B_{||}$ (*i.e.*, B_{mid} decreases), with B_{max} moving more rapidly than B_{min} (*i.e.*, ΔB also increases). The strength of the features also decreases rapidly when $V_G < -0.25$ V and the features essentially disappear when the top QW is depleted at $V_G = V_{depl} \approx -0.29$ V, as shown in the inset of Fig. 4.9. To a first approximation, negatively biasing V_G linearly decreases the top QW density n_1 while leaving the bottom QW density n_2 unchanged. This approximation is good when the DQW is unbalanced, however, it breaks down for strongly coupled DQWs which are near balance. As V_G decreases, the bottom of the top QW dispersion curve is raised relative to the bottom of the other QW dispersion, thus reducing the size of the top QW Fermi surface. This means a smaller **k**-space shift ($\Delta k = edB_{||}/\hbar$) is needed to cause the two uncoupled Fermi surfaces to touch tangentially on the outside as sketched in Fig. 4.10. Thus the features appear at lower $B_{||}$ with decreasing V_G. The increase of ΔB with decreasing $B_{||}$ is not as easily described with a physical picture. The gate bias dependence of B_{mid} and ΔB for all three samples are shown in Fig. 4.11 and next a simple model accounting for this dependence is developed [88].

We first model the gate dependence of B_{mid} using simple theory. B_{mid} occurs when μ is at the center of the energy gap and the two uncoupled QW Fermi surfaces touch tangentially on the outside, where $\Delta k = k_1 + k_2$. Using $k_{1,2} = (2\pi n_{1,2})^{1/2}$, $n_1 = C_G/e(V_G - V_{depl})$, and assuming that n_2 is constant, this model gives

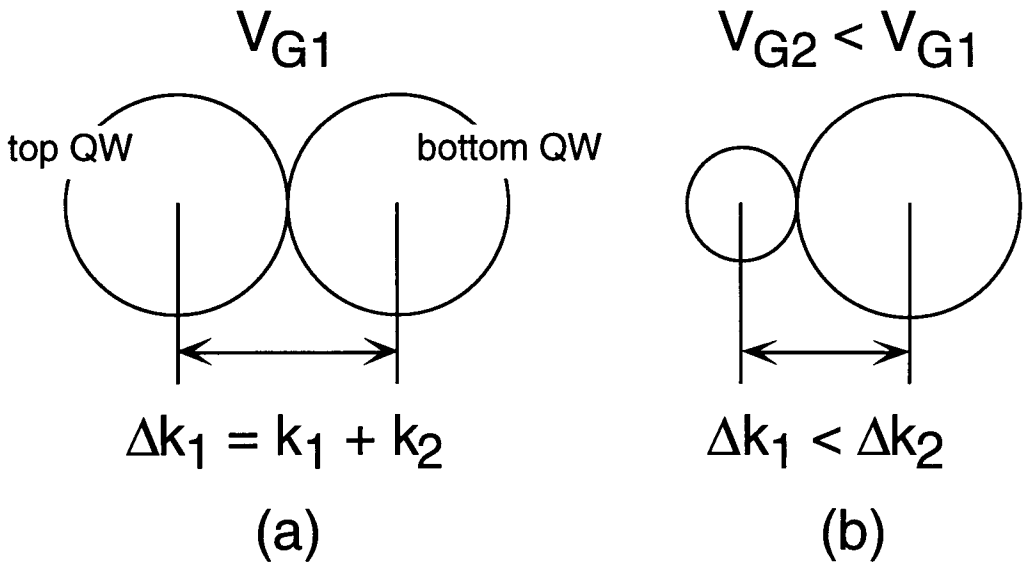

Fig. 4.10 Sketch of the uncoupled Fermi circles at two different V_G showing the Δk necessary to move the middle of the energy gap to the chemical potential.

$$B_{mid} = \left(\sqrt{\frac{C_G}{e}(V_G - V_{depl})} + \sqrt{n_2}\right)\frac{\hbar\sqrt{2\pi}}{ed}, \tag{4.7}$$

where $C_G = \varepsilon/d_c$ is the capacitance per unit area between the gate and top QW. For convenience, a constant permittivity equal to the GaAs permittivity $\varepsilon = 13.1\varepsilon_0$ is used, where ε_0 is the permittivity of free space. d_c is the distance from the gate to the top QW and is the calculated from the samples' growth structures. V_{depl} is obtained from gate scans at $B = 0$ as shown in the inset of Fig. 4.9 and n_2 is obtained from measurements in $B_\perp$ with the top QW depleted. Fits to equation 4.7 using d as the only adjustable parameter are shown in Fig. 4.11. The values for d obtained in this manner show relatively good agreement with values for d obtained from self-consistent Hartree calculations which give d = 195, 140, and 180 Å for samples A, B, and C, respectively.

A similar, somewhat more complicated model is developed for $\Delta B = B_{min} - B_{max}$. B_{max} and B_{min} occur when the top and bottom edges of the energy gap are at μ. At B_{max}, the uncoupled Fermi circles overlap as shown in Fig. 4.12(a) and $\Delta k_{max} = (k_1 - \Delta k_1) +$

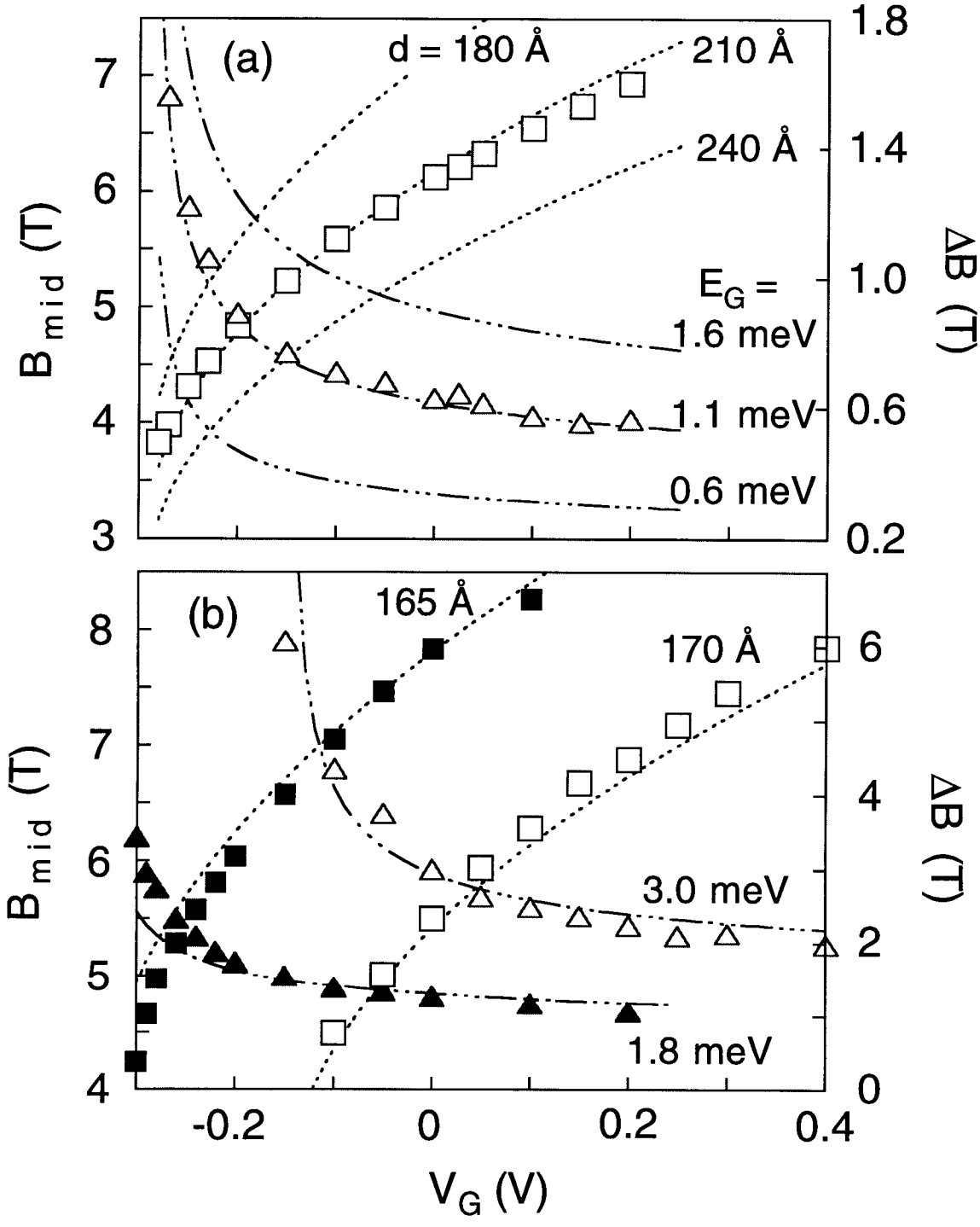

Fig. 4.11 (a) Plot of B_{mid} (squares) and ΔB (triangles) for sample A. Dotted lines are plots of equation 4.7 using different values of the fit parameter d and dash-dotted lines are plots of equation 4.8 for various E_G. (b) Same as in (a), but for samples B (solid symbols) and C (open symbols) showing the best fits.

($k_2 - \Delta k_2$). At B_{min}, they are slightly separated as shown in Fig. 4.12(b) and Δk_{min} = ($k_1 + \Delta k_1$) + ($k_2 + \Delta k_2$). Fig. 4.12(c) shows a schematic of the dispersion curve at the anticrossing and shows the definition of Δk which is obtained from $\Delta E/\Delta k = \partial\varepsilon/\partial k$. $\partial\varepsilon/\partial k$ is the slope of the uncoupled dispersion curve and is evaluated as $\hbar^2 k/m^*$. Using $B_{min,max} = \hbar\Delta k_{min,max}/ed$ and $\Delta B = B_{min} - B_{max}$ we obtain

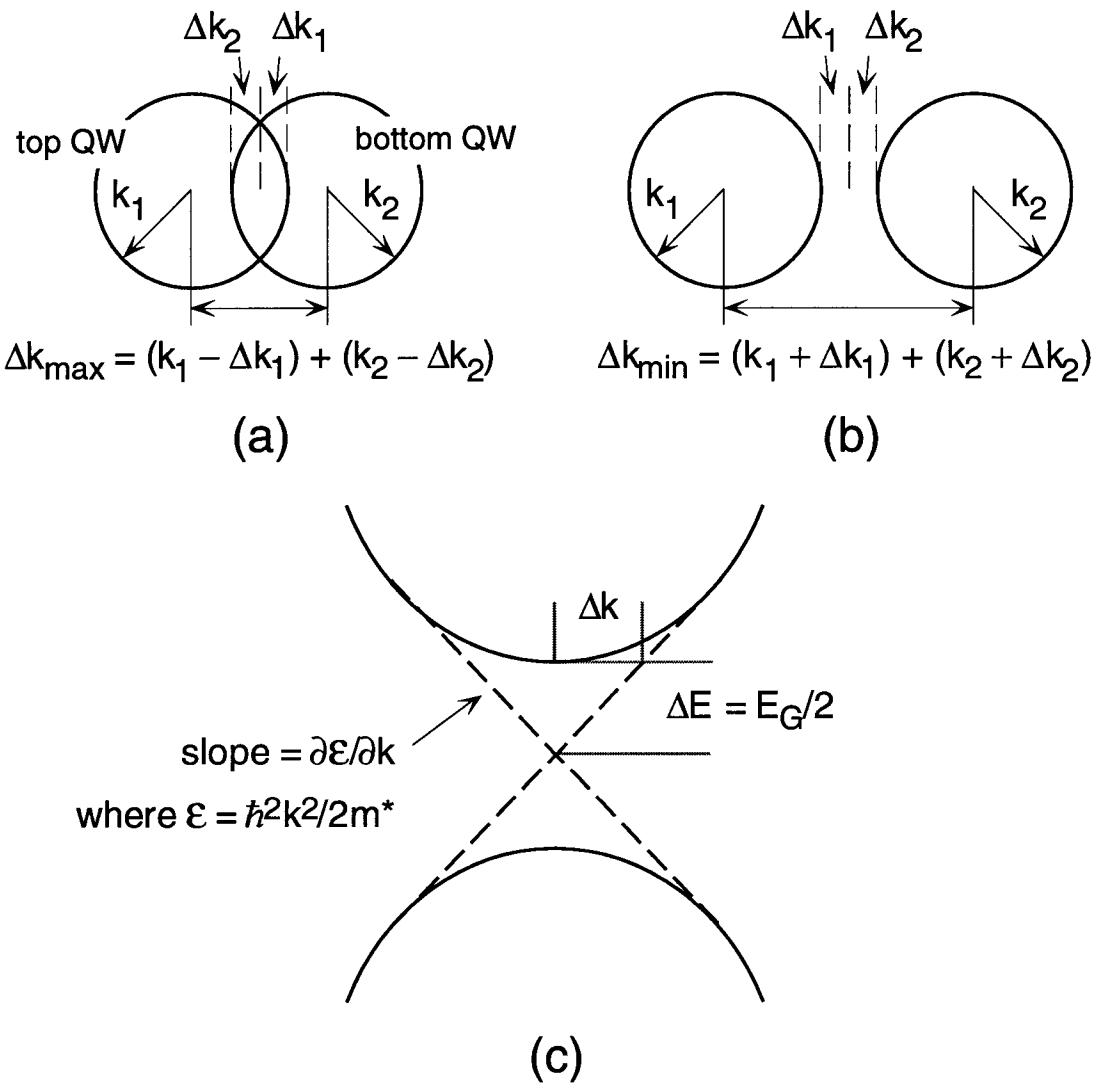

Fig. 4.12 Sketch of the Fermi surfaces and the Δk necessary for (a) the top of the energy gap to be at the chemical potential, (b) the bottom of the energy gap to be at the chemical potential. (c) Sketch of the dispersion curve and the quantities used to calculate ΔB.

$$\Delta B = \left[\left(\frac{C_G}{e}(V_G - V_{depl})\right)^{-1/2} + n_2^{-1/2}\right]\frac{E_G m^*}{ed\hbar\sqrt{2\pi}}. \quad (4.8)$$

Fits to equation 4.8 using values of d obtained from the fit of equation 4.7 and with E_G as the only adjustable parameter are shown as dash-dotted lines in Fig. 4.11. This gives values of E_G = 1.1, 1.8, and 3.0 meV, respectively for samples A, B, and C, which are in fair agreement with the values of E_G = 1.4, 2.0, and 3.4 meV obtained from the Hartree calculations. The assumptions made to obtain equation 4.8 breakdown for larger E_G, as seen by the larger discrepancy for sample C.

4.3 Measurement of Electron Cyclotron Effective Mass

The above experiments showed that the in-plane magnetic field causes changes in the in-plane conductance that are the result of distortions in the density of states due to distortions in the DQW dispersion curve. One would expect to see distortions as a function of $B_{||}$ in other properties that depend on the dispersion curve or Fermi surface. One such quantity is the electron effective mass m^*. In one sense, the effective mass can be viewed as being inversely proportional to the curvature of the dispersion curve. For the lens orbit near the energy gap, a small m^* is expected due to the sharp curvature here (see Fig. 4.2). For both branches far from the energy gap, m^* is expected to be equal to the GaAs effective mass $m^*_{GaAs} = 0.067m_e$. The situation is more complicated at the saddle-point where $\varepsilon(k_x, k_y)$ has negative curvature in the k_y-direction and positive curvature in the k_x-direction. The purpose of the following experiment is to measure m^* as a function of $B_{||}$. The Fermi surface area in **k**-space can also be determined from this experiment and is discussed at the end of this section.

4.3.1 Experiment

The effective mass is measured by adding a small perpendicular ($B_\perp$) component of magnetic field to $B_\parallel$ and analyzing the resulting magnetoresistance oscillations as a function of temperature. With small $B_\perp$ and at lower temperatures, the Landau levels are fairly narrow and the overlap between adjacent Landau levels is relatively small. Therefore, the magnetoresistance oscillations have a large amplitude. For the same $B_\perp$, as the temperature is raised, the Landau levels are thermally broadened, which increases the overlap between adjacent Landau levels and causes the oscillation amplitude to decrease. This thermal broadening is proportional to m^*T [95]. Thus, oscillations from subbands with small m^* persist to higher T than oscillations from subbands with large m^*.

The experiments were done with the sample mounted at a small, fixed angle θ from parallel to the magnetic field, where $\theta = 2.5°$, 3.0°, and 3.5° were used [89, 90]. This gave a large, changing $B_\parallel$ ($= B_T \cos\theta$) and a small, changing $B_\perp$ ($= B_T \sin\theta$). The fact that $B_\perp$ was changing simultaneously with $B_\parallel$ was dealt with in the analysis and had negligible effects on the outcome of the experiment. The sample temperature was held constant during each B_T-sweep and several sweeps were done at temperatures ranging from 0.5 K to 3.0 K. The sample temperature was monitored using a calibrated germanium resistor. Measurements could have been done to obtain a constant $B_\parallel$ and changing $B_\perp$ as described in Chapter 3, however, this method requires hundreds of B_T sweeps for *each* temperature. The total process would take several months. The issue here is not the time required but the stability of the sample. Over the period of several months, the sample density would be likely to change by roughly ±10%, thereby making an accurate determination of m^* impossible. This technique has subsequently been used to measure small mass deviations as a function of $B_\parallel$ in single 2DEGs [96, 97].

Fig. 4.13(b) shows the resulting magneto-resistance oscillations for sample A at θ = 3.0° and $T = 0.5$ K. Due to the simultaneously changing $B_\parallel$ and $B_\perp$, the SdH oscillations

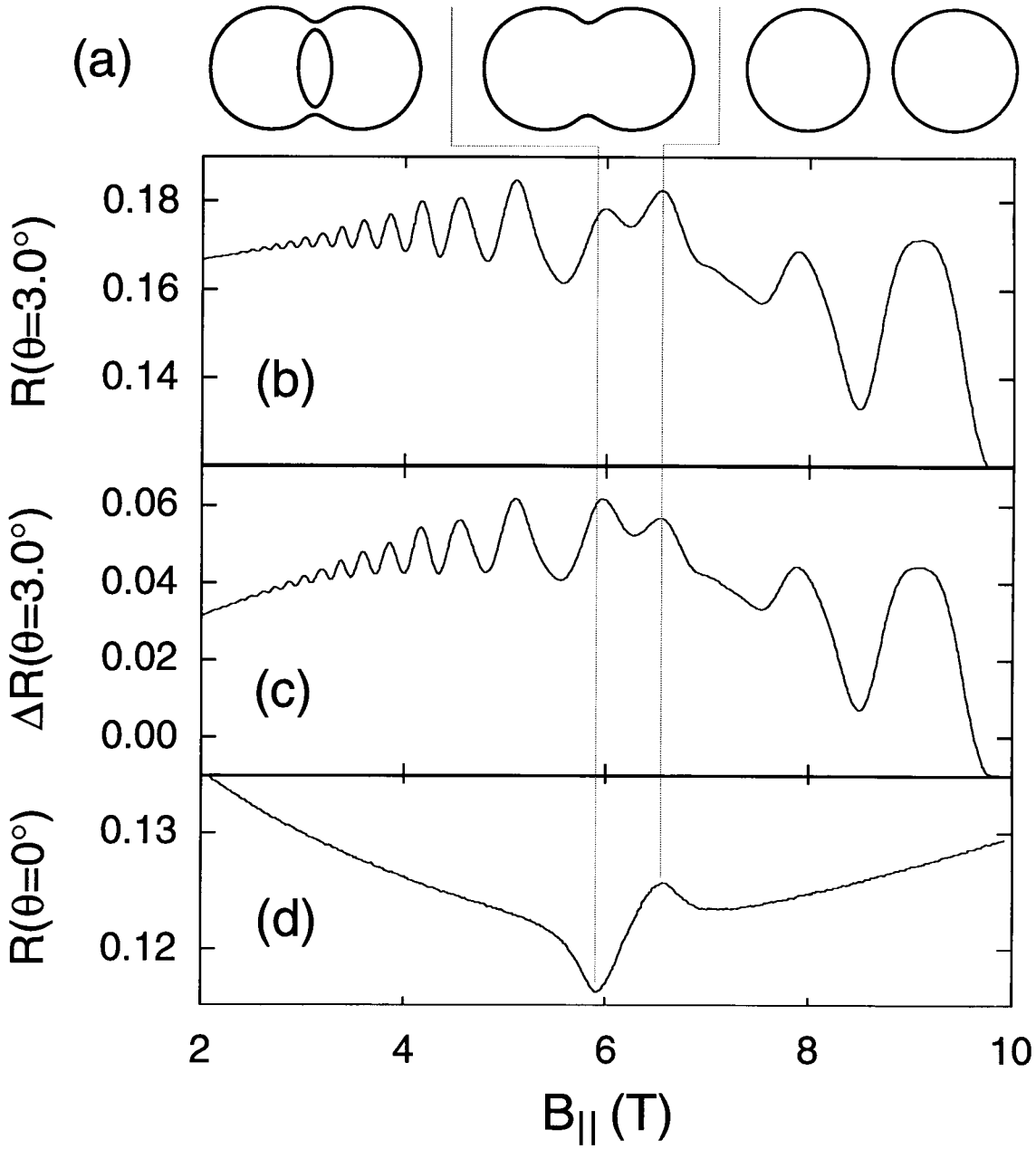

Fig. 4.13 (a) Sketch of the Fermi surfaces for the different $B_{||}$ regions. (b) Magnetoresistance oscillations of sample A at $\theta = 3.0°$ and $T = 0.5$ K, (c) ΔR resulting from (b), (d) anticrossing features for $\theta = 0°$. Curve (d) was subtracted from (b) to get curve (c). The gray lines highlight the anticrossing features.

are mixed with the anticrossing features and to partially remove this mixing, $\Delta R(B_{||}, \theta=3°)$ = $R(B_{||}, \theta=3°) - R(B_{||}, \theta=0°)$ was analyzed. Fig. 4.13(c) and (d) show $\Delta R(B_{||}, \theta)$ and $R(B_{||}, \theta=0°)$, respectively. The main difference between $R(B_{||}, \theta)$ and $\Delta R(B_{||}, \theta)$ occurs near the anticrossing as shown by the gray lines in Fig. 4.13.

The data can be divided into three regions: low, intermediate and high $B_{||}$. Fig. 4.13(a) shows a sketch of the Fermi surface for each of these regions. At low $B_{||}$ ($< \approx 6$ T), the oscillations are uniform and have a single period, indicating that a single Fermi surface orbit is contributing to the oscillations. In this range of $B_{||}$, both the lens and peanut orbits are occupied but because the lens is much smaller than the peanut, it is the one contributing to the oscillations. In the peanut orbit, electrons are unable to traverse the entire orbit without scattering, and therefore the peanut orbit has a negligible contribution to the SdH oscillations. In the intermediate $B_{||}$ region (from $B_{||} \approx 6$ to ≈ 6.5 T), only the peanut orbit is present. At the transition from low to intermediate $B_{||}$, both the amplitude and period of the oscillations change significantly, indicating that the Fermi surface and also m^* are going through drastic changes. The oscillations here are much weaker because the peanut is so large. In the high $B_{||}$ region (above $B_{||} \approx 6.5$ T), the two Fermi circles have separated and the oscillations have a single period even though the Fermi surface has two components. This is because the Fermi circles are roughly the same size.

Fig. 4.14 shows ΔR versus $B_{||}$ for several different temperatures for sample A at θ = 3° [89, 90]. As stated previously, the mass is determined from the temperature dependence of the amplitude of the oscillations. The oscillations the low $B_{||}$ region persist to higher temperatures than the oscillations in other regions, indicating that the thermal broadening of the Landau levels is smaller , and thus m^* is lower in this region. In the anticrossing, there are only a couple of weak oscillations whose amplitudes decrease rapidly with increasing T, indicating a larger m^*. At high $B_{||}$, the dispersion curve is again parabolic and m^* is expected to be equal to m^*_{GaAs}.

The SdH oscillations for a single Fermi surface orbit are described by the Ando formula, which, after converting from conductance to resistance, is [95]

$$\frac{\delta R(T)}{4R_o} = \sum_{s=1}^{\infty} \frac{sX_T}{\sinh(sX_T)} \exp\left[\frac{-\pi s}{\omega_c \tau}\right] \cos\left[\frac{2\pi s\mu}{\hbar\omega_c} - \pi s\right], \tag{4.9}$$

where $\delta R(T)$ is the amplitude of an oscillation, R_o is the resistance at $B_T = 0$, $X_T = 2\pi^2 k_B T/\hbar\omega_c$, $\omega_c = eB_\perp/m_c$, and τ is the total scattering time. The $sX_T/\sinh(sX_T)$ factor accounts for the thermal broadening. The amplitude is calculated from Fig. 4.14 by linearly interpolating between two adjacent minimum to get the resistance minimum at the $B_\perp$ where the oscillation maximum occurs and then subtracting the minimum resistance from the maximum resistance. This can be done for all maxima and it can also be done

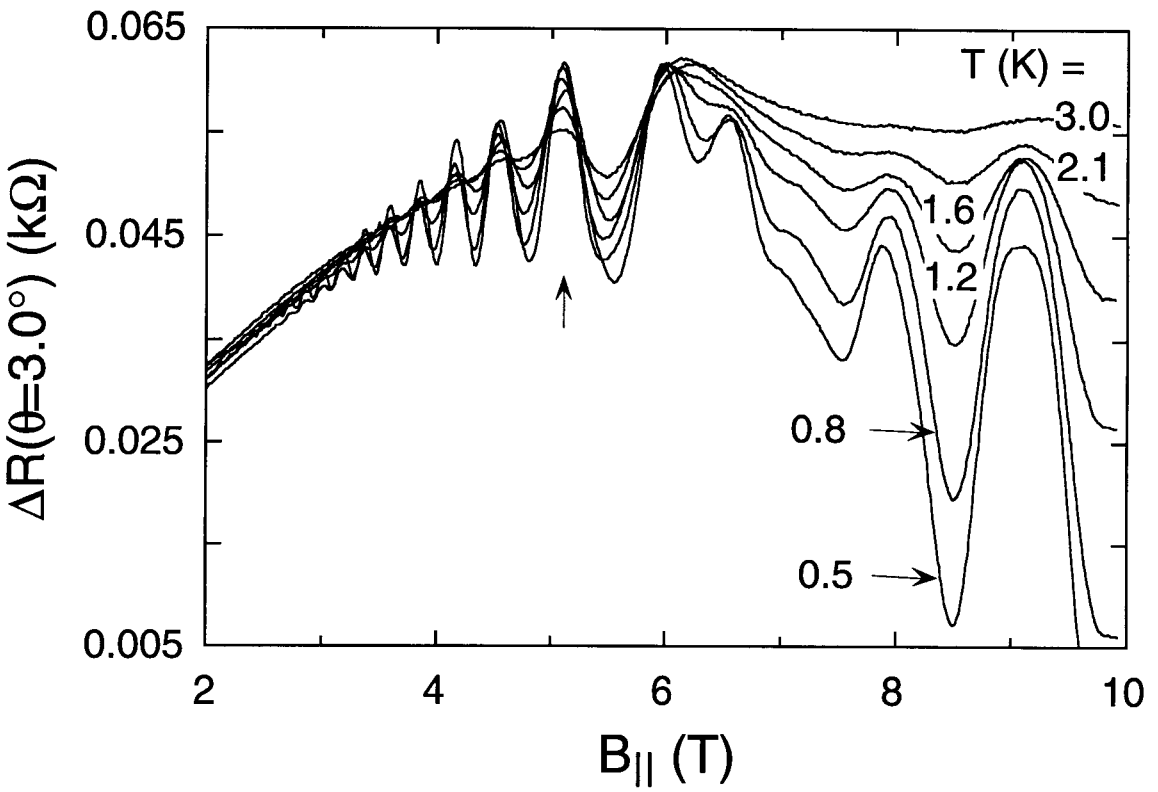

Fig. 4.14 Plot of $\Delta R(B_{||}, \theta = 3.0°)$ for several T. Oscillations below $B_{||} \approx 5.9$ T persist to higher T, indicating a lower m^* in this region. The vertical arrow at 5.1 T indicates one $B_\perp$ at which m^* is calculated.

using two maxima and a minimum. Alternatively, a line can be fit to the maxima and another line fit to the minima and the difference between these two lines can be obtained for the $B_\perp$ of interest. In this way, the mass can be determined quasi-continuously as a function of $B_\parallel$. When $B_\perp$ is sufficiently small that $\omega_c\tau$ is of order unity, the higher order terms ($s > 1$) become negligible, and the SdH oscillations become single period, small in amplitude, and sinusoidal in shape. This clearly describes the data in Fig. 4.14, particularly at low $B_\parallel$. The oscillations in this data are strongly sinusoidal and never exceed 15% of the background.

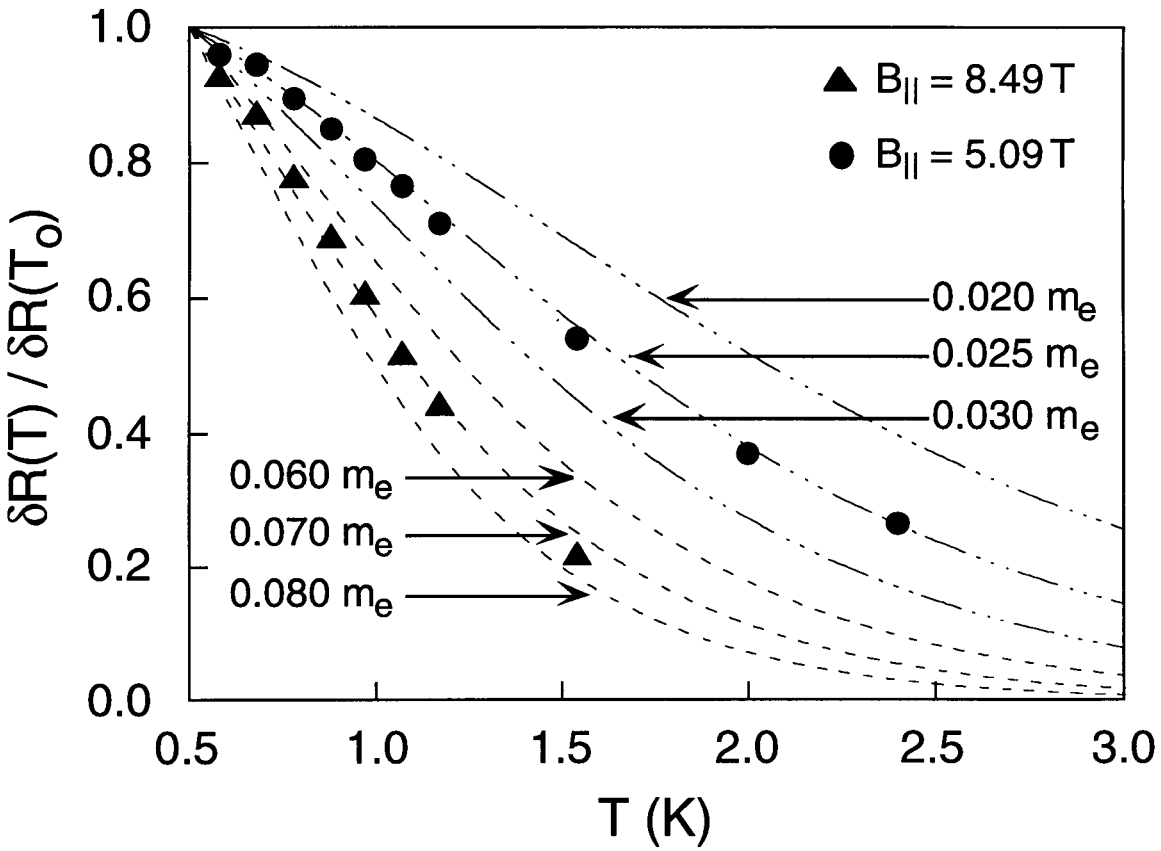

Fig. 4.15 Ratio of oscillation amplitudes versus temperature at $\theta = 3.0°$. Dashed (dash-dotted) lines show fits of equation 4.10 to $B_\parallel$ = 8.49 T (5.09 T) data for several mass values, with the best fits giving $m^* = 0.070\ m_e$ (0.025 m_e).

When higher-order terms are negligible, equation 4.9 can be simplified. The ratio of the oscillation amplitude at temperature T to the amplitude at base temperature T_o is then given by [19]

$$\frac{\delta R(T)}{\delta R(T_o)} = \frac{T\sinh\left(\beta T_o(m^*/m_e)/B_\perp\right)}{T_o\sinh\left(\beta T(m^*/m_e)/B_\perp\right)}, \tag{4.10}$$

where $\beta = 2\pi^2 k_B m^*/\hbar e$. When the ratio of amplitudes at a given $B_\perp$ is plotted versus temperature, m^* is used as a fit parameter in the expression above. Two typical fits to equation 4.10 are shown in Fig. 4.15 [89, 90]. The quality of the fits is quite good and provides further justification for using this method to determine m^* and also for neglecting the higher order terms in equation 4.9. The mass obtained for $B_{||}$ = 8.49 T is 0.070 m_e which is very close to m^*_{GaAs}, as expected. However, m^* at $B_{||}$ = 5.09 T is 0.025 m_e which is roughly a factor of three lower than m^*_{GaAs}. The fits yield an error of roughly 10%, except for the range $\approx$ 5.9 T < $B_{||}$ < $\approx$ 6.5 T, where the mass changes substantially between adjacent SdH extrema, yielding errors of roughly 20%.

A summary of the measured m^* versus $B_{||}$ for all three angles used [89, 90] is shown in Fig. 4.16 along with a theoretical calculation of m^* [91]. Below $B_{||} \approx$ 2.7 T, the oscillations at higher T were too weak to accurately determine m^*. Near $B_{||}$ = 2.7 T, $m^* \approx$ 0.5 m_e, which is considerably lower than m^*_{GaAs}. As $B_{||}$ is increased, the size of the lens and its mass decrease, reaching $m^* \approx$ 0.021 m_e when the lens disappears at $B_{||} \approx$ 5.9 T. After this point, the mass increases rapidly to $m^* \approx$ 0.099 m_e approximately when the saddle-point crosses the chemical potential. As stated previously, the error in the measured mass in the anticrossing region is quite high. However, the measured mass here is significantly larger than m^*_{GaAs}. As $B_{||}$ is further increased, m^* drops and rapidly converges to m^*_{GaAs} near $B_{||} \approx$ 7 T and remains approximately constant after that, as expected.

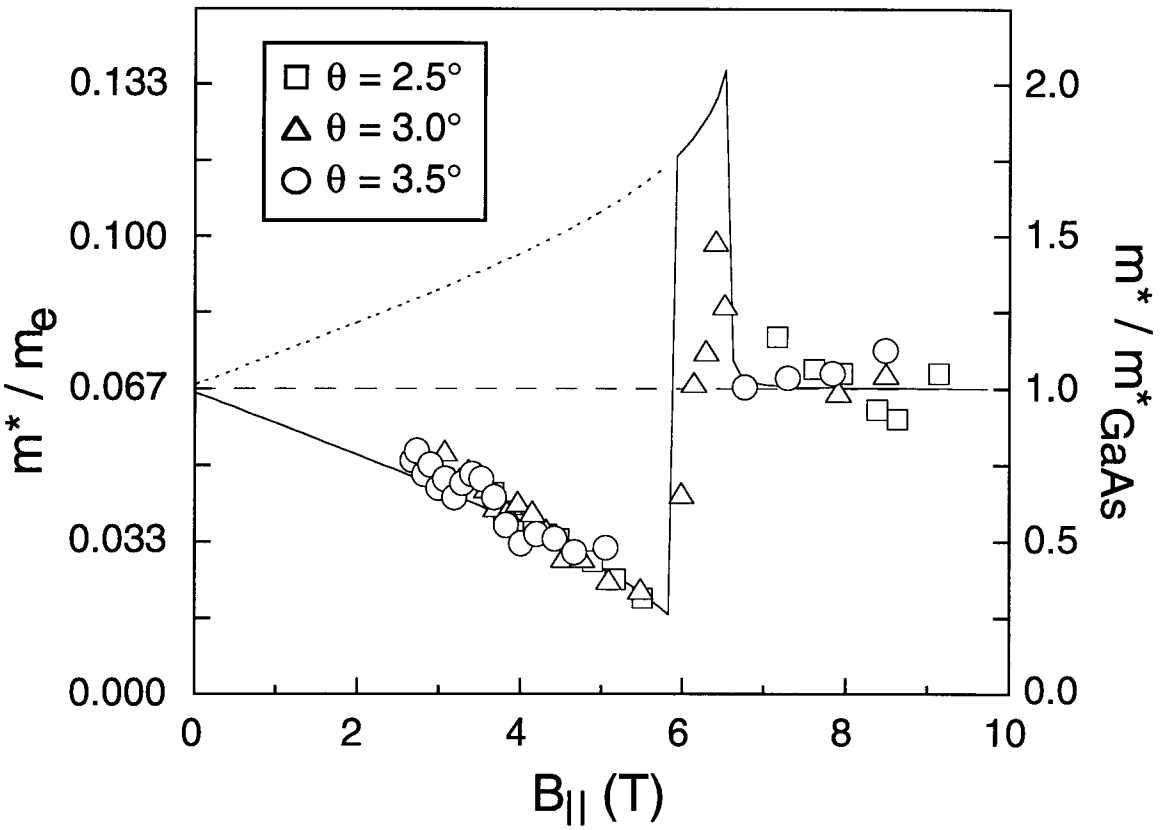

Fig. 4.16 Summary of measured m^* versus $B_{||}$ for all three angles θ used. The solid line is the theoretical calculation of m^* for the dominant Fermi surface orbit and the dotted line is the peanut m^* where it is not the dominant orbit.

4.3.2 Comparison with Calculated Effective Mass

Theoretically, the mass for each Fermi surface orbit is given by $m^* = (\hbar^2/2\pi)\partial S/\partial\varepsilon$, where S is the area of the orbit in **k**-space, and ε is the electron energy at the Fermi surface [91]. The **k**-space area of each orbit as a function of energy is obtained from the dispersion curve calculated using the tight-binding method earlier in this chapter. This expression can be rewritten as $m^* = m^*_{GaAs}\rho(\varepsilon)/\rho_0$ for 2D structures, where $\rho(\varepsilon)$ is the contribution to the DOS per spin from the orbit under consideration, $\rho_0 = m^*A/(2\pi\hbar^2)$ is the DOS per spin of a 2D parabolic dispersion curve, and A is the area of the QWs. This equation shows that the effective mass is directly related to the DOS.

The results of this calculation for sample A are shown as the solid line in Fig. 4.16. For $B_{||} \approx 0$ T, both the lens and peanut orbits have $m^* \approx m^*_{GaAs}$ because the dispersion curve is not distorted at such low $B_{||}$. As $B_{||}$ increases, the lens mass decreases and the peanut mass increases. For $B_{||} < \approx 6$ T, the lens dominates and there is excellent agreement between the calculation and the experimental data. When μ is in the energy gap ($\approx 6.0 < B_{||} < \approx 6.5$ T), only the peanut orbit is occupied. However, an accurate measurement of the peanut m^* was not possible with this sample because there are only a couple of weak oscillations in this $B_{||}$ range. After the two Fermi circles have separated ($B_{||} > \approx 6.5$ T), both the theoretical and measured effective masses return to m^*_{GaAs}.

4.3.3 Peanut Orbit Mass Measurement

To accurately measure the peanut effective mass, the mass measurements were repeated on sample D, which has a Δ_{SAS} large enough that the lens orbit is not occupied at any $B_{||}$ and only the peanut orbit is occupied for a large range of $B_{||}$ [98].. This means that there are many SdH oscillations from which to accurately measure m^* for the peanut orbit. This sample has $w = 125$ Å and $t = 10$Å, which results in a calculated $\Delta_{SAS} \approx 7.6$ meV. Δ_{SAS} for this sample could not be measured because the antisymmetric state is not occupied at $B_{||} = 0$ due to the large Δ_{SAS}. Above $B_{||} \approx 12$ T, the energy gap moves above the chemical potential and the Fermi surface then consists of two uncoupled circular orbits.

Fig. 4.17(a) shows the magnetoresistance of sample D at an angle $\theta = 0°$ at base temperature. The broad maximum near $B_{||} = 12$ T occurs when the saddle-point reaches the chemical potential. However, there is no resistance minimum indicating the lens orbit moving above the chemical potential. This shows that the lens is not occupied at any $B_{||}$ and only the peanut orbit is present for $B_{||} < \approx 12$ T. Fig. 4.17(b) shows ΔR of this sample at an angle $\theta = 10°$ for several different temperatures. These oscillations are uniform and have a single period, indicating that a single Fermi surface orbit is contributing

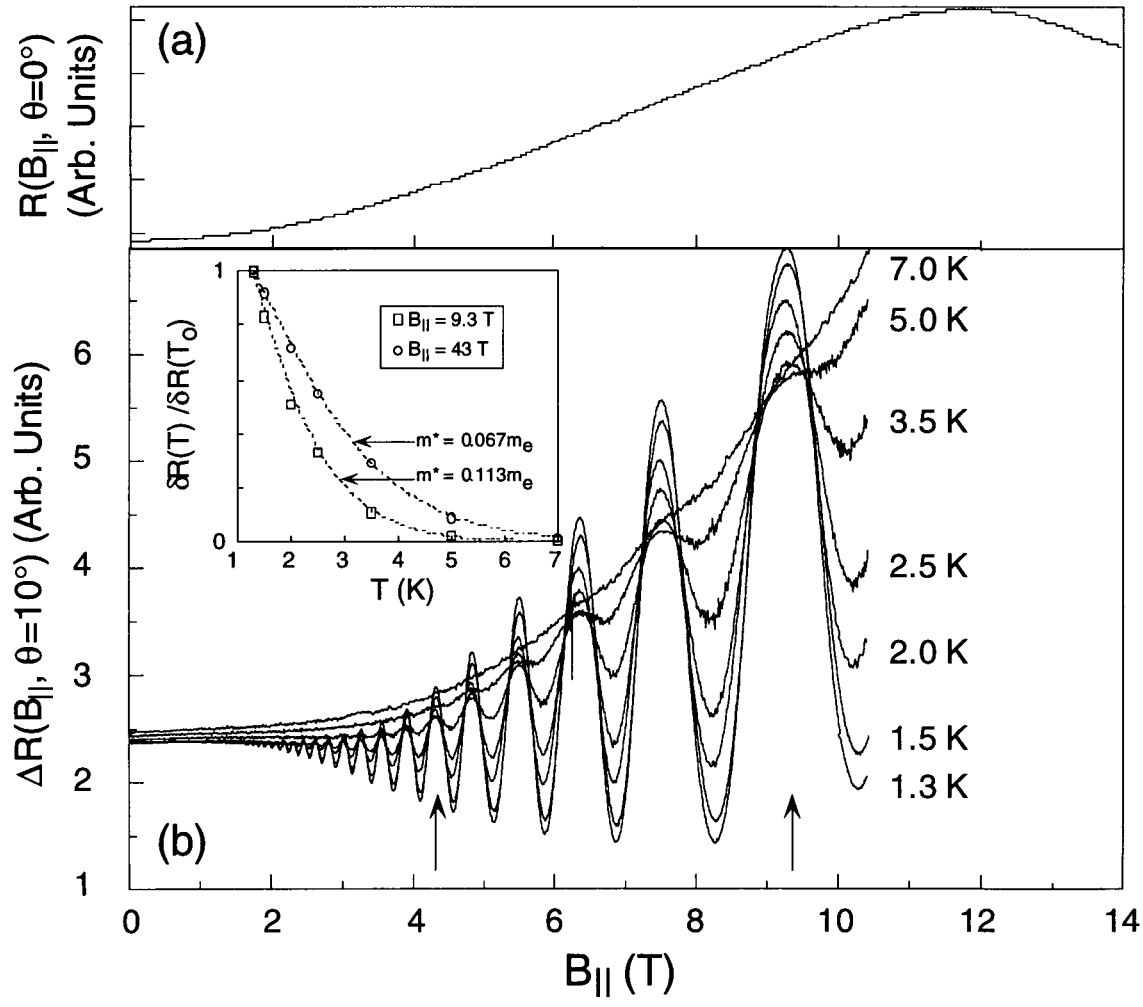

Fig. 4.17 Plot of (a) $R(B_{||}, \theta = 0°)$ and (b) $\Delta R(B_{||}, \theta = 10°)$ versus $B_{||}$ for sample D at several T. In (b), the vertical arrows at 4.3 and 9.3 T indicate the $B_{\perp}$ at which m^* is calculated. Inset: Ratio of oscillation amplitudes versus temperature for the two values of $B_{\perp}$ indicated.

to the oscillations. The inset to Fig. 4.17(b) shows fits to equation 4.10 at $B_{||} \approx 4.3$ T and ≈ 9.3 T. The fits to this data are also of very good quality and result in $m^* \approx 0.067\ m_e$ and $0.113\ m_e$, respectively.

A summary of m^* versus $B_{||}$ for sample D is shown in Fig. 4.18. Below $B_{||} = 2$ T, the oscillations were too weak to determine m^*. For $2\text{ T} < B_{||} < \approx 4.5$ T, $m^* \approx m^*_{GaAs}$. It

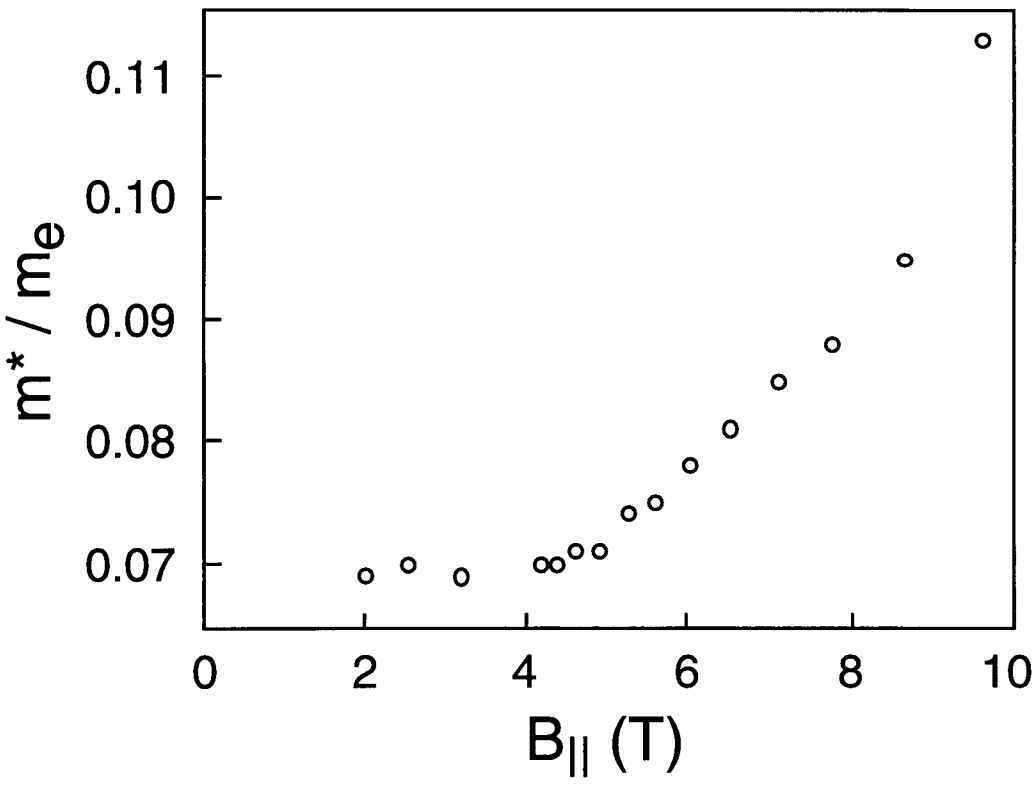

Fig. 4.18 Measured m^* versus $B_{||}$ for the peanut orbit of sample D.

is difficult to determine why the mass is unchanged in this region. This may be due to a small value of d ($\approx$ 125 Å + 10 Å), which then requires a larger value of $B_{||}$ to distort the Fermi surface. In the range 4.0 T < $B_{||}$ < 11.9 T, m^* increases dramatically and monotonically, reaching $\approx 0.11\ m_e$ at $B_{||} \approx$ 10 T. Mass measurements could not be done for $B_{||}$ > 12 T, where the two circles have separated and the mass returns to m^*_{GaAs}, because the magnet could not reach the high magnetic fields required. A theoretical calculation of the effective mass for this sample has not been done, however, the measured peanut mass shows the monotonic increase seen in the calculated peanut mass of sample A. Due to these similarities, good agreement between the theoretical and experimental data is expected.

4.3.4 Fermi Surface Area

Finally, it is possible to determine the dominant orbit's **k**-space area from the period of the magneto-resistance oscillations [27], The area in **k**-space is given by $A = (2\pi e/\hbar)[\Delta(1/B_\perp)]^{-1}$ and $\Delta(1/B_\perp)$ is the oscillation period, which is the spacing between resistance peaks in $1/B_\perp$. The inverse of the period is plotted as a function of $B_\parallel$ in Fig. 4.19 for sample A. The conversion to **k**-space area is shown on the right vertical axis of the figure. As $B_\parallel$ is raised, the data shows that the area of the lens orbit decreases, as expected. There are not enough oscillations when μ is in the energy gap (5.9 T < $B_\parallel$ < 6.5 T) to determine the orbit area. For $B_\parallel$ > 6.5 T, the area is clearly much larger than the lens

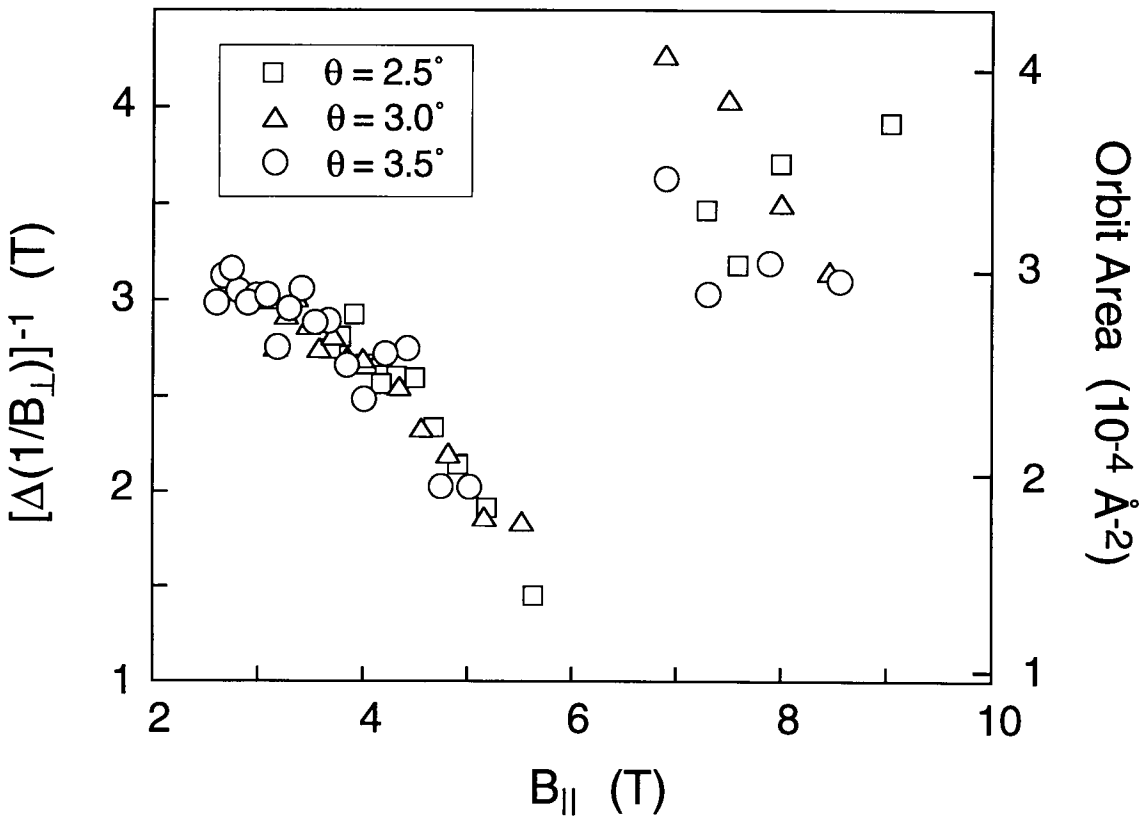

Fig. 4.19 Plot of the inverse of the peak spacings in $1/B_\perp$ as a function of $B_\parallel$ for the three angles used for sample A. $[\Delta(1/B_\perp)]^{-1}$ is proportional to the orbit area in **k**-space which is shown on the right vertical axis.

area and appears to be constant within ±20% error. There is considerable scatter in this range because the DQW was not fully in-balance and therefore, the two circle orbits have slightly different areas.

4.4 Chapter Summary

This chapter examined the effect of dispersion curve distortions on transport in double quantum well samples. The chapter started with a description of the dispersion curve distortions that result from an in-plane magnetic field. Next, calculations of the in-plane conductance were presented. This work was done by Ken Lyo and was published in reference [31]. After that, measurements of the conductance as a function of in-plane field were described. Two features were observed in the conductance and, after a slight modification to his theory, Lyo was able to reproduce these features theoretically. Using the gate bias dependence of these features, Δ_{SAS} could be extracted from this data. The experimental results were published in reference [88]. The last part of the chapter describes the experimental measurement and theoretical calculation of the electron cyclotron effective mass as a function of in-plane field. The mass was measured by analyzing the temperature dependence of the magnetoresistance oscillations when a perpendicular magnetic field was also applied to the sample. A mass as low as 1/3 the GaAs effective mass was measured. There was excellent agreement between the measured and calculated masses. These were the first mass measurements done on this distorted dispersion curve and the results were published in references [86, 89, 90]. The calculations were done by Ken Lyo and these results were published in reference [91].

5. DOUBLE QUANTUM WELLS IN TILTED MAGNETIC FIELDS

In this chapter, DQWs subject to tilted magnetic fields are studied. The only previous work on DQWs subject to large tilted magnetic fields studied the $\nu = 1$ quantum Hall state at different tilt angle [46]. This work investigated many-body Coulomb interactions between electrons in different layers. The present work focuses on the magnetoresistance at slightly lower $B_\perp$, where $\nu \approx 4 - 14$. This work, for the first time, investigates the evolution of Landau levels as the Fermi surface is controllably changed. Magnetic breakdown, which is tunneling through **k**-space from one Fermi surface orbit to another, is also studied in this experiment. The in-plane field again distorts the dispersion curve; while the perpendicular magnetic field causes Landau level formation and magnetoresistance oscillations for each branch of the Fermi surface. First the experimental results are presented and discussed in terms of the shifted Fermi circles. Then it will be shown that magnetic breakdown is occurring in the DQW samples studied. Next, a semiclassical calculation of the Landau level positions is performed to help explain the data, and finally, the Fourier power spectra of the data will be presented and also explained in terms of the shifted Fermi circles.

5.1 Magnetoresistance Versus $B_{||}$ and $B_\perp$

The magnetoresistances of samples E and F and the Hall resistance of sample E were measured as a function of $B_{||}$ and $B_\perp$ [99, 100] using the multiple scan technique described in Section 3.2.2. For this experiment, approximately nine hundred B_T sweeps were done at different angles over the course of six weeks. This resulted in data in the ranges 0.0 T < $B_{||}$ < 9.25 T and 0.0 T < $B_\perp$ < 5.5 T, however, analysis of the data for $B_\perp$ < 1.5 T will be emphasized. Fig. 5.1 shows a schematic representation of the B_T sweeps as a function of

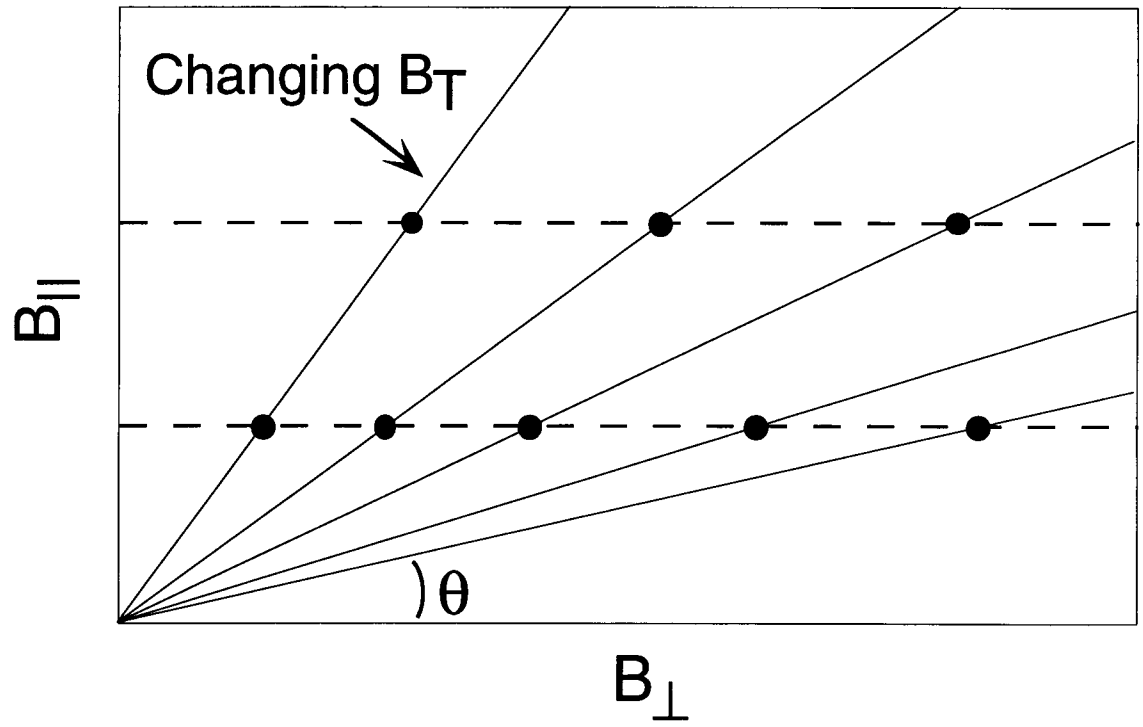

Fig. 5.1 Schematic representation of the B_T sweeps with the sample mounted at different angles θ. The solid lines represent resistance data as a function of $B_{||}$ and $B_\perp$ for each B_T sweep. The dashed lines are slices where resistance versus $B_\perp$ traces at constant $B_{||}$ are extracted.

$B_{||}$ and $B_\perp$ for several B_T sweeps with the sample mounted at different angles θ. The solid lines represent resistance data obtained in each B_T sweep. The dashed lines show slices at constant $B_{||}$ where values of resistance and $B_\perp$ are obtained for each scan and then compiled to form a trace of resistance versus $B_\perp$ at a constant value of $B_{||}$. Traces of resistance versus $B_{||}$ with constant $B_\perp$ can also be extracted.

Fig. 5.2(a) shows one of these slices, where R_{xx} and R_{xy} versus $B_\perp$ at a constant $B_{||}$ = 4.5 T for sample E was extracted from the raw data. This $B_{||}$ is large enough to cause the lens and peanut orbits to form. SdH oscillations, with beating present, are clearly seen in the data. The Fermi surface orbits causing these oscillations can be identified by the frequencies of the oscillations in $1/B_\perp$. The frequency is proportional to the **k**-space area

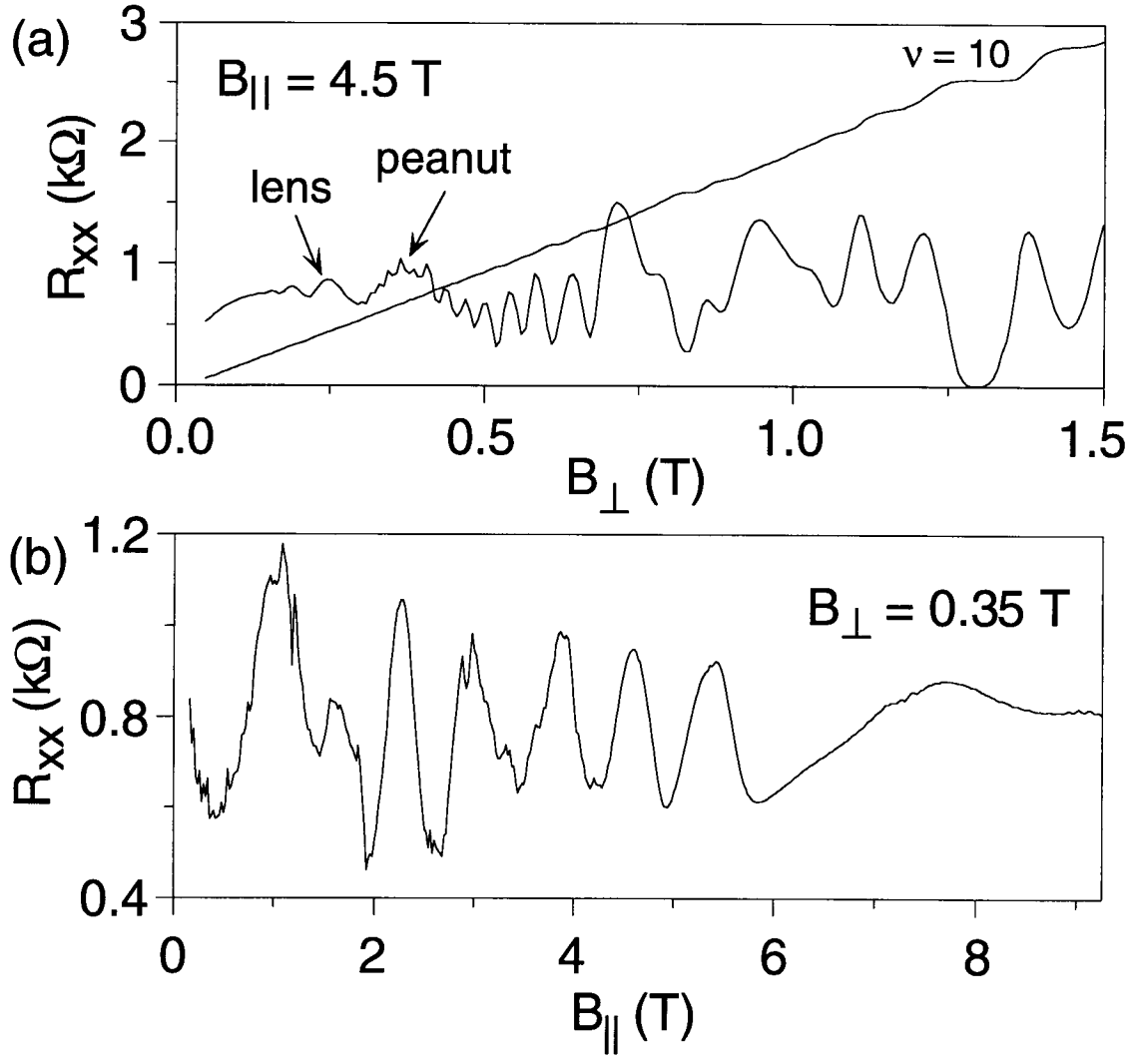

Fig. 5.2 (a) R_{xx} and R_{xy} versus $B_\perp$ at constant $B_{||}$ = 4.5 T for sample E. Oscillations from the lens and peanut orbits can be identified at low $B_\perp$. (b) R_{xx} versus $B_{||}$ at constant $B_\perp$ = 0.35 T for sample E. The large oscillations result as Landau levels in the lens orbit are depopulated with increasing $B_{||}$.

of the Fermi surface component. Therefore, orbits of different sizes can be distinguished from one another.

At low $B_\perp$ ($< \approx 0.3$ T), low frequency oscillations from the lens orbit are visible. As $B_\perp$ increases, small, high frequency oscillations from the peanut orbit are seen superimposed on the lens oscillations. The peanut oscillations are weak because the peanut orbit is large and only a few electrons traverse the entire orbit before scattering. At even

higher $B_\perp$, the data exhibits significant beating and the orbits contributing to the oscillations can not be determined visually. At high $B_\perp$, plateaus can be seen in R_{xy} corresponding to the minima in R_{xx}. The broadest plateau occurs for $\nu = 10$. In Fig. 5.2(b), R_{xx} is plotted versus $B_\parallel$ at a constant $B_\perp = 0.35$ T for sample E. As $B_\parallel$ increases, the lens orbit becomes smaller and the Landau levels in the lens depopulate. As this happens successive Landau levels from the lens cross μ resulting in maxima in R_{xx}. The peanut orbit becomes larger and more populated with increasing $B_\parallel$ resulting in small, high frequency oscillations that occur as more Landau levels in the peanut orbit become occupied. Due to its size, the peanut oscillations are weak and can be seen superimposed on the lens oscillations.

A more complete picture of the evolution of the Landau levels with $B_\parallel$ and $B_\perp$ is possible by plotting the data on contour plots. Fig. 5.3 shows gray-scale plots of R_{xx} versus $B_\parallel$ and $B_\perp$ for sample E (Fig. 5.3(a)) and sample F (Fig. 5.3(b)). The lines are the results of a semiclassical calculation of the $B_\parallel$, $B_\perp$ positions of the Landau levels, which will be discussed later. The numbers in part (b) label Landau levels $N_\ell = 0$ and 1 in the lens, and $N_p = 4$, 5, and 6 in the peanut. The measurements were done in two sets; $B_\parallel <$ 4.0 T and $B_\parallel >$ 4.0 T. A slight discontinuity in the data can be seen at $B_\parallel = 4.0$ T. The discontinuity shows that the sample changed slightly during the measurements but the quality of the data else where shows that the sample was stable through the majority of the measurements. The data in Fig 5.3 can be divided into three distinct $B_\parallel$-regimes: low, intermediate and high $B_\parallel$. The dispersion curve and Fermi surface for each of these $B_\parallel$ regimes are sketched in Fig. 5.4. For sample E, the data span all three regimes: high $B_\parallel$ (> 7.5 T), intermediate (6.0 T < $B_\parallel$ < 7.5 T), and low $B_\parallel$ (< 6.0 T). For sample E, only the low $B_\parallel$ (< 9.0 T) and part of the intermediate $B_\parallel$ (> 9.0 T) regimes are present, due to the higher electron density in this sample .

The high $B_\parallel$ regime occurs when μ is below the energy gap and the two QW Fermi circles have separated (Fig. 5.4(c)). Here, the measured R_{xx} is relatively independent of $B_\parallel$ (Fig. 5.3), resulting in a set of vertical high resistance ridges that occur when Landau levels

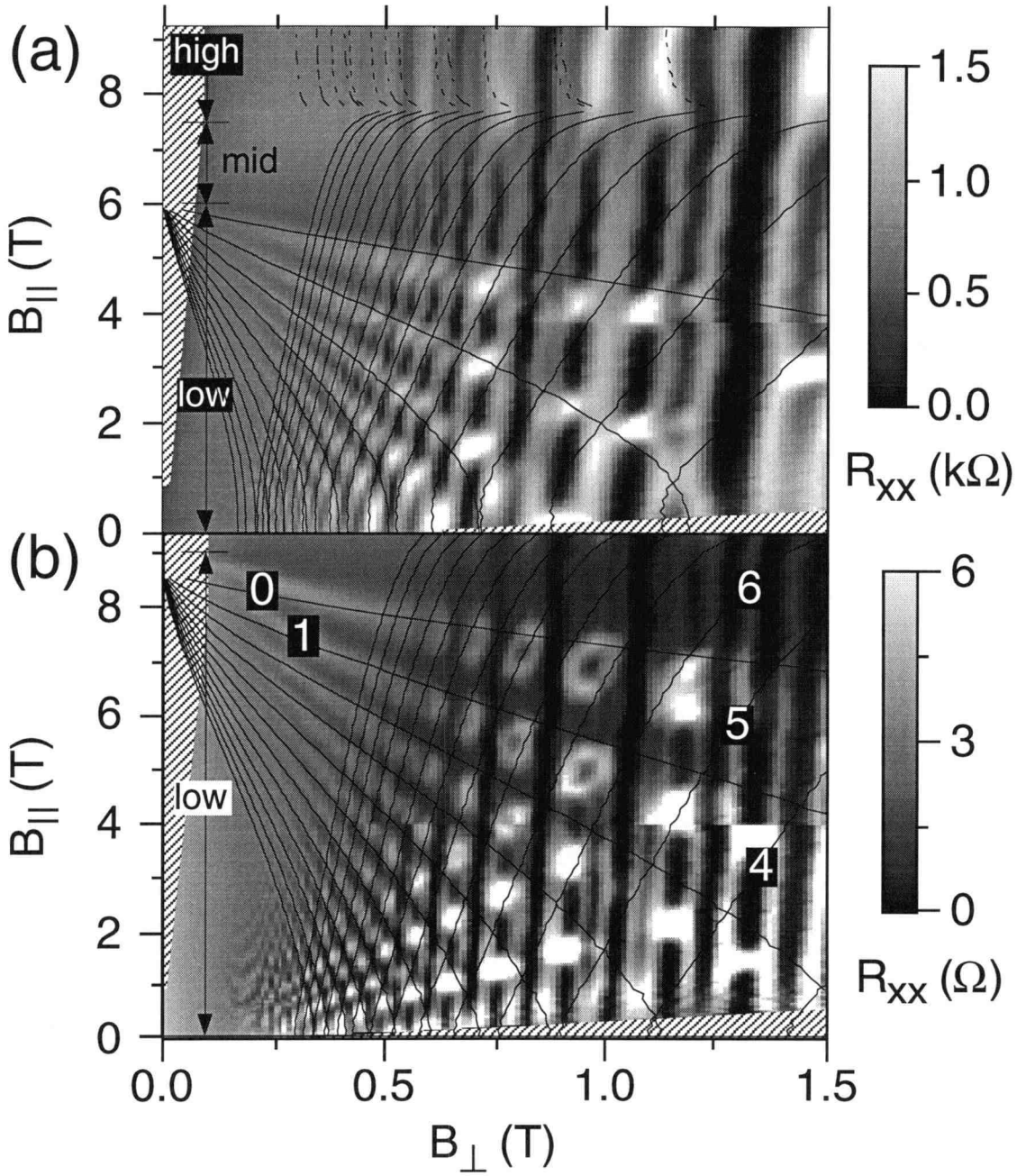

Fig. 5.3 (a) and (b) show R_{xx} versus $B_{||}$ and $B_\perp$ for samples E and F, respectively. The cross-hatching indicates regions where data was not obtained. The $B_{||}$ regimes are shown on the left. The lines show the results of a calculation discussed below and the numbers show the Landau level indices of several lines.

from the circle orbits cross μ. The ridges are vertical because changing $B_{||}$ only changes the separation between the two Fermi circles but does not change the shape of the Fermi surface. There is some beating in the oscillations because the DQW is slightly out of balance and the two circles have different areas, thus they produce oscillations with slightly

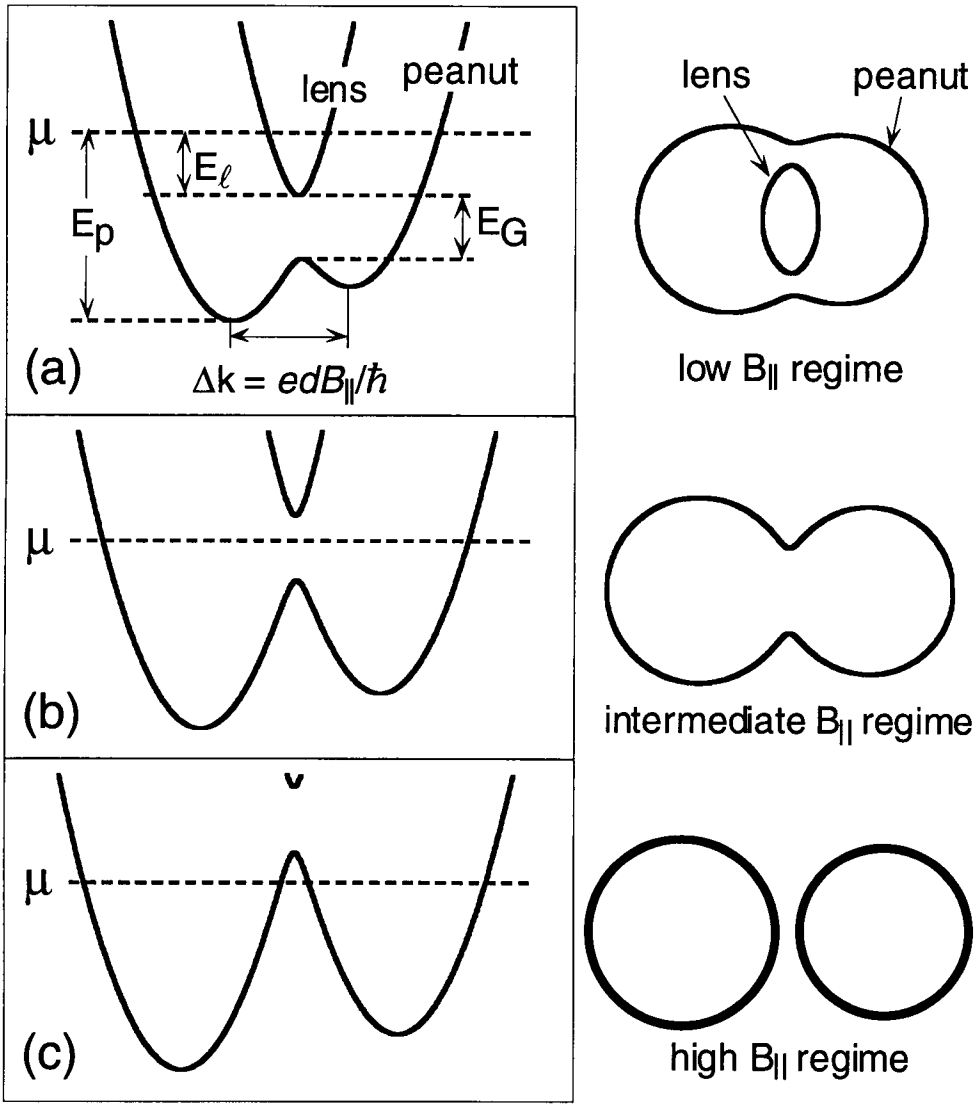

Fig. 5.4 Sketches of the dispersion curves and Fermi surfaces for the three $B_{||}$ regimes. The upper panel contains definitions of the relevant energies.

different frequencies. In the intermediate $B_{||}$ regime, μ is in the energy gap and only the peanut orbit is present (Fig. 5.4(b)). The data here (Fig. 5.3) consist of a set of vertical ridges with several wiggles in it. The main part of the ridges is the result of magnetic breakdown in which electrons tunnel through **k**-space across the neck of the peanut and remain on the QW circle orbits. Magnetic breakdown will be discussed in more detail below. The circle orbits are smaller than the peanut orbit and thus produce stronger oscillations. The wiggles on the ridges result when Landau levels from the peanut coincide with Landau levels from the circle orbits.

The oscillations in the low-$B_{||}$ regime show much more complex beating and depend strongly on $B_{||}$ (Fig. 5.3). In this regime, μ is above the energy gap and both the lens and peanut orbits are occupied (Fig. 5.4(a)). A set of high resistance ridges can be seen running from the upper left to the lower right in both parts of Fig. 5.3. These ridges are due to the Landau levels from the lens orbit coinciding with μ and are seen as the large oscillations in Fig. 5.2. The depopulation of the lens Landau levels with increasing $B_{||}$ is due to two effects. First, the lens Fermi energy (E_ℓ) decreases with increasing $B_{||}$ roughly as the square of $B_{||}$ [31], where E_ℓ is shown in Fig. 5.4(a). Second, the energy spacing ($\Delta E_\ell = e\hbar B_\perp / m^*_\ell$) between the lens Landau levels also increases due to the decrease in the lens effective mass (m^*_ℓ) arising from the distorted dispersion [89 – 91].

A second weaker set of high resistance ridges can also be seen in Fig. 5.3, running from the lower left to the upper right. These ridges are clearly seen in part (a) but are difficult to see in part (b). This set of ridges is due to the peanut orbit Landau levels crossing μ. These are much weaker because the peanut is so large that relatively few electrons can complete it without scattering. These ridges are the small oscillations seen in Fig. 5.2. While the peanut Fermi energy (E_p) (see Fig. 5.4(a)) remains nearly constant with $B_{||}$, the peanut Landau level spacing ($\Delta E_p = e\hbar B_\perp / m^*_p$) decreases due to an increasing effective mass (m^*_p), thus causing more peanut Landau levels to become occupied.

Sharp peaks in the resistance occur when Landau levels from the lens and peanut orbits cross at μ. In the data of sample F, a series of peaks forming lines running from the lower left to the upper right with a smaller slope than the peanut Landau levels can be clearly seen. These peaks are the intersection points of the lens and peanut Landau levels, as is shown by the semiclassical calculation which will be discussed later. The alternating strength of these rows of peaks is due to a beating of the oscillations from the lens and peanut orbits with oscillations from circular orbits that result from magnetic breakdown, which is discussed below.

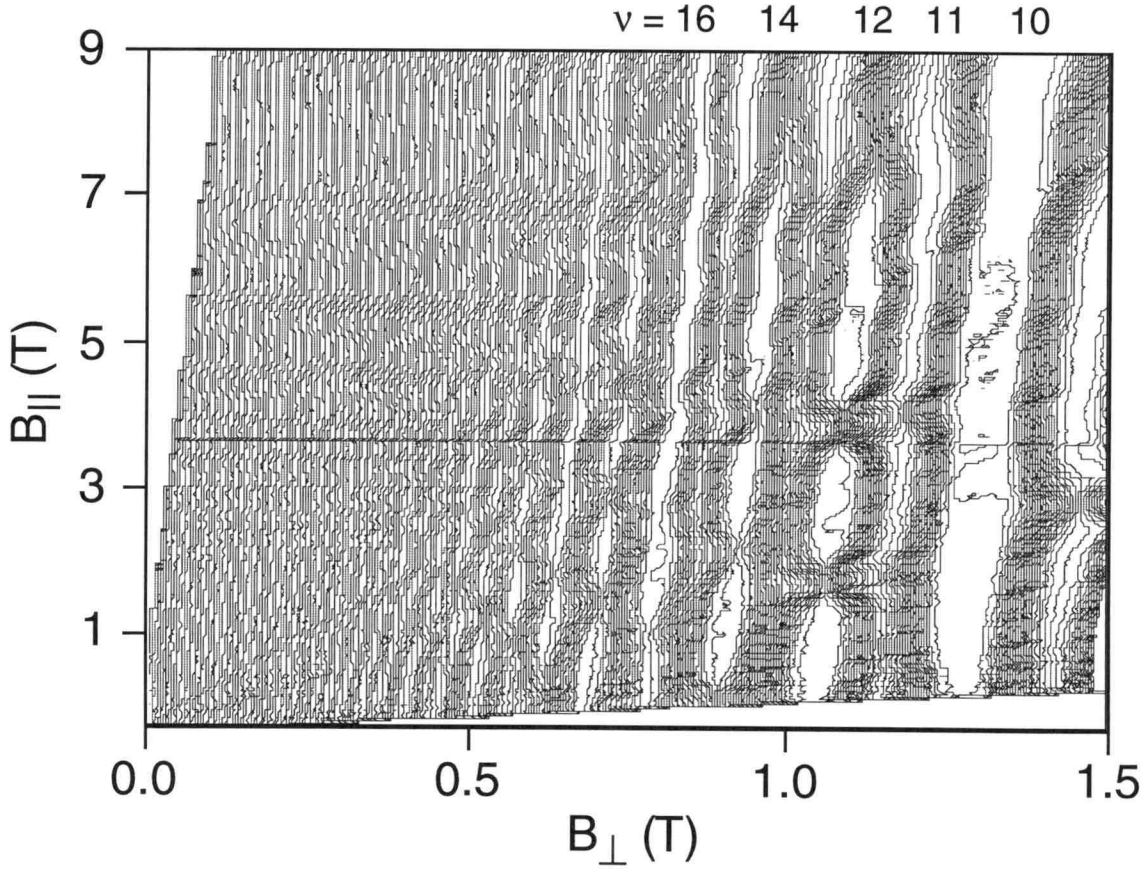

Fig. 5.5 R_{xy} versus $B_{\|}$ and $B_{\perp}$ for sample E. Plateaus appear as white regions and dark regions are rapidly changing R_{xy}. Several filling factors, determined from R_{xy} are shown at the top of the plot.

The Hall resistance of sample E is plotted on a contour plot as a function of $B_{||}$ and $B_{\perp}$ in Fig. 5.5. Plateaus in R_{xy} appear as white regions in the plot and correspond to minima in R_{xx}. The $\nu = 10$ and 16 plateaus are nearly independent of $B_{||}$, indicating that these result from magnetic breakdown. Other plateaus show beating as a function of $B_{||}$, which result from crossings of the lens and peanut Landau levels.

5.2 Magnetic Breakdown

A third set of ridges and valleys, running vertically, can be seen in Fig. 5.3 at slightly higher $B_{\perp}$. These features appear in sample F at lower $B_{\perp}$ than in sample E. This set of ridges is caused by magnetic breakdown [101], in which electrons tunnel through **k**-space between the lens and peanut orbits to form circular orbits corresponding to the individual QWs. The magnetic breakdown is weak at low $B_{\perp}$, but becomes stronger as $B_{\perp}$ is increased, as expected. This increase in breakdown is due to the fact that as electrons are confined to tighter real space orbits by $B_{\perp}$, the uncertainty in their real space positions is decreased. The uncertainty in their momenta thus increases correspondingly, enabling tunneling when it becomes comparable to the gap in **k**-space separating the different Fermi surface orbits [27].

The concept of magnetic breakdown was first proposed in 1961 to explain the giant orbit observed by Priestley in the de Haas-van Alphen effect (oscillating magnetization as a function of magnetic field) in magnesium [101]. Since then magnetic breakdown has been observed in several metals and a few semiconductors [102 – 104]. Magnetic breakdown in semiconductors was first observed in metal-oxide-semiconductor structures on vicinal planes of silicon [103] and was later observed in similar structures on vicinal planes of indium antiminide [104]. In these structures, the valley-valley degeneracy is lifted when the bulk band structure is projected onto the vicinal surface. This results in a dispersion curve similar to that of Fig. 4.2, except that the two parabloids making up the dispersion

curve are always of equal size. More recently, magnetic breakdown was observed in periodically modulated 2DEGs, where the modulation potential causes the cyclotron orbit to drift in the direction perpendicular to the direction of modulation [105]. Also, Boebinger *et al.* [55] observed deviations from semiclassical behavior in DQWs subject to small tilted fields and Hu and MacDonald [56] later attributed this to magnetic breakdown.

In semiclassical magnetic breakdown theory, the probability P of breakdown occurring is given by $P = \exp(-B_o/B_\perp)$, where B_o is the breakdown field and is given by $B_o = (m^*/e\hbar)E_G^2/E_F$ where m^* is the effective mass of the circular orbit [101, 106]. For samples E and F this gives $B_o = 0.45$ T and 0.15 T, respectively. This qualitatively agrees with the data in that vertical ridges in R_{xx} appear at lower $B_\perp$ in sample F. Hu and MacDonald performed a quantum mechanical treatment of DQWs in tilted magnetic fields and obtained the expression [56]

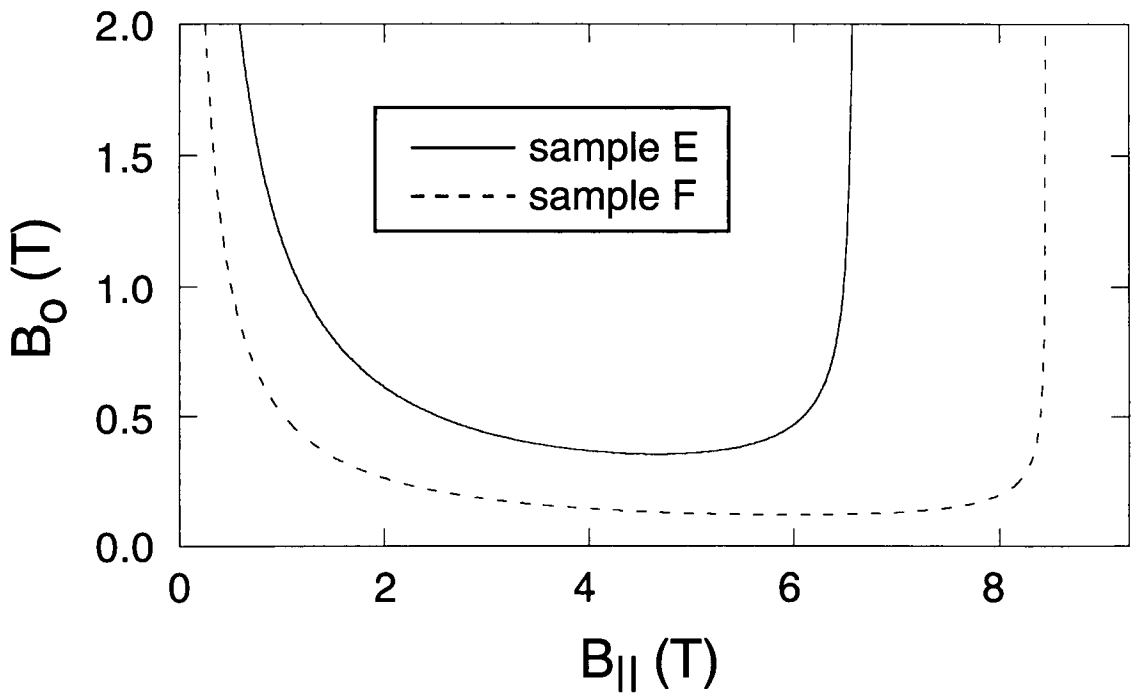

Fig. 5.6 Breakdown fields B_o for samples E and F calculated using the expression from Hu and MacDonald [56].

$$B_o = \frac{\pi m^* \Delta_{SAS}{}^2}{4e\hbar E_F(\Delta k/k_F)}\left[1-(\Delta k/2k_F)^2\right]^{-1/2}, \tag{5.1}$$

where $\Delta k = edB_{||}/\hbar$ as in Chapter 4, $k_F = (2\pi n)^{1/2}$, and $m^* = m^*_{GaAs}$. This treatment is valid only when μ is above the energy gap and both the lens and peanut orbits are present.

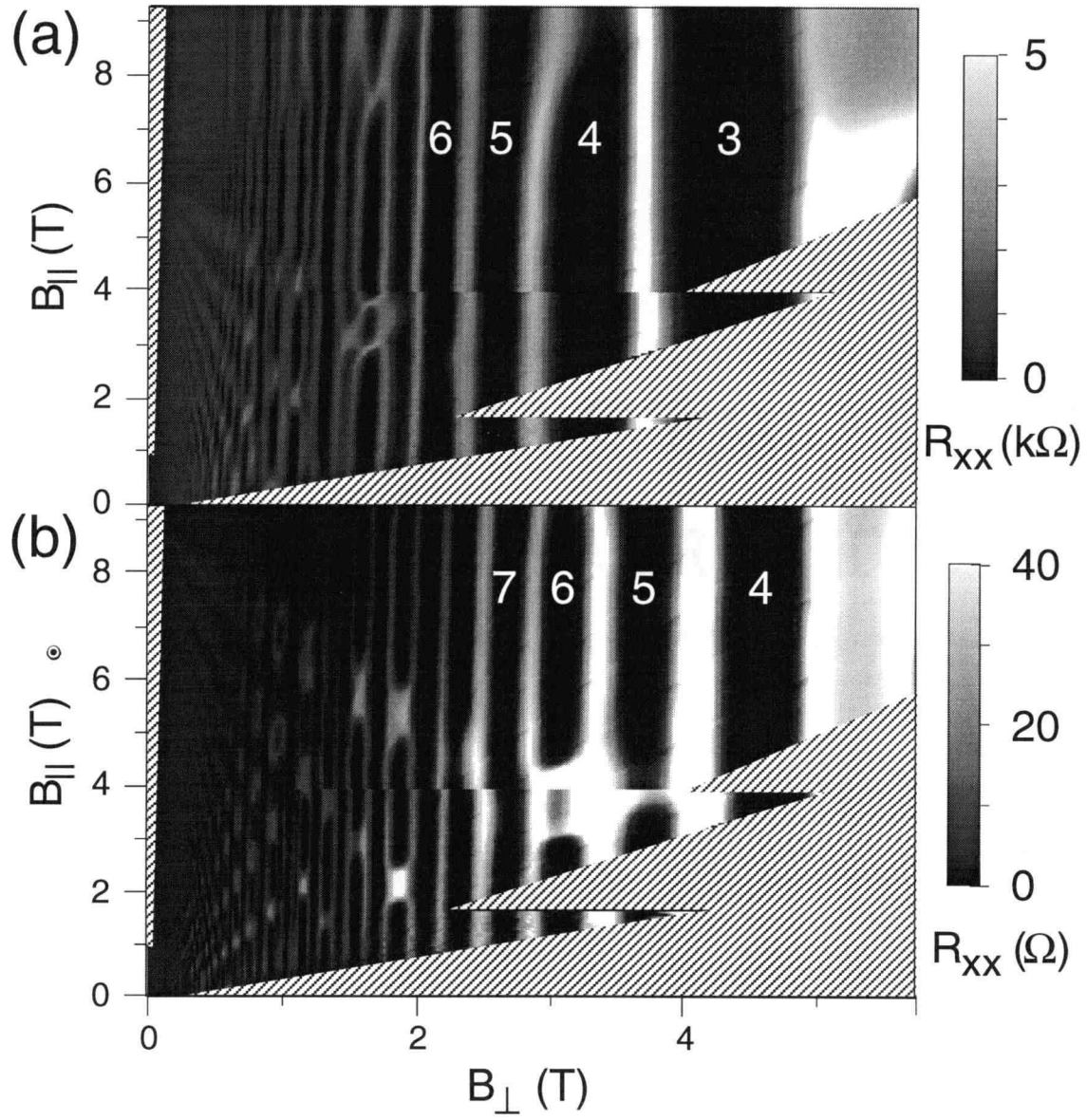

Fig. 5.7 Contour plots of R_{xx} versus $B_{||}$ and $B_\perp$ for (a) sample E and (b) sample F. These plots extend to higher $B_\perp$ than Fig. 5.3. The white numbers indicate the Landau level filling factors. Cross-hatching indicates regions where data was not obtained.

Fig. 5.6 shows the results of this calculation for samples E and F as a function of $B_{||}$. At the minima, this expression agrees fairly well with the semiclassically predicted B_o and also agrees in the fact that the lower Δ_{SAS} sample has a lower predicted B_o. Unfortunately, B_o can not be accurately determined from the experimental data.

Contour plots of R_{xx} versus $B_{||}$ and $B_{\perp}$ with $B_{\perp}$ extending to higher values than in Fig. 5.3 are shown in Fig. 5.7 for samples E and F. This plot shows that at higher $B_{\perp}$, where magnetic breakdown is expected to be nearly complete, R_{xx} is nearly independent of $B_{||}$ in sample E and for high $B_{||}$ in sample F. The data for sample F is somewhat strange because the ridge for the $N_{\ell} = 0$ Landau level in the lens extends to at least $B_{\perp} \approx 3.5$ T and the $N_{\ell} = 1$ lens Landau level extends to $B_{\perp} \approx 2$ T. This is not expected because with nearly complete magnetic breakdown there should be no features resulting from the lens or peanut orbits. Also, these ridges for sample F extend to higher $B_{\perp}$ than the corresponding ridges in sample E. This is surprising because magnetic breakdown is expected to be stronger in sample F.

One final point on magnetic breakdown concerns the electron orbits in real space when the sample is subject to tilted magnetic fields. In the dispersion curves of Fig. 5.4, we see that at $\pm k_y$, far from the anticrossing, the dispersion is parabolic, indicating that it is single QW-like. Thus, electrons at high $|k_y|$ are localized in one QW or the other; while electrons near the anticrossing at $k_y \approx 0$ are delocalized across both QWs. With applied $B_{||}$ and $B_{\perp}$, electrons on the peanut orbit at $-k_y$ start in the left QW. As they approach $k_y \approx 0$, they occupy both QWs simultaneously, and when they proceed to $+k_y$, they are in the right QW. Fig. 5.8 shows a schematic of this tunneling from left QW to right QW as electrons traverse the peanut orbit in real space. The situation is similar for the lens, except that $-k_y$ corresponds to the right QW and $+k_y$ corresponds to the left QW. When magnetic breakdown occurs, electrons remain on one circular orbit and thus no longer tunnel in real space from one QW to the other, as shown in Fig 5.8.

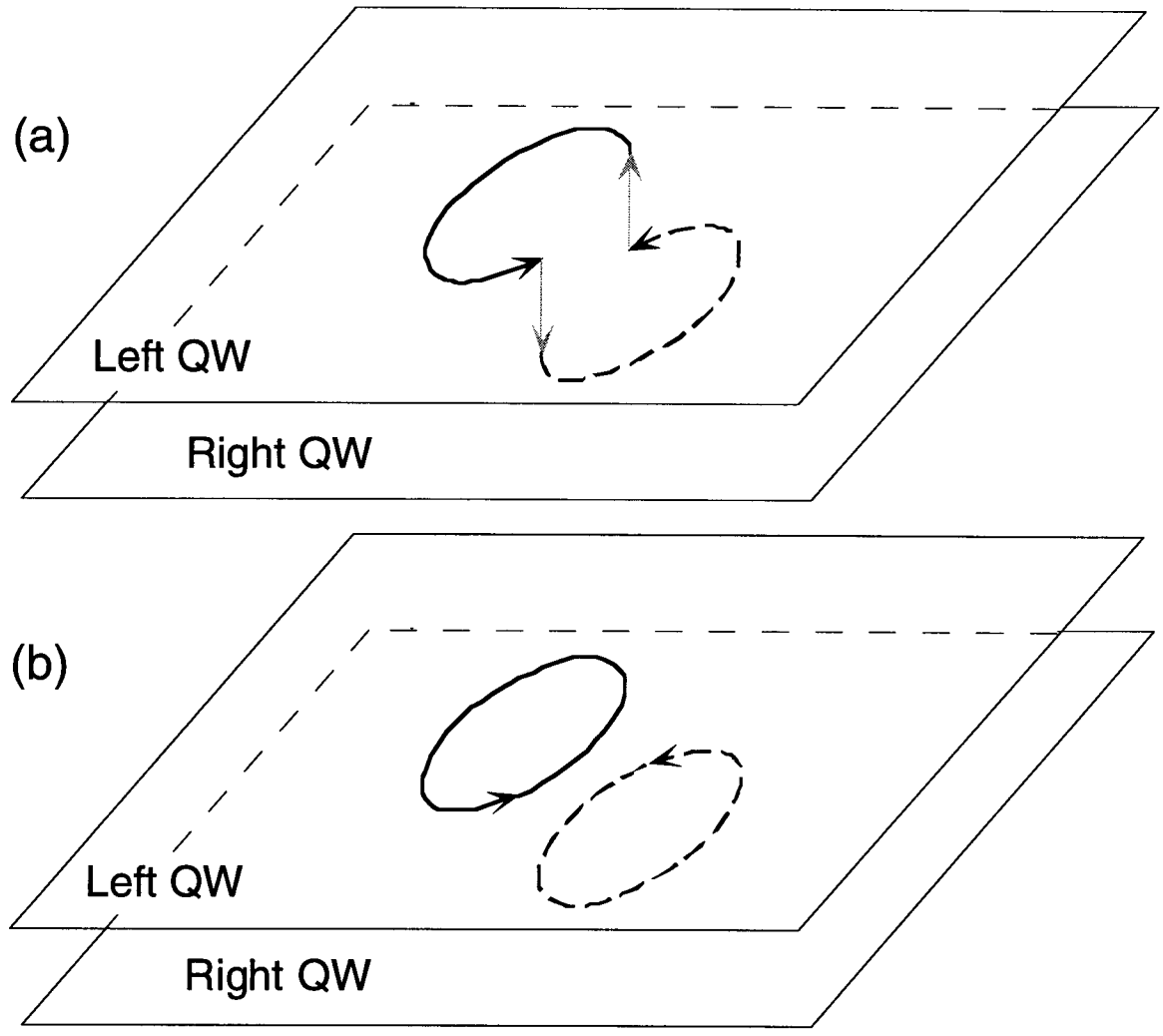

Fig 5.8 Schematic of the electron trajectories in real space for the cases of (a) no magnetic breakdown, and (b) magnetic breakdown occurring.

5.3 Semiclassical Calculation of Landau Levels

Next we turn to the semiclassical calculation of the $B_{\|}$, $B_{\perp}$ values at which the lens and peanut Landau levels cross μ. The original intent of this calculation was to verify the positions of the peanut Landau level resistance ridges and to provide a more quantitative test of our model. In the experimental data, the Landau levels are well-formed and a semiclassical treatment is not expected to be very accurate. This implies that a full quantum mechanical treatment is necessary to accurately reproduce the essential features of the data.

However, the semiclassical calculation agreed surprisingly well with the data. (A full quantum mechanical treatment also reproduced the data very well [107].) As previously stated, in Fig. 5.3(b), a series of peaks forming lines running from the lower left to the upper right with a smaller slope than the peanut Landau levels can be clearly seen. These lines can easily be mistaken for the peanut Landau levels and the results of this calculation show that they definitely are not the peanut Landau levels.

The Landau level positions are found by solving the Landau level energy relation $E_{\ell,p} = (N_{\ell,p} + 1/2)\,\hbar\omega_{\ell,p}(B_{||}, B_{\perp})$, with spin splitting ignored [99]. E_ℓ is the $B_{||}$-dependent Fermi energy of the lens orbit, and E_p is the Fermi energy of the peanut orbit, which is taken as a constant here. These energies are shown on the dispersion curve sketches of Fig. 5.4. $N_{\ell,p} = 0, 1, 2, \ldots$ are the Landau level indexes and $\omega_{\ell,p}(B_{||}, B_{\perp}) = eB_{\perp}/m^*_{\ell,p}(B_{||})$ are the cyclotron frequencies for the lens and peanut orbits, respectively. Solutions to this equation are obtained by fixing $N_{\ell,p}$ and $B_{||}$, then finding the $B_{\perp}$ which makes this relation an equality. This method assumes that each Fermi surface orbit is well-described by a constant m^* at each $B_{||}$ and also that $E_{\ell,p}$ are constant with $B_{\perp}$.

The masses $m^*_{\ell,p}(B_{||})$ and the lens Fermi energy E_ℓ are obtained from the $B_{||}$-dependent dispersion curve, which is calculated following Lyo's method [31] presented in Section 4.1. This calculation is done for $B_{||}$ in the range 0 – 9.5 T with a 0.1 T interval. Lyo used square QW potentials and their resulting wavefunctions as the basis in a tight-binding calculation. However, for closely coupled DQWs, this overestimates Δ_{SAS} because, in real structures, band bending pushes the electrons to the outsides of the QWs, resulting in less coupling between the QWs. To obtain more accurate values of Δ_{SAS}, band bending is artificially introduced by giving the bottoms of the QWs a non-zero slope, as shown in Fig. 5.9(a) for sample E. The slope was chosen to give an accurate Δ_{SAS} and was also compared to results from self-consistent Hartree calculations to ensure that the slope was reasonable. At $B_{||} = 0$ T, the measured $\Delta E = 3.2$ meV while the calculated is 3.7 meV and at $B_{||} = 5$ T, the calculated $\Delta_{SAS} = 2.1$ meV compared to the measured $\Delta_{SAS} =$

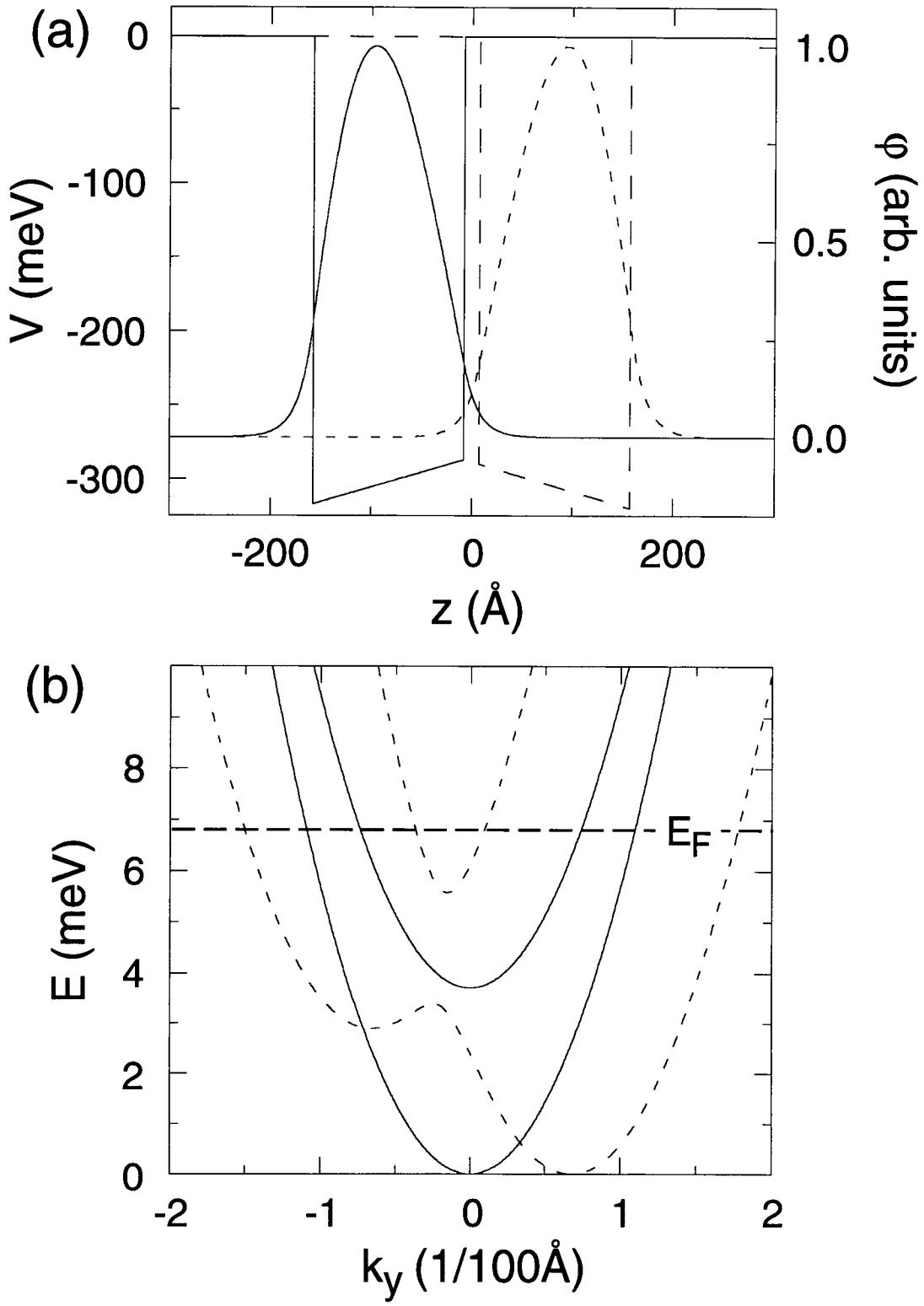

Fig. 5.9 (a) Plot of the QW potentials and wavefunctions used to calculate the dispersion curve for sample E. (b) Resulting dispersion curve for $B_{||} = 0$ T (solid lines) and $B_{||} = 5$ T (dashed lines).

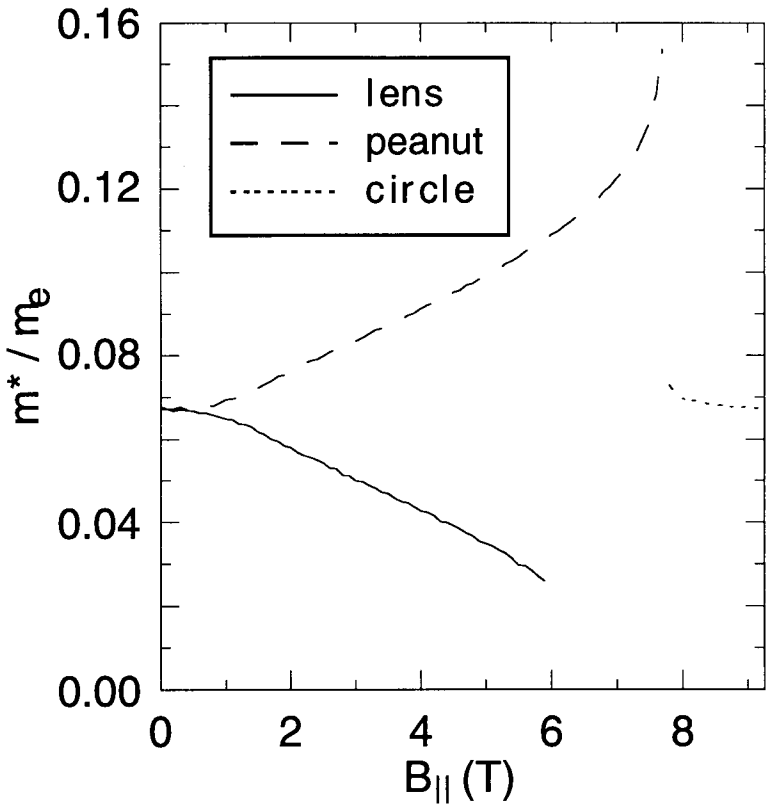

Fig. 5.10 Calculated m^* as a function of $B_{||}$ for the various Fermi surface components of sample E.

2.3 meV. The lens Fermi energy E_ℓ (see Fig. 5.4) is calculated as a function of $B_{||}$ directly from the dispersion curve and also the calculated dispersion curves are used in subsequent calculations of the electron effective masses of the lens and peanut orbits.

Next, the lens and peanut effective masses as a function of $B_{||}$ are calculated from the dispersion curves following Lyo [91] as presented in Section 4.3.2. Here the mass is given by $m^* = (\hbar^2/2\pi)\partial S/\partial\varepsilon$, where S is the area of the orbit in **k**-space, and ε is the electron energy at the Fermi surface. The results of this calculation are shown in Fig. 5.10 for the different Fermi surface orbits.

The results of the semiclassical calculation are the black lines in Fig. 5.3 and, as can be seen, the calculation reproduces the ridges in the experimental data very well. The sharp

R_{xx} peaks correspond closely with the calculated intersection points of the lens and peanut Landau levels. In sample F, these peaks form rows that appear to be the peanut Landau levels. However, as the calculation shows, these are rows of intersection points of lens and peanut Landau levels. The calculation's unusual behavior near $B_{||}$ = 7.5 T for sample E is due to the saddle-point in the peanut dispersion branch, where m^*_p diverges logarithmically and an infinite number of peanut Landau levels become occupied if E_p = constant is assumed. Although this approximation must break down at the saddle-point, R_{xx} is somewhat higher along $B_{||}$ = 7.5 T.

5.4 Fourier Power Spectra of R_{xx} Versus $1/B_{\perp}$

To further support the explanation for the R_{xx} data as a function of $B_{||}$ and $B_{\perp}$, the Fourier power spectra of the data versus $1/B_{\perp}$ are computed [86]. These are computed using the LabVIEW graphical programming language and the LabVIEW fast Fourier transform (FFT) subprogram which applies the split-radix algorithm to compute the FFT [108]. As stated in Section 5.1, with $B_{||}$ = constant, the oscillations in $1/B_{\perp}$ are periodic with a frequency that is proportional to the orbit's area in **k**-space. The Fourier power spectra should then give distinct peaks for the lens and peanut orbits, and also for the circular orbits that result from magnetic breakdown.

Fig. 5.11 shows Fourier power spectra of the data of sample F at $B_{||}$ = 2.0 T and 4.5 T, which are computed with $B_{\perp}$ in the range 0.1 − 1.2 T. Several peaks can be identified in the data. There is a low frequency peak from the lens orbit at $f \approx$ 3.3 T at $B_{||}$ = 2.0 T, which moves to lower frequency ($f \approx$ 1.9 T at $B_{||}$ = 4.5 T) with increasing $B_{||}$ due to the decreasing area of the lens orbit. A small peak for the peanut orbit appears at $f \approx$ 6.1 T at $B_{||}$ = 2.0 T, and moves to higher frequency ($f \approx$ 8.6 T) as $B_{||}$ increases, because of the increasing area of the peanut orbit. The lens peak is much stronger than the peanut peak because more electrons can traverse the lens without scattering due to its smaller size. Two

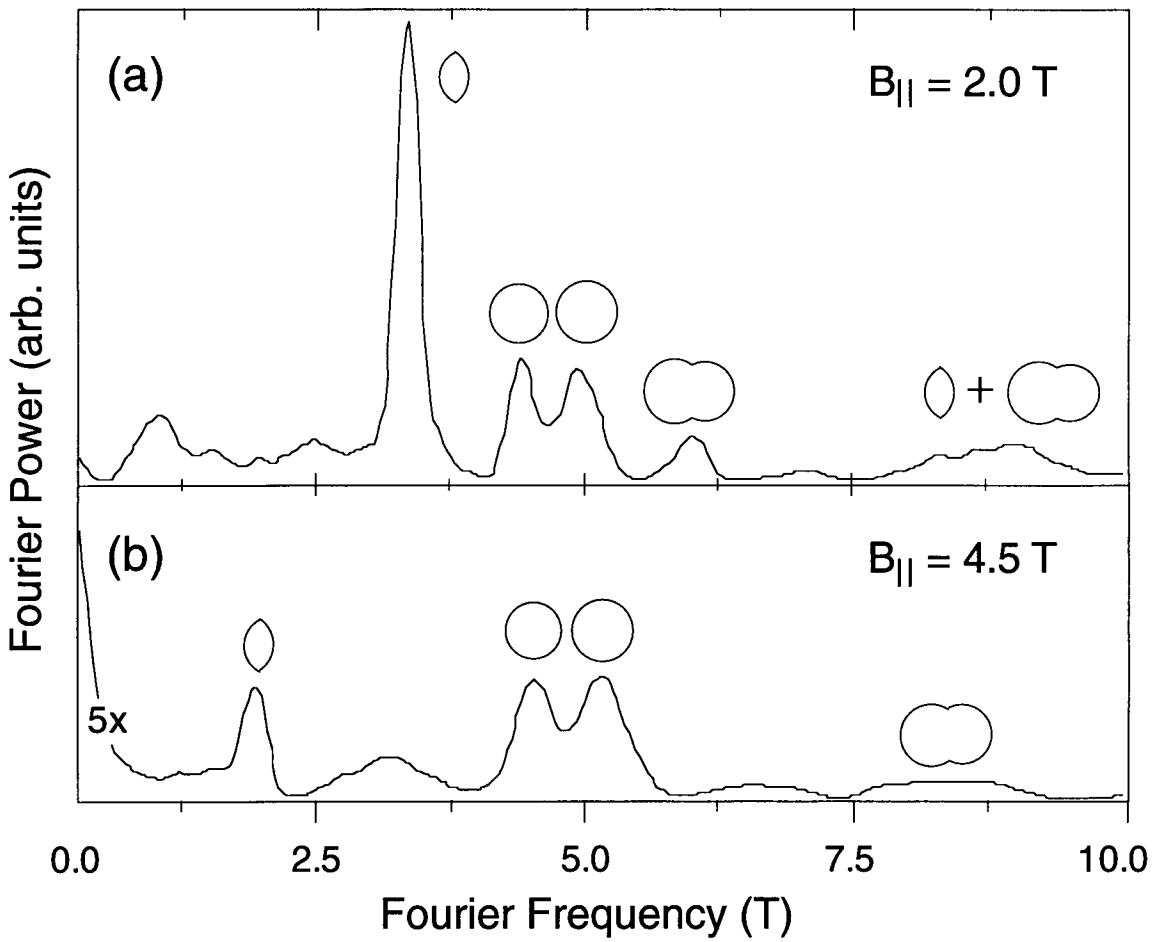

Fig. 5.11 Fourier transforms of R_{xx} versus $1/B_{\perp}$ for sample F at (a) $B_{||}$ = 2.0 T and (b) $B_{||}$ = 4.5 T. The various peaks are identified by the symbols near them. The lens (peanut) peak moves to lower (higher) Fourier frequency with increasing $B_{||}$, as expected.

intermediate frequency peaks ($f \approx 4.4$ T and 5.0 T) can also be seen and the frequencies of these peaks are approximately independent of $B_{||}$. These are from the circle orbits that result from magnetic breakdown. Because the dispersion is parabolic for the circle orbits, the Fourier frequency can be converted to density, where $n = (2e/h)f$. This gives $n_1 = 2.2 \times 10^{11}$ cm^{-2} and $n_2 = 2.5 \times 10^{11}$ cm^{-2}, which agrees very well with the $B_{||} = 0$ T densities measured for this sample which are $n_1 = 2.1 \times 10^{11}$ cm^{-2} and $n_2 = 2.4 \times 10^{11}$ cm^{-2}.

To get a clearer picture of how these orbits evolve with $B_{||}$, Fig. 5.12 shows gray-scale contour plots of the Fourier power spectra plotted versus $B_{||}$ for sample E and F. The

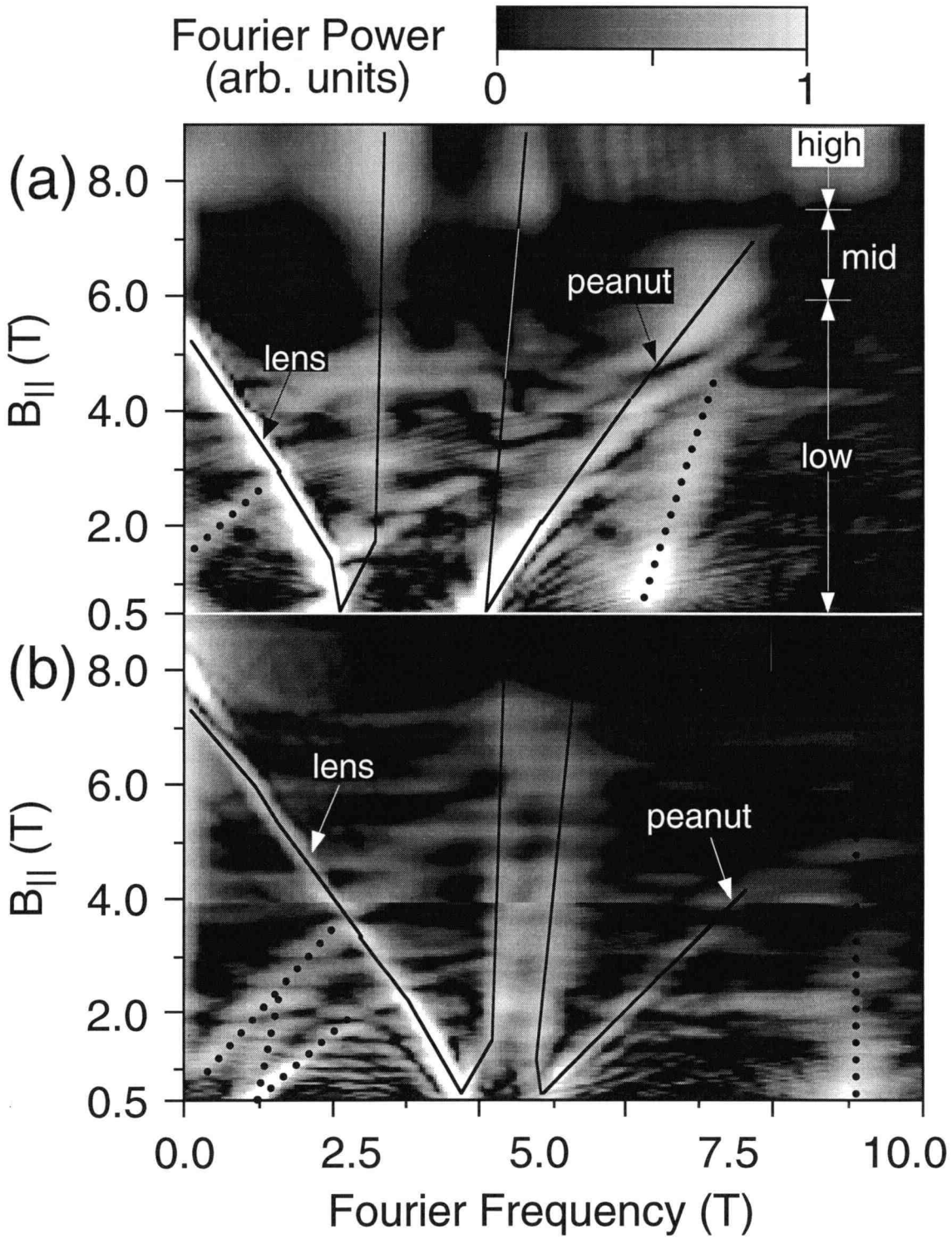

Fig. 5.12 Contour plot of the Fourier power spectra for (a) sample E and (b) sample F. The overlaid black lines are guides to the eye, indicating the orbit peaks (solid) and spurious aliasing peaks (dotted).

solid lines are guides to the eye, highlighting the ridges from the lens, peanut, and circle orbits. For both samples, the lens peak moves to lower frequency with increasing $B_{||}$ and the peanut peak moves to higher frequency. The two intermediate frequency peaks are due to magnetic breakdown and they remain relatively unchanged with $B_{||}$. These peaks change frequency a little at very low $B_{||}$ as the system changes from a gap $\Delta E \approx (\varepsilon_{1,2}^2 + \Delta_{SAS}^2)^{1/2}$ to a system with energy gap $\Delta E \approx \Delta_{SAS}$ [31]. This reduction of the energy gap decreases the difference in the areas of the two circle orbits. For balanced DQWs, the difference in areas goes to zero and a single intermediate frequency peak would be observed. The intermediate frequency peaks also have a slight drift to higher frequency with increasing $B_{||}$ due to a slight distortion of the shape of the individual QW circle orbits caused by $B_{||}$ [96, 97]. The magnetic breakdown peaks are more clearly seen in sample F which has a higher probability of magnetic breakdown than sample E. In sample E, the circle orbit peaks are clearly seen in the high $B_{||}$ regime where the two Fermi circles have separated and can also be seen in the intermediate $B_{||}$ regime, where magnetic breakdown occurs across the neck of the peanut orbit. Several small ridges occur due to aliasing and composite orbits [103] that occur when electrons traverse multiple orbits, such as the lens plus a circle or the peanut plus the lens. These ridges are highlighted by dotted lines in the figure. The aliasing occurs due to the relatively small number of oscillations found in the data, a small amount of noise in the data, and also from a small background slope in the data.

The Fourier frequencies of the various orbits can also be calculated from the **k**-space area of the Fermi surface orbit. The frequency is given by $f = 1/(2\pi)^2(h/e)A$, where A is the **k**-space area of the orbit. The areas of the circle orbits are obtained from the densities at $B_{||} = 0$ T and are used along with $\Delta k = edB_{||}/\hbar$ to geometrically calculate the areas of the lens and peanut orbits. Again, a d slightly larger than the QW center-to-center spacing is used to account for band bending. In these calculations $d = 175$ Å is used for both samples. The results of this calculation are shown in Fig. 5.13 for samples E and F. The agreement between the measured and calculated frequencies is very good for sample F and

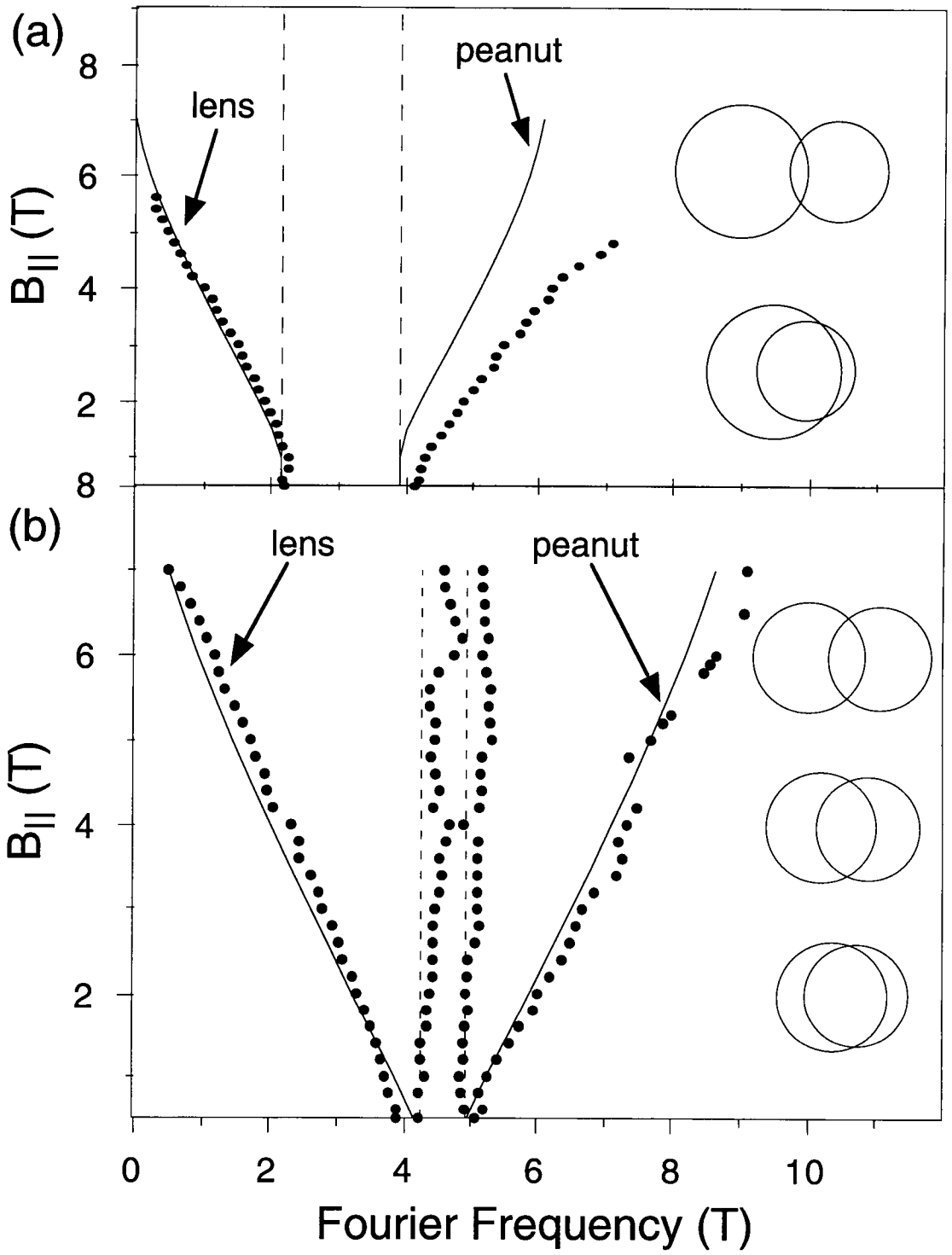

Fig. 5.13 Plot of the Fourier frequencies of the Fermi surface orbits of samples (a) E and (b) F versus $B_{||}$. The symbols are the measured frequencies, the dashed lines are the measured $B_{||}$ = 0 T circle orbit frequencies, and the solid lines are the geometrically calculated frequencies for the lens and peanut orbits. Sketches of the Fermi surfaces for different values of $B_{||}$ are also shown.

for the lens orbit of sample E. The error for the peanut orbit of sample E is quite large and is probably due to the fact that the distortions in the circles due to the energy gap were ignored in the calculation. Including this effect would increase the frequencies of the peanut orbit and decrease the frequencies of the lens orbit. The changes would be very small for sample F because Δ_{SAS} is relatively small, but could be much larger for sample E because its Δ_{SAS} is fairly large.

The R_{xx} versus $B_{||}$ and $B_{\perp}$ data, and, in particular, the Fourier power spectra of this data, clearly show that magnetic breakdown is occurring in both samples. However, a determination of the breakdown field B_o is not possible with these measurements. One possible method for determining B_o with this data is to compute the Fourier power over small ranges of $1/B_{\perp}$ and then to identify the range in which peaks for the circle orbits appear. However, this involves computing the Fourier power for data sets with only a couple of oscillations, which results in large errors and low sensitivity. This method was tried and no meaningful peaks appeared in the power spectra. Other methods for analyzing this data to determine B_o can be envisaged, but they seem doomed to failure for the same reasons that the method presented here failed. Other possible experimental approaches to this problem will be presented in Chapter 7.

5.5 Chapter Summary

In this chapter, the evolution of the Landau levels with changes in the dispersion curve were investigated. The dispersion was continuously and controllably distorted by changing the in-plane magnetic field, while the Landau level spacing was changed by varying the perpendicular magnetic field. Experimentally, the magnetoresistance was mapped by measuring the resistance as a function of B_T with the sample mounted at different angles. For this work, approximately nine hundred B_T-sweeps were done. Previously, measurements at low $B_{||}$ with changing $B_{\perp}$ were performed and the results compared with

semiclassical theory [55]. Deviations from semiclassical behavior were later attributed to magnetic breakdown [56]. However, in that work, $B_{||}$ was too low for the energy gap to form and the results were plotted as single traces only, not as contour plots. In the present work, plotting the data on contour plots showed the evolution of the Landau levels from the lens and peanut orbits and also from the circle orbits that resulted from magnetic breakdown. A semiclassical calculation of the Landau level positions as a function of $B_{||}$ and $B_{\perp}$ showed good agreement with the data. These results were published in references [99, 100]. Contour plots of the Fourier power spectra showed $B_{||}$-dependent peaks for the lens and peanut orbits. $B_{||}$-independent peaks, which occur due to magnetic breakdown, were also observed

6. ONE-DIMENSIONAL STRUCTURES ON DOUBLE QUANTUM WELLS

One-Dimensional and quasi-one-dimensional structures on single 2DEGs have been extensively studied over the last 15 years [109]. Ballistic transport and truly 1D behavior has been observed in quantum point contacts (QPCs), which have channel lengths (L) that are much shorter than the electron mean free path (ℓ) [13]. In these devices, electrons traverse the channel without scattering. Diffusive transport has been observed in longer structures (referred to as quantum wires in this work) where the channel length is longer than the mean free path [109]. Electrons in these devices suffer elastic scattering within the channel. However, this scattering does not destroy the phase coherence and quantum interference effects can be observed in these devices. The phase coherence length is the characteristic length scale in these devices. This chapter discusses two experiments involving 1D structures on double quantum wells. There has been very little work in this area, most likely due to difficulties in fabricating samples, which will be discussed below. Our experimental work has focused on QPCs and short quantum wires subject to in-plane magnetic fields.

6.1 Quantum Point Contacts on DQWs

Our discussion of QPCs begins with a description of QPCs on single 2DEGs. There has been much work on QPCs on single 2DEGs and several reviews of these structures have been written [13, 109]. A brief review of the experimental results and theoretical explanations for these results is given below. The steps for fabricating these devices and the device geometry were discussed in Section 3.2.

In QPCs defined using the split gate technique (upper left inset of Fig. 6.1), the QPC forms when the 2DEG under the gates is depopulated as a negative bias is applied to the gates (lower right inset of Fig. 6.1) [110, 111]. The resulting channel is quasi-one-

dimensional when more than one subband is occupied and transport through it is ballistic. Electrons are confined in z-direction by the growth structure, they are confined in the y-direction by the split gates, and they are free to move along the x-direction only. The confinement in the y- and z-directions results in 1D subbands with energy $E_n(k) = E_n + \hbar^2k^2/(2m^*)$ where E_n is confinement energy of the n-th subband, k is the wave vector for propagation along the x-direction, and $m^* = m^*_{GaAs}$ [13]. The number N of occupied subbands at E_F is the largest integer such that $E_N < E_F$. The transport is ballistic because the length ($L < \approx 1$ μm) of the channel is much shorter than the mean free path ($\ell = \tau v_F = \hbar\mu(2\pi n_s)^{1/2}/e \approx 10$ μm) [33] and therefore, electrons do not scatter within the channel.

Experimentally, QPCs exhibit a conductance (G) that is quantized in steps of $2e^2/h$ as a function of gate bias (V_G) [110, 111]. The conductance is given by $G = [R(V_G) - R_b]^{-1}$ where $R(V_G)$ is the measured resistance and R_b is a background series resistance that is taken as a different constant $\approx 400\ \Omega$ for each device. The idealized conductance for a QPC is sketched in Fig. 6.1. Each 1D subband contributes $2e^2/h$ to the conductance and the steps occur as the 1D channels are depopulated as V_G is made more negative. The energy at the bottom of the constriction (E_c) is greater than the energy in the wide 2DEG regions and increases as V_G is made more negative [13]. This reduces the electron density in the constriction from the bulk density n_s roughly by a factor $(E_F - E_c)/E_F$. The reduction in N is due both to a decrease in the channel width (W) and to the increase in E_c. The accuracy of quantization is only about 1%, partially due to the background resistance which can not be accurately determined, while in the quantum Hall effect, the quantization has an accuracy of about 10^{-6} % [20]. Both the degree of flatness of the plateaus and the sharpness of the transitions between them vary among devices with identical design, indicating that the detailed shape of the electrostatic potential defining the QPC is important [13].

To understand the source of the conductance quantization, we calculate the current per unit energy interval injected into a subband. The current is injected into the channel within a narrow range $\delta\mu$ above E_F into the N 1D subbands. The current per unit energy is the

product of the group velocity and the 1D density of states [13]. The group velocity is $v_n = \hbar^{-1} dE_n(k)/dk$, and the density of states, including spin, is $\rho_n = (\pi dE_n(k)/dk)^{-1}$. From this we see that the product of v_n and ρ_n is independent of both energy and subband index. Indeed, the product is even independent of the form of the dispersion relation $E_n(k)$. The injected current is therefore equally shared by all of the occupied subbands with each subband carrying a current = $ev_n\rho_n\delta\mu = (2e/h)\delta\mu$ and thus the conductance of each subband is $G = I/(\delta\mu/e) = 2e^2/h$. This result can also be obtained using the Landauer-Büttiker formalism as is done in Reference [13]. The 1D dispersion curve for a QPC with three occupied subbands is sketched in Fig. 6.2. The states that carry the net current through the QPC are indicated by the shaded box on the $+k$ side of the dispersion curve,

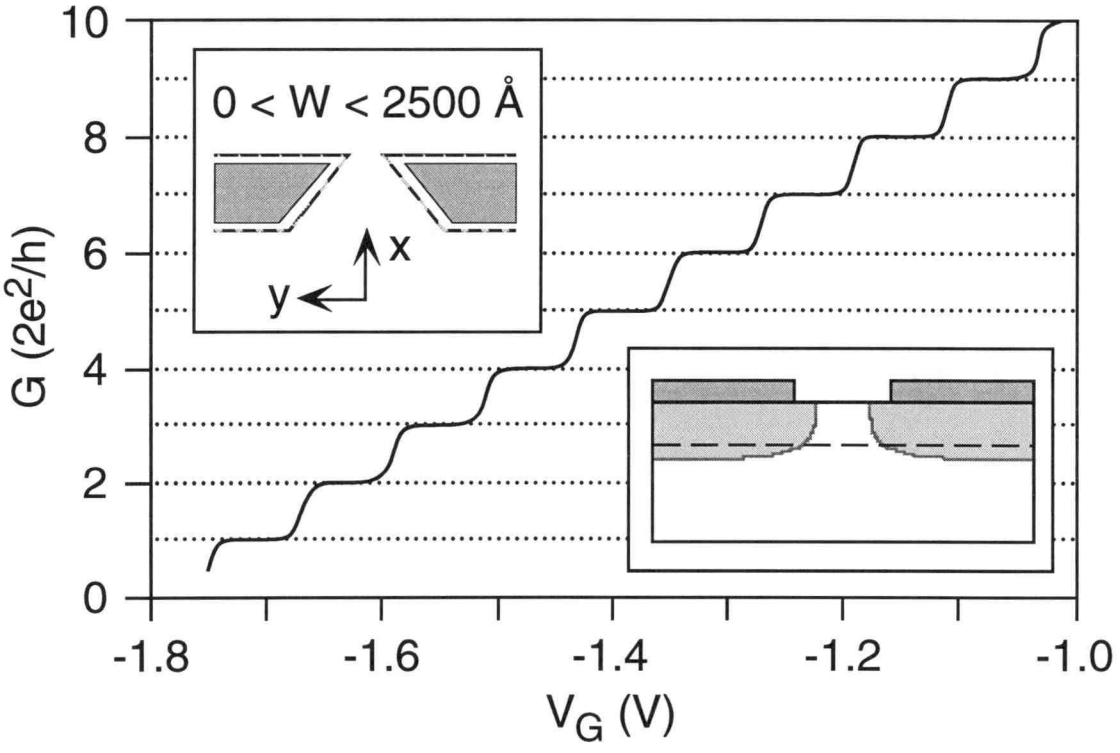

Fig. 6.1 Sketch of the conductance G versus gate voltage V_G for a quantum point contact on a single 2DEG. The upper left inset shows a top view of the split gates and the lower right inset shows a cross-sectional view of the sample showing the gates and their depletion regions.

where the height of the box is $\delta\mu$. The dispersion curve for each subband crosses E_F at two points known as Fermi points (one each at $\pm k_x$), indicated by vertical arrows in the figure. Thus, G can be viewed as having a contribution of $2e^2/h$ from each pair of Fermi points.

QPCs on coupled DQWs are expected to behave similar to QPCs on single 2DEGs, where each occupied subband contributes $2e^2/h$ to the total conductance. For the DQW case, there will be two channels, each with an integer number ($N_{1,2}$) of occupied subbands. The two channels are in parallel so their conductances will add and the total conductance will exhibit steps of $2e^2/h$ when subbands in either channel are depopulated.

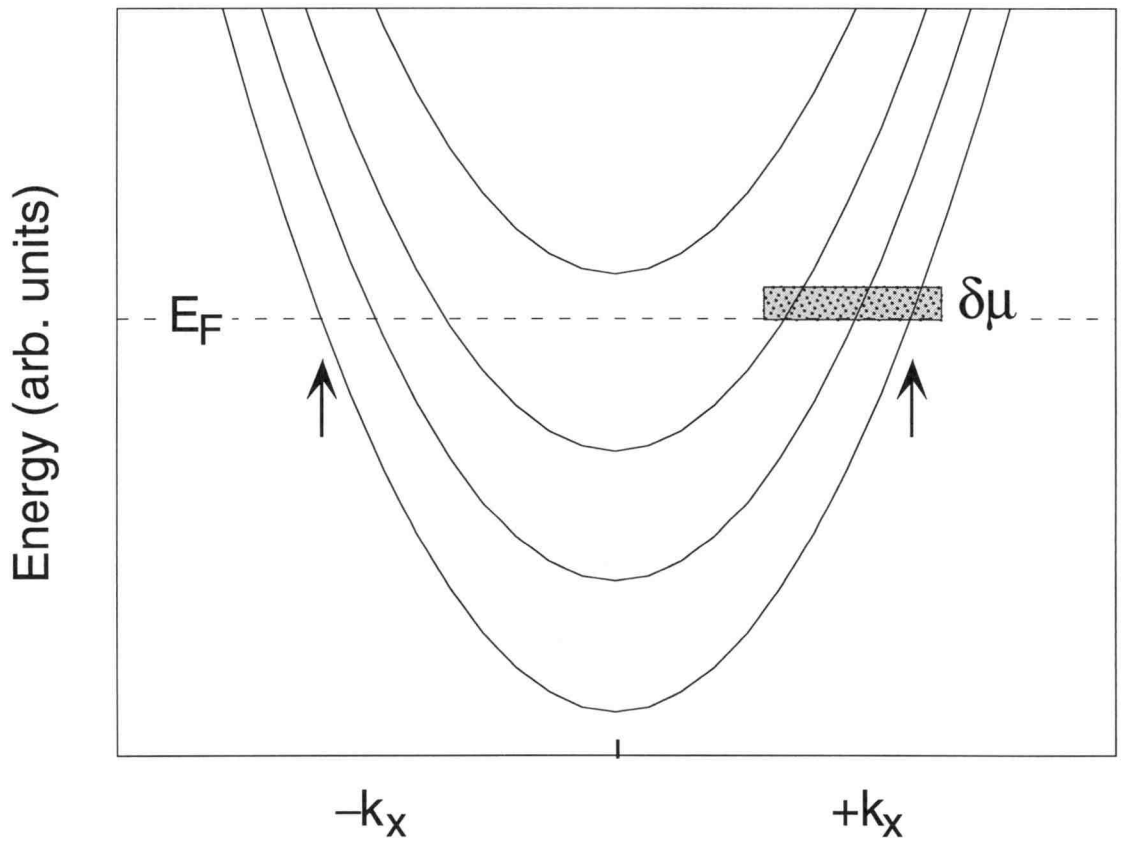

Fig. 6.2 Sketch of the 1D dispersion curve of a QPC with three subbands occupied. The shaded box indicates $\delta\mu$ and the states that carry the net current. The dashed line indicates the Fermi energy and the vertical arrows show the Fermi points of the $n = 1$ subband.

When a magnetic field ($B_{||}$) is applied in the growth plane (x, y-plane) and perpendicular to the conducting channel (in the y-direction), the 1D dispersion curves in each QW will shift in the k_x-direction with respect to one another, and, for coupled QWs, they will anticross, similar to the 2D case. When the magnetic field is applied parallel to the conducting channel (x-direction), the dispersion curves will shift in the k_y-direction and they will not cross and the transport will be unchanged.

When one subband is occupied in each QW, the conductance is expected to have step increases and decreases as a function of $B_{||}$ as the number of subbands changes due to the anticrossing moving through E_F. Fig. 6.3 shows a schematic of the dispersion curve, and

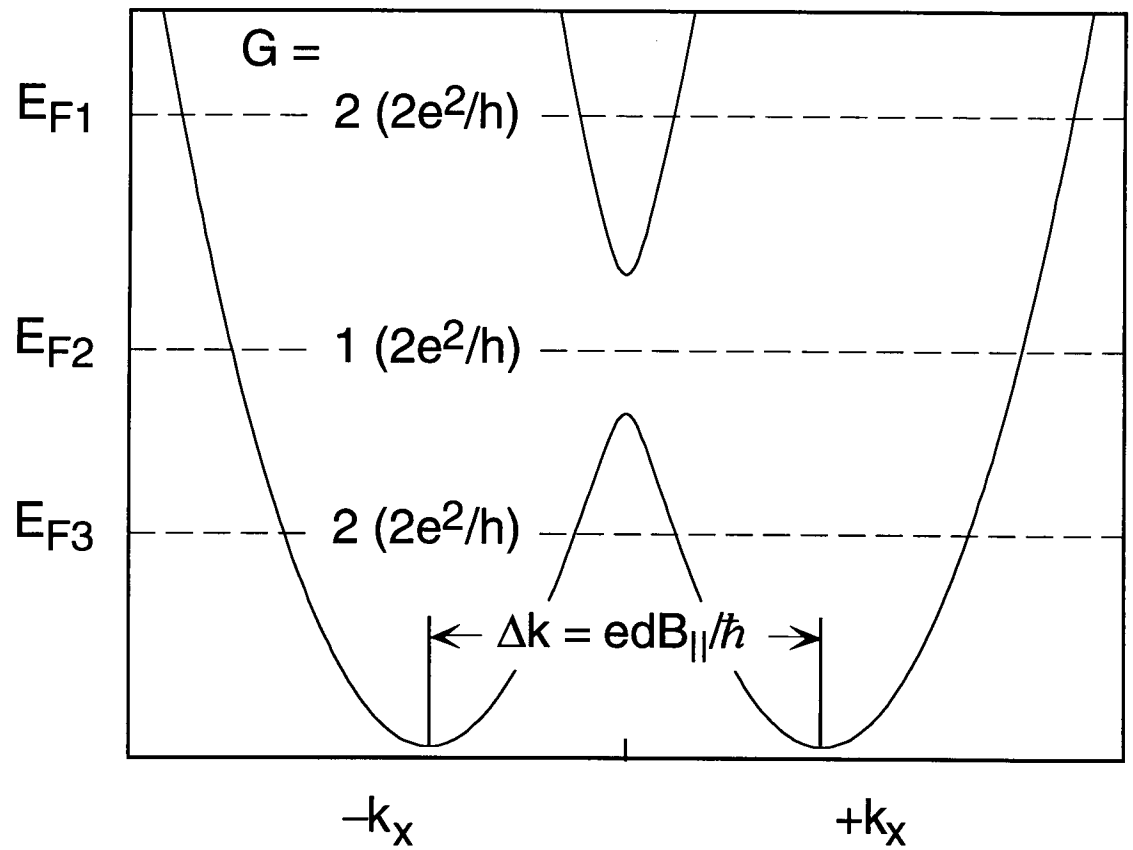

Fig. 6.3 Sketch of the 1D dispersion curve for a QPC formed on a DQW with an applied in-plane magnetic field. Each QW has one subband occupied. The conductance for three different values of E_F are shown.

the corresponding conductance, for different values of E_F at constant $B_{||}$. For high E_F (E_{F1}; above the energy gap) and low E_F (E_{F3}; below the energy gap), both subbands are occupied and the conductance is $2(2e^2/h)$, while at intermediate E_F (E_{F2}; in the energy gap) only the lower subband is occupied and the conductance drops to $2e^2/h$ [112]. In real devices, E_F is constant and $B_{||}$ is increased to move the energy gap to higher energy. In that case, E_{F1} corresponds to low $B_{||}$ where the Fermi energy is above the energy gap and two subbands are occupied. As $B_{||}$ is increased, the conductance drops when the energy gap reaches E_F (E_{F2} in the figure) and only one subband is occupied, and at still higher $B_{||}$, the conductance increases when the energy gap moves above E_F (E_{F3} in the figure) and two subbands are again occupied.

The goal of our experiments on QPCs on DQWs is to verify these predictions of step increases and decreases in the conductance of these devices as a function of $B_{||}$. In the first attempt, QPCs were made on sample G, which is from the same wafer as sample E of Chapter 5. Four QPCs were fabricated on this sample; two with a 0.5 μm separation between the split gates and the other two with a 0.7 μm separation. Of these devices, two had the conducting channel parallel to $B_{||}$ and, in the other two, it was perpendicular to $B_{||}$.

Fig. 6.4(a) shows a plot of the four-terminal resistance (R) versus gate voltage (V_G) for low V_G for the 0.5 μm device with current perpendicular to $B_{||}$. The top QPC forms at $V_G \approx -0.3$ V, as indicated in the figure. No features are seen on the scale used in the figure, however, on an expanded scale, a change of slope is seen near $V_G = -0.3$ V. Also, from gate scans on Hall bars on other samples from this wafer, the top QW depletion voltage is known to be ≈ -0.3V. The resistance changes very little at this point because the channel is fairly wide and thus has a low resistance and the bottom QW is still very low resistance. As V_G is decreased, there are no steps seen in the resistance from subbands being depopulated. This is because the steps are washed out by the low resistance of the bottom QW. A sharp rise in resistance below $V_G \approx -0.5$ V occurs as the bottom QW is being depleted. Near $V_G \approx -0.65$ V, the bottom QW is depleted under the gates and the

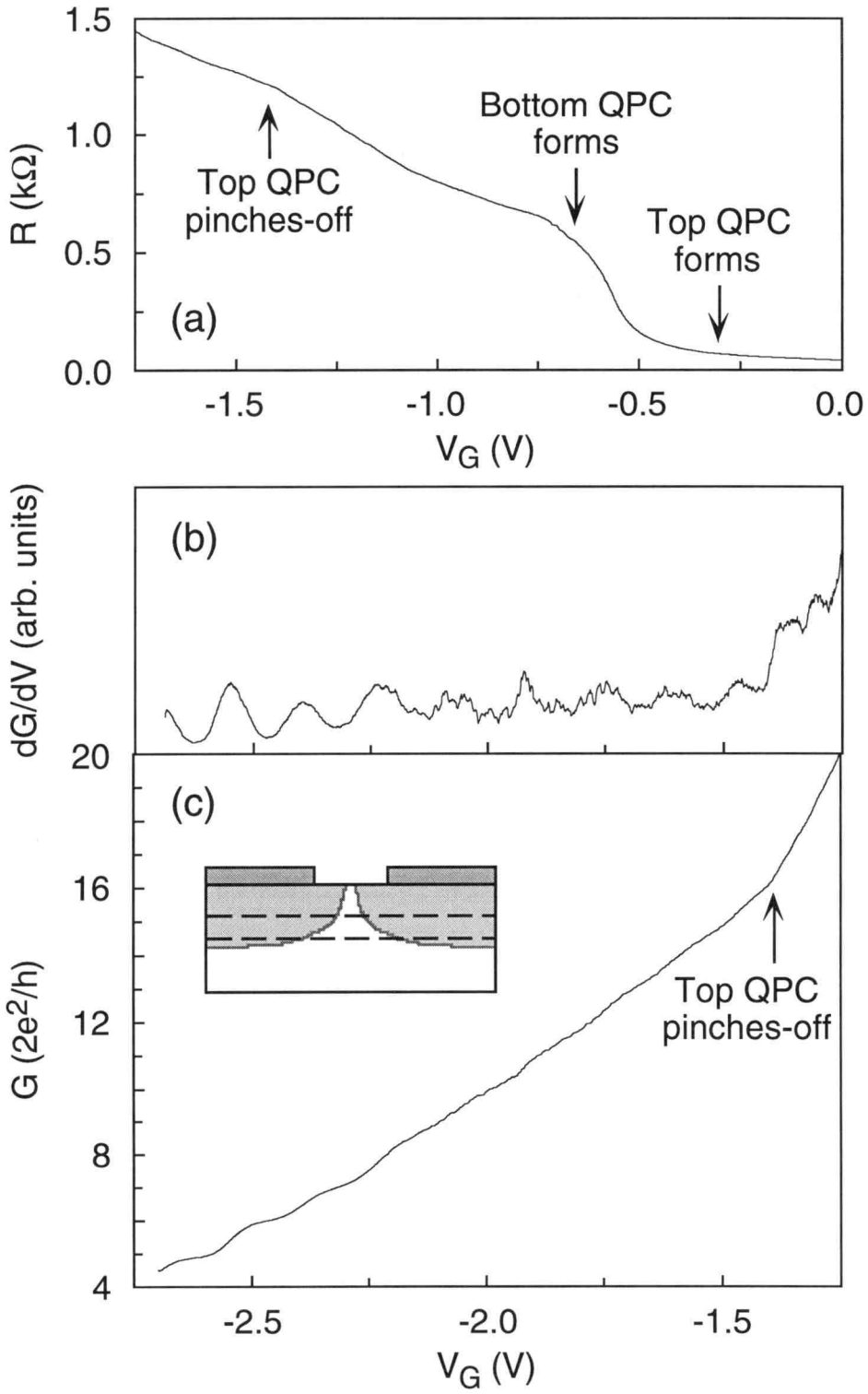

Fig. 6.4 (a) Resistance of the QPC as a function of gate bias at low V_G. (b) Derivative of the G and (c) G as a function of gate bias at more negative V_G. Below $V_G \approx -1.4$ V, only the bottom QPC is occupied. The inset to (c) schematically shows the widths of the two QPCs.

bottom QPC has formed. From $V_G \approx -0.65$ V to -1.4 V, the number of subbands in both QPCs is decreasing, but because so many subbands are occupied, the steps in R can not be resolved. At $V_G \approx -1.4$ V, the top QPC becomes too narrow for subbands to be occupied in it and it pinches-off. The change in slope at this point indicates that the top QPC is pinching-off here.

Fig 6.4(b) and (c) show the slope of the conductance (dG/dV_G) and the conductance, respectively, for this device as a function of V_G at more negative gate bias. The conductance is given by $G = 1/(R - 0.4\ \text{k}\Omega)$, where $R_b = 0.4\ \text{k}\Omega$ was chosen such that the plateaus appear at integer values of $2e^2/h$. The change in slope that occurs when the top QPC pinches-off is clearly seen in Fig. 6.4(c). At more negative bias ($V_G < -2.0$ V), steps in G can be seen. The lowest plateau corresponds to five occupied subbands in the bottom QPC. The derivative of G shown in Fig. 6.4(b) has minimum values at the plateaus in G and these minima can be seen as high as $V_G \approx -1.5$ V, even though true plateaus can not be seen in G at these gate biases. The data in Fig. 6.4 indicates that when both QPCs are occupied, the top QPC has fewer occupied subbands, and is thus much narrower, than the bottom QPC. This is partly due to screening of the electric field by electrons in the top QW. The widths of the two QPCs are shown schematically in the inset of Fig. 6.4(c). Due to the large difference in the widths of the two QPCs, the anticrossing in the 1D dispersion is not expected to be seen because the total dispersion is extremely complicated with one subband occupied in the top QPC and many subbands occupied in the bottom QPC.

A second QPC sample was fabricated using a slightly different technique to give the two QPCs the same widths. These devices were fabricated on sample H, which is from the same wafer as sample A of Chapter 4. Four devices with the same geometries and separation between gates as those of sample G were fabricated. The difference between the two samples is that after e-beam resist is patterned and developed, the gate areas of this sample were etched to a depth of ≈ 730 Å in phosphoric acid (1:4:495 H_3PO_4:H_2O_2:H_2O).

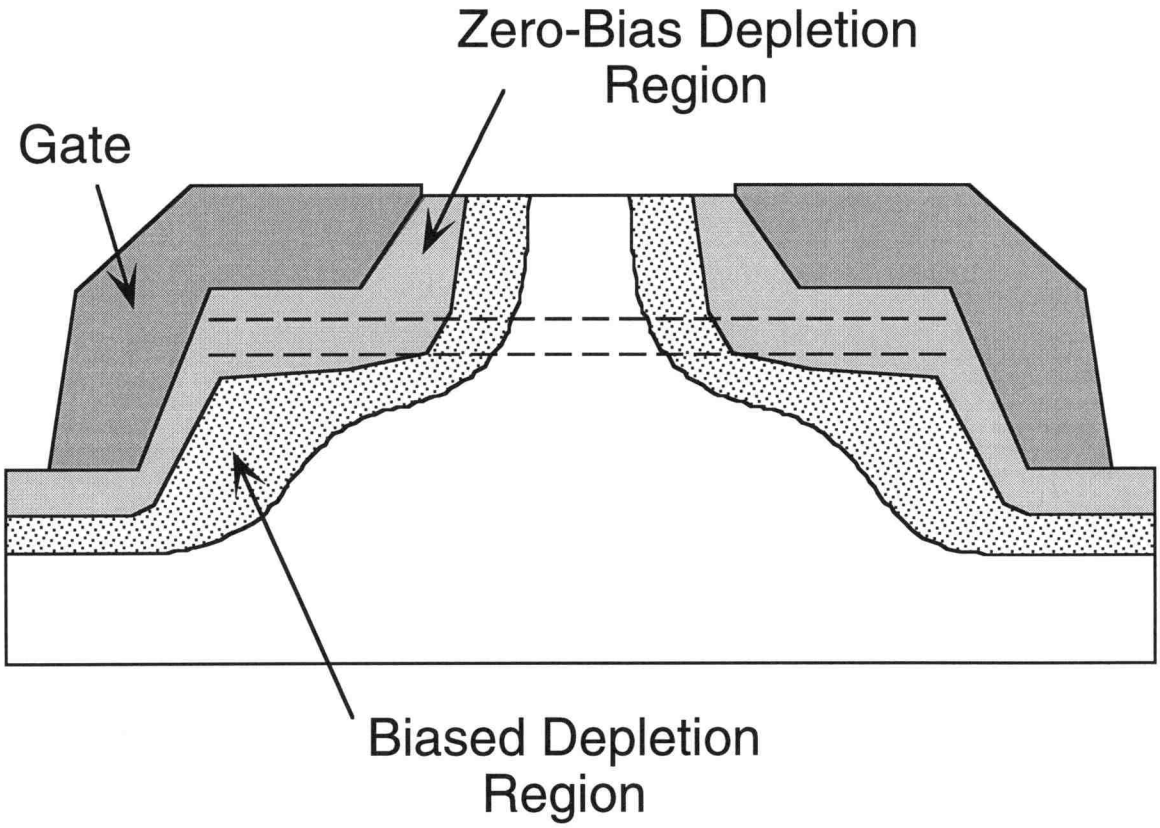

Fig. 6.5 Schematic of sample H after etching and depositing the gates.

After the etch, the resist was left on the sample and the gate metal was evaporated on to the sample and lifted off.

Fig. 6.5 shows a schematic of the sample after the gate metal was deposited. The etch was deep enough to remove the top layer of dopants (see typical growth structure in Fig. 2.1). After the etch, the QWs under the gates are depleted because the dopants above them were etched away and also because the surface is pinned at roughly 0.8 eV above the Fermi energy.

Fig. 6.6(a) shows the resistance of sample H as a function of V_G for a 0.5 μm device with the current parallel to $B_{||}$. The resistance is higher near V_G = 0 V in this sample than in sample G. This indicates that at least the top QPC and possibly the bottom QPC are formed by the gate etch. Fig 6.6(b) shows the measured conductance which was obtained

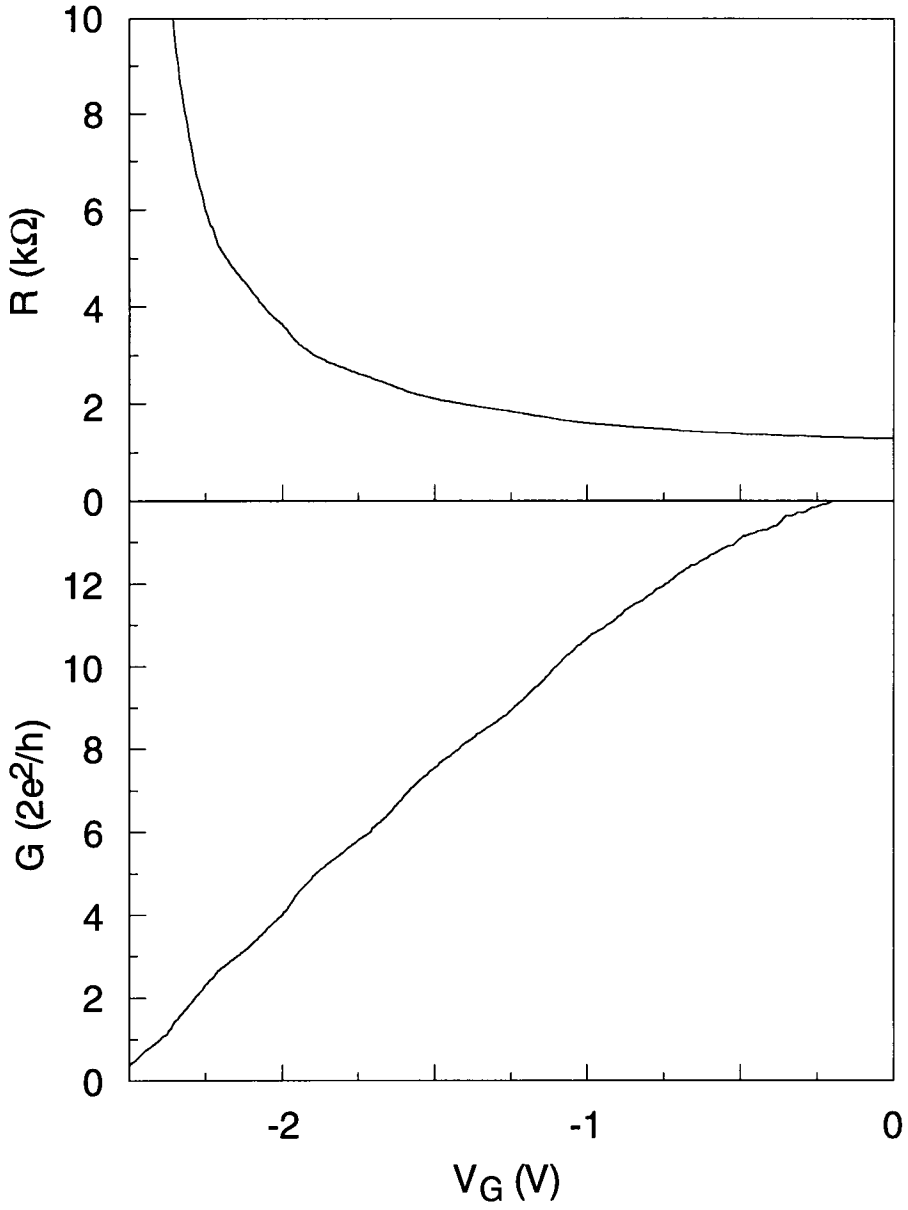

Fig. 6.6 (a) Resistance and (b) conductance of sample H as a function of V_G. Weak plateaus can be seen in (b).

using R_b = 0.5 kΩ. Extremely weak plateaus can be seen in this data but, because the plateaus are so weak, it is difficult to be confident in the choice of R_b. Due to the uncertainty of R_b and the weakness of the plateaus, it is also difficult to identify the number of subbands occupied. In measurements of $G_{||}$ as a function of $B_{||}$ (not shown), the

anticrossing of the 1D dispersion curve was not seen. We believe this is because the plateaus in the conductance are so weak.

The ideal sample for these experiments would have split gates defined on both the top surface and on the back surface of the sample. This would allow independent control of the QPC widths in each QW. However, the substrates on typical samples are $\approx$ 600 μm thick and they can be thinned to only $\approx$ 50 μm before they become too fragile to work with. Large-area back gates have been made on such thick substrates but $V_G \approx -100$ V is necessary to deplete the bottom QW [60]. Even though back gates can be made on these substrates, the substrates are much too thick to allow definition of QPCs with back gates. The problem is that sharp features defined by the gates become rounded and slightly distorted in the depletion region under the gate. Thus, the QPCs made on these thick substrates would become very long and the plateaus would be washed out.

To overcome this problem, we have developed a technique to make back gates that are as little as $\approx$ 0.4 μm from the bottom QW [61]. This technique is known as EBASE (Epoxy-Bond And Stop-Etch) and has been used to make samples with large-area back gates. In this technique, first the mesa, ohmic contacts, and large-area top gates are processed. Next, alignment marks are defined with optical lithography, etched to a depth of $\approx$ 0.5 μm, and filled with metal. The top e-beam defined split gates are aligned to these marks. Now the sample is epoxied, face down, on a host substrate and the sample substrate itself is thinned to $\approx$ 50 μm. The rest of the sample substrate is etched away in a selective etch that stops on the AlGaAs buffer layer (see Fig. 2.1). This leaves a smooth surface with the etched alignment marks protruding from the surface. The sample now consists of $\approx$ 0.5 μm of epitaxial layers epoxied to the host substrate. The back e-beam defined split gates are aligned to the etched alignment marks and finally via holes are etched to make contact to the ohmic contacts and the top gates. Fig. 6.7 shows a cross-sectional view of the completed sample. Using this technique, the top and back split gates should be accurately aligned to each other and should provide the independent control of the top and

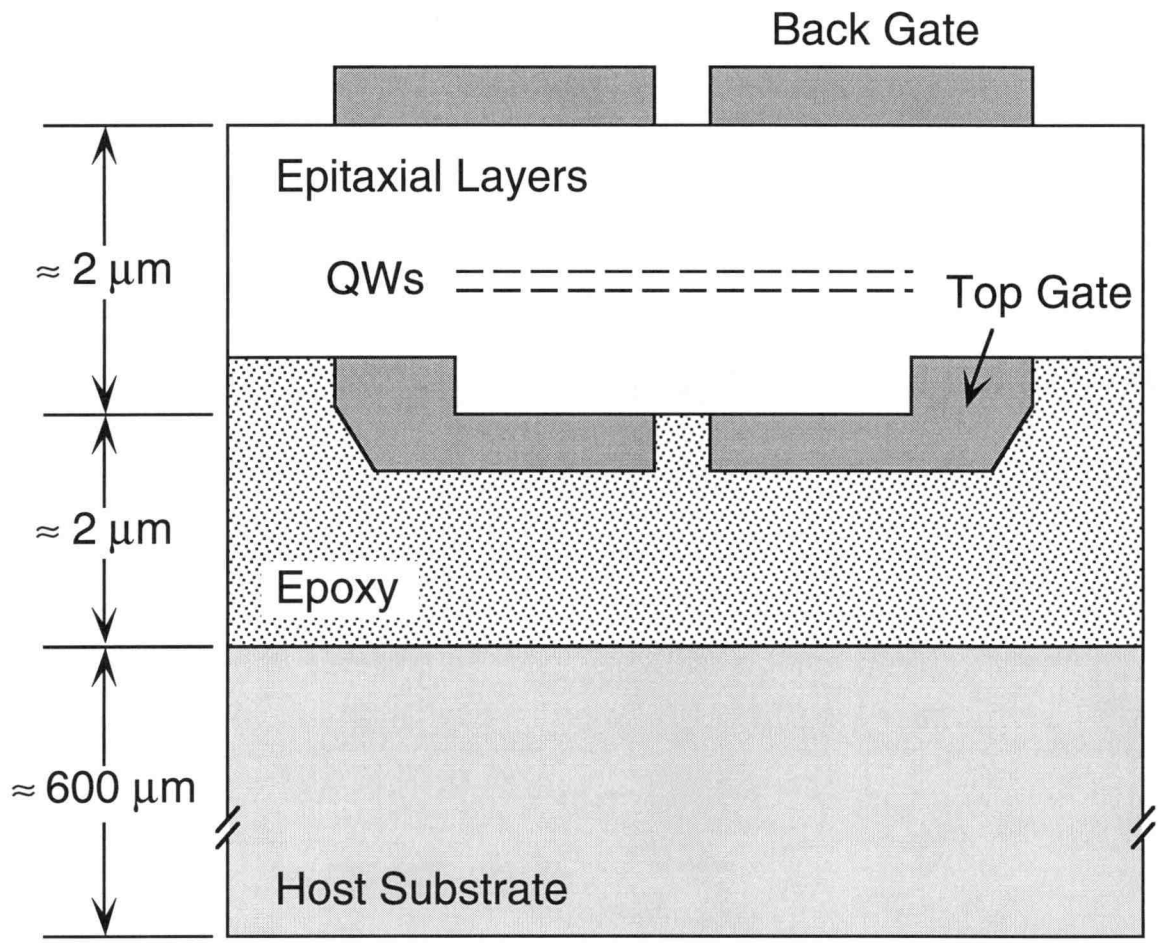

Fig. 6.7 Cross-sectional view of QPC sample after processing using the EBASE technique.

bottom QPCs that is necessary to make this experiment successful. This technique has been successfully used to fabricate samples with large area back gates, which have been used to make independent contact to the top and bottom QWs [61]. At the time of writing, a QPC sample was being fabricated using this technique.

6.2 Short Quantum Wires on DQWs

Quantum wires on single 2DEGs have also received considerable attention in the last decade [109], with effects such as universal conductance fluctuations and Aharonov-Bohm

oscillations being studied. Tunneling from quantum wires to 2DEGs has been studied in both single 2DEGs [113] and in DQWs [68]. Coupled quantum wires on DQWs, on the other hand, have received very little theoretical attention [114, 115] and no experimental attention that we are aware of.

In short quantum wires formed on DQWs and subject to a magnetic field ($B_{||}$) parallel to the growth plane and perpendicular to the direction of current flow, Lyo has predicted a gigantic enhancement of the conductance may be observed [114]. For the conductance enhancement to occur, the quantum wires must be fairly narrow and have nearly equal widths so that only the lowest subband in each quantum wire is occupied, similar to the QPCs in the last section. The magnetic field again shifts the 1D dispersion curves of each quantum wire with respect to each other. Due to coupling, these curves anticross and an energy gap opens, as sketched in Fig. 6.8.

The conductance enhancement occurs due to a suppression of the intra-wire back scattering. In coupled quantum wires, the scattering rate is proportional to $|\langle\varphi_n(z)|V|\varphi_m(z)\rangle|^2$, where $\varphi_{n,m}(z)$ are the isolated QW wavefunctions, n,m = 1,2 index the isolated QWs and V is the confinement potential [114]. When the Fermi level is outside the energy gap (E_{F1} in Fig. 6.8), the dominant back scattering (indicated by dashed lines) occurs within a single quantum wire. Here, the intra-wire scattering has a rate that is proportional to $|\langle\varphi_n(z)|V|\varphi_n(z)\rangle|^2$, and is therefore fairly large. The inter-wire back scattering (indicated by solid lines), on the other hand, is much weaker because its rate is proportional to $|\langle\varphi_n(z)|V|\varphi_m(z)\rangle|^2$, where n ≠ m. This scattering rate is much smaller due to the smaller overlap between $\varphi_n(z)$ and $\varphi_m(z)$. When the Fermi level is in the energy gap (E_{F2} in Fig. 6.8), the intra-wire scattering is suppressed and only the weak inter-wire back scattering is possible. Due to the suppressed back scattering, the conductance increases by several orders of magnitude when the Fermi level is in the energy gap.

The quantum wires and QPCs have very similar dispersion curves but are predicted to behave very differently. The main physical difference between these devices is the channel length. In the QPCs, L is much shorter than the mean free path (ℓ) and the transport is ballistic. While in the quantum wires, L must be $\approx> \ell$ to see the conductance enhancement, since there must initially be intra-wire scattering in order to see its suppression by adding $B_{||}$. In typical DQW samples, $\ell \approx 5$ μm. Due to the requirement of comparable widths of the top and bottom quantum wires, the EBASE technique must be used for these samples. This technique also allows the widths to be varied so the wires can be tuned to have only

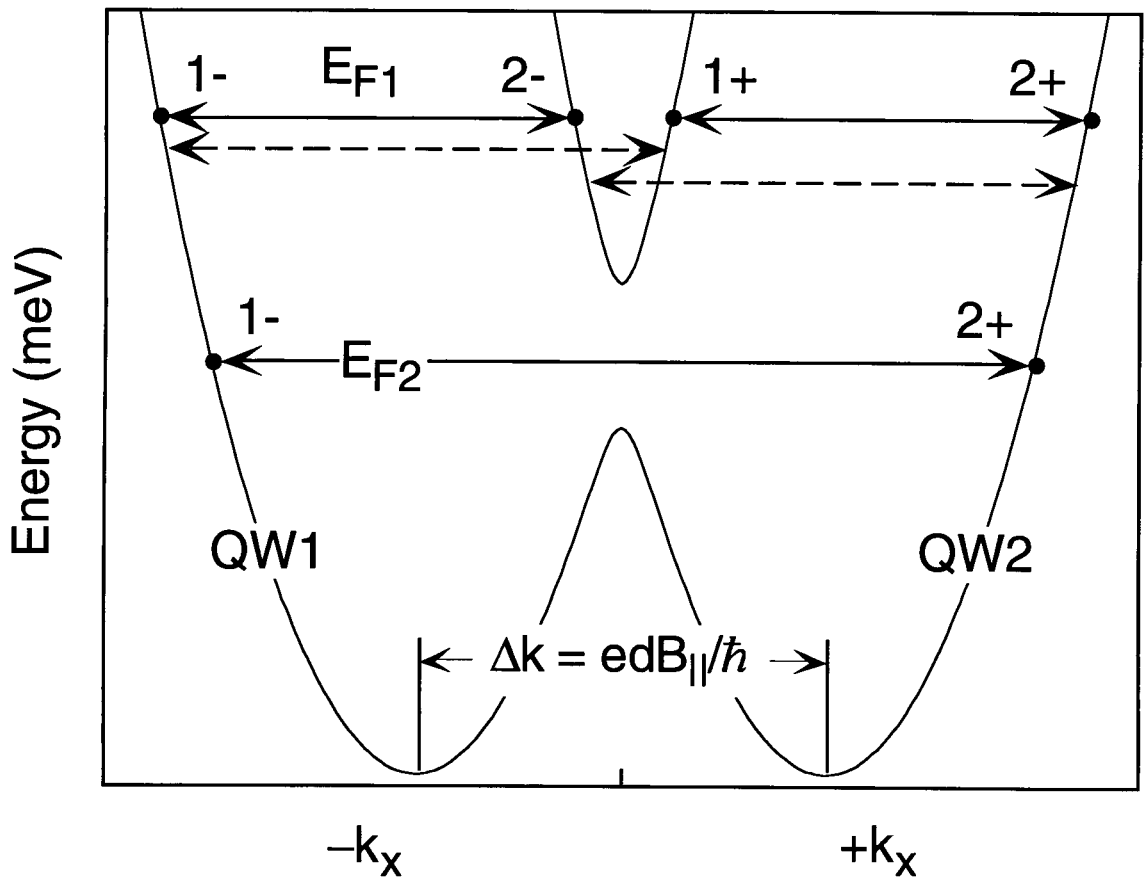

Fig. 6.8 Sketch of the 1D dispersion curve of the coupled quantum wires in $B_{||}$. The lines indicate back scattering between the Fermi points which are shown as dots. The dashed lines are offset in energy for clarity. The +,- signs indicate slopes of the dispersion and the numbers 1,2 indicate which QW the wavefunction resembles.

one subband occupied. The samples could also be fabricated using *in situ* low energy gallium ion beam damage to define the wires [116, 80]. However, the wires fabricated using this technique are not tunable. At the time of writing, quantum wire samples for this experiment are in the process of being fabricated using the EBASE technique.

7. SUMMARY AND FUTURE WORK

Over the last several years interest in double quantum wells has been increasing rapidly. Much of this interest stems from the additional degree of electronic freedom, found in DQWs that is not present in single 2DEGs. The present work has focused on electron transport in double quantum wells subject to magnetic fields applied parallel to the QWs. The first part of this chapter summarizes the experiments done in this thesis and highlights the main conclusions drawn from this work. The second part of the chapter suggests future experiments that could be done using double quantum wells.

7.1 Summary of Work Completed

The samples used in this work are all closely coupled DQWs, most with $\Delta_{SAS} \approx 1$ - 3 meV and one extremely closely coupled sample with $\Delta_{SAS} \approx 7.6$ meV. The experiments that were done can be divided into three groups: (1) distortions in the dispersion curve and Fermi surface caused by $B_{||}$, (2) formation of Landau levels and magnetic breakdown on this distorted dispersion curve due to the addition of $B_{\perp}$, and (3) related transport phenomena in 1D structures on DQWs subject to $B_{||}$.

In the first group of experiments, the in-plane conductance of closely coupled DQWs is measured as a function of $B_{||}$. Two sharp features are observed in the conductance: first a maximum, followed closely by a minimum. These results are in excellent agreement with calculations by Lyo. These features occur as the edges of a partial energy gap in the dispersion curve cross the chemical potential. The energy gap results from an anticrossing of the individual QW dispersion curves that are shifted with respect to one another by $B_{||}$. The distortions in the dispersion curve cause deviations in the density of states, Fermi velocity, and electron effective mass. The evolution of the features with gate bias can be used to determine Δ_{SAS}. We also investigated the anisotropy of the features in $G_{||}$ with

respect to the direction of the electric field. The theory of Vasko and Raichev [93] showed good agreement with the measured data. Finally, the electron effective mass of the dominant **k**-space orbit was measured by adding a small perpendicular component of magnetic field to the in-plane field and analyzing the resulting magnetoresistance oscillations. For one sample, the dominant orbit was the smaller lens-shaped orbit, which exhibited an m^* much less than m^*_{GaAs}, while in another specially designed sample, only the peanut-shaped orbit was present, which exhibited an m^* much greater than m^*_{GaAs}. Again, there was excellent agreement between the experiment and calculations by Lyo.

The second set of experiments examined the resistance of two closely coupled DQW samples as a function of both $B_{||}$ and $B_{\perp}$. In this work, $B_{||}$ shifted the QW dispersion curves causing the energy gap to form and $B_{\perp}$ caused Landau level formation and magnetoresistance oscillations for each branch of the Fermi surface. We observed three separate sets of Landau levels corresponding to three different types of Fermi surface orbits. The first set comes from the smaller, lens-shaped orbit, which has a low effective mass and becomes less populated with increasing $B_{||}$. The second set comes from the larger, peanut-shaped orbit, which has a high effective mass and becomes more populated with increasing $B_{||}$. As a result, sweeping $B_{||}$ induces multiple crossings of the Landau levels from the two orbits at the chemical potential. The third set of Landau levels, which are independent of $B_{||}$, result from magnetic breakdown of the Fermi surface. Magnetic breakdown occurs when electrons tunnel in **k**-space between the peanut and lens orbits to form circular orbits corresponding to the separate uncoupled QWs. A semiclassical calculation of the Landau level spectrum, taking into account the $B_{||}$-dependence of both the mass and Fermi energy of each orbit, shows excellent agreement with the data. Finally, the Fourier spectra of the data as a function of $1/B_{\perp}$ for constant $B_{||}$ further supports the lens and peanut model of the Fermi surface.

The last set of experiments investigated one-dimensional structures on closely coupled double quantum wells. The goal of these experiments was to see the effects of an

anticrossing of the 1D dispersion curves as a function of in-plane magnetic field. The structures studied were quantum point contacts. Here, a step decrease in conductance is expected when the chemical potential is in the energy gap followed by a step increase when the gap moves above the chemical potential. We also studied short quantum wires, where a conductance enhancement is predicted when the chemical potential is in the energy gap due to a strong suppression of back scattering. QPCs were fabricated using top surface depletion gates only. This resulted in a very narrow QPC in the top layer and a very wide QPC in the bottom layer. Thus the top QPC has a very low conductance and the bottom QPC has a very high conductance and, in retrospect, it is not surprising that the conductance steps were not observed in these samples. A technique to fabricate samples with split-gates on both the top surface and on the bottom surface has been developed, but the fabrication of samples using this method has not yet been completed. Samples for the coupled quantum wire experiments are also presently undergoing fabrication using this method.

7.2 Suggestions for Future Work

With improvements in epitaxial growth techniques and sample processing techniques (EBASE, FIB, etc.), the amount of research in coupled double quantum wells will continue to increase. There is a wide variety of work that can be done in this system, including device development, extensions to the work of this thesis, and experiments in other areas involving DQWs.

Two possible device applications for DQWs are as quantum tunneling transistors and far-infrared (FIR) detectors. One proposed transistor is the double electron layer tunneling transistor (DELTT) [16]. In this device, electrons are injected into one QW, tunnel into the second, and are collected, while a gate is used to control the tunneling by moving the DQW in or out of balance. Independent ohmic contact to the top and bottom QWs are essential

for this device to work and they can be fabricated using the EBASE technique. Prototypes have been demonstrated with peak-to-valley ratios of 50:1 [16].

An FIR detector utilizing photon-assisted tunneling from one QW to the other can also be envisioned. Again top and back gates are used to give independent contact to the two layers. A source/drain bias is applied across the device which raises the upper QW dispersion curve above that of the bottom QW and above the Fermi energy. When the bottom QW absorbs a photon of appropriate energy, the photon completes the energy and momentum conservation and allows an electron to tunnel to the top QW which contributes to the tunneling current. The frequency response of this device would be narrow band because the dispersion curves are surface parabloids and not volume parabloids as in the 3D case. The absorption energy is also tunable either by changing the bias on a control gate or by changing the source/drain bias.

One possible extension of the present work is to continue studying magnetic breakdown in DQWs in tilted fields. For this work to be successful, a technique for measuring the breakdown field B_O must be developed. If B_O can be accurately measured as a function of $B_{||}$, meaningful comparison with existing theory on magnetic breakdown in DQWs will be possible. One possibility is to use the data of Chapter 5 and develop a method for computing the Fourier power over different intervals of $B_\perp$ and seeing where magnetic breakdown sets in. Another possibility is to vary the Fermi energy with the sample in fixed $B_{||}$ and $B_\perp$. As the Fermi energy is lowered, oscillations in the resistance occur as Landau levels in the various orbits are depopulated, similar to results in other systems [103, 104]. The difficulty with DQWs is that a top gate only varies the density of the top QW and thus distorts the DQW dispersion curve. For DQWs, top and back gates will have to be biased *together* to change the electron densities of both QWs while keeping them in balance and preserving the shape of the dispersion curve. Performing gate sweeps at constant $B_{||}$ and different values of $B_\perp$ should allow an accurate determination of B_O. The EBASE

technique is ideal for fabricating samples with back gates close to the bottom QW for this experiment.

Other possible extensions of the present work are experiments on 1D structures on DQWs. The present work showed that top and back gates are needed for experiments on QPCs and quantum wires in DQWs, and that the EBASE technique will work very well for fabricating these samples. The experiments described in Chapter 6 could be performed, along with a variety of experiments to explore the coupling between the 1D subbands.

Finally, other areas involving DQWs can be explored. One area that is getting more experimental attention is coupled electron-hole systems on DQWs. Theorists have been working on this subject for more than 20 years [117 -119] where excitonic ground states and excitonic superfluidity have been predicted.

BIBLIOGRAPHY

[1] S. M. Sze, Physics of Semiconductor Devices, Wiley, New York (1981).

[2] L. Geppert, "Technology 1996; Solid State," IEEE Spectrum, 33 (1) 51 (1996).

[3] J. A. Swanson, "Physical versus Logical Coupling in Memory Systems," IBM J. Res. Develop. 4, 305 (1960).

[4] R. Landauer, "Irreversibility and Heat Generation in the Computing Process," IBM J. Res. Develop. 5, 183 (1961).

[5] R. W. Keyes, "Miniaturization of electronics and its limits," IBM J. Res. Develop. 32, 24 (1988).

[6] C. A. Mead "Scalingof MOS Technology to Submicrometer Feature Sizes," J. of VLSI Signal Processing 8, 9 (1995).

[7] N. Yokoyama, S. Muto, K. Imamura, M. Takatsu, T. Mori, Y. Sugiyama, Y. Sakuma, H. Nakao, and T. Adachihara, "Quantum Functional Devices for Advanced Electronics" Solid State Electronics 40, 505 (1996).

[8] S. Datta, M. R. Melloch, S. Bandyopadhyay, and M. S. Lundstrom, "Proposed structure for large quantum interference effects," Appl. Phys. Lett., 48, 487 (1986); F. Capasso and S. Datta, "Quantum electron devices," Phys. Today 43(2), 74 (1990).

[9] J. N. Randall, "A lateral-resonant-tunneling universal quantum-dot cell," Nanotechnology 4, 41 (1993).

[10] C. S. Lent, P. D. Tougaw, and W. Porod, "Bistable saturation in coupled quantum dots for quantum cellular automata," Appl. Phys. Lett. 62, 714 (1993).

[11] P. D. Tougaw and C. S. Lent, "Logical devices implemented using quantum cellular automata," J. Appl. Phys. 75, 1818 (1994).

[12] U. Meirav and E. B. Foxman, "Single-electron phenomena in semiconductors," Semicond. Sci. Technol. 10, 255 (1995).

[13] H. van Houten, C. W. J. Beenakker, and B. J. van Wees, "Quantum Point Contacts," in Semiconductors and Semimetals, ed. M. A. Reed, Academic Press, New York (1992).

[14] J. R. Tucker, "Complementary digital logic based on the 'Coulomb blockade'," J. Appl. Phys. 72, 4399 (1992).

[15] R. W. Keyes, "Electronics in Large Systems," in Molecular Electronics and Molecular Electronic Devices, ed. K. Sienicki, CRC Press, Boca Raton (1993).

[16] Personal Communication, J. A. Simmons, Sandia National Laboratories, MS 1415 P.O. Box 5800, Albuquerque, NM 87185-1415 USA (505-844-8402).

[17] Y. Ohno, M. Tsuchiya, and H. Sakaki, "Gigantic negative transconductance and mobility modulation in a double-quantum-well structure via gate-controlled resonant coupling," Appl. Phys. Lett. 62, 1952 (1993).

[18] H. H. Tsai, Y. K. Su, H. H. Lin, R. L. Wang, and T. L. Lee, "P-N Double Quantum Well Resonant Interband Tunneling Diode with Peak-to-Valley Current Ratio of 144 at Room Temperature," IEEE Electron Device Letters 15, 357 (1994).

[19] T. Ando, A. B. Fowler, and F. Stern, "Electronic Properties of Two-Dimensional Systems," Rev. Mod. Phys. 54, 437 (1982).

[20] M. J. Kelly, Low-Dimensional Semiconductors: Materials, Physics, Technology, and Devices, Clarendon Press, Oxford (1995).

[21] C. Weisbuch and B. Vinter, Quantum Semiconductor Structures: Fundamentals and Applications, Academic Press, New York (1991).

[22] V. Swaminathan and A. T. Macrander, Materials Aspects of GaAs and InP Based Structures, Prentice Hall, Englewood Cliffs (1991).

[23] S. Adachi, "GaAs, AlAs, and $Al_xGa_{1-x}As$: Material Parameters for Use in Research and Device Applications," J. Appl. Phys. 58, R1 (1985).

[24] H. C. Chui, B. E. Hammons, J. A. Simmons, N. E. Harff, and M. E. Sherwin, "High Quality Single and Double Two-Dimensional Electron Gases Grown by Metalorganic Vapor Phase Epitaxy," Appl. Phys. Lett. 67, 1911 (1995).

[25] H. C. Chui, B. E. Hammons, N. E. Harff, J. A. Simmons, and M. E. Sherwin, "2×10^6 cm^2/V s Electron Mobility by Metalorganic Chemical Vapor Deposition with Tertiarybutylarsine," Appl. Phys. Lett. 68, 208 (1996).

[26] F. Stern, "Self-Consistent Results for n-type Si Inversion Layers," Phys. Rev. B 5, 4891 (1972).

[27] N. W. Ashcroft and N. D. Mermin, Solid State Physics, Holt, Rinehart and Winston, New York (1976).

[28] S. E. Koonin, Computational Physics, Addison-Wesley, New York (1986).

[29] W. E. Spicer, I. Lindau, P. Skeath, C. Y. Su, and P. Chye, "Unified Mechanism for Schottky-Barrier Formation and III-V Oxide Interface States," Phys. Rev. Lett. 44, 420 (1980).

[30] K. Ensslin, D. Heitmann, M. Dobers, K. von Klitzing, and K. Ploog, "Electrical Depopulation of Double Quantum Wells," Phys. Rev. B 39, 11179 (1989).

[31] S. K. Lyo, "Transport and Level Anticrossing in Strongly Coupled Double Quantum Wells with In-Plane Magnetic Fields," Phys. Rev. B 50, 4965 (1994).

[32] C. Cohen-Tannoudji, B. Diu, and F. Laloë, Quantum Mechanics, John Wiley & Sons, New York (1977).

[33] S. Datta, Electronic Transport in Mesoscopic Systems, Cambridge University Press, Cambridge (1995).

[34] R. E. Prange and S. M. Girvin (eds.), The Quantum Hall Effect, Springer-Verlag, New York (1987).

[35] K. von Klitzing, G. Dorda, and M. Pepper, "New Method for High-Accuracy Determination of the Fine-Structure Constant Based on Quantized Hall Resistance," Phys. Rev. Lett. 45, 494 (1980).

[36] D. C. Tsui, H. L. Störmer, and A. C. Gossard, "Two-Dimensional Magnetotransport in the Extreme Quantum Limit," Phys. Rev. Lett. 48, 1559 (1982).

[37] K. von Klitzing, "The Quantized Hall Effect," Rev. Mod. Phys. 58, 519 (1986).

[38] T. Chakraborty and P. Pietiläinen, The Fractional Quantum Hall Effect: Properties of an Incompressible Quantum Fluid, Springer Series in Solid-State Sciences, Vol. 58. Springer-Verlag, Berlin (1988).

[39] G. S. Boebinger, H. W. Jiang, L. N. Pfeiffer, and K. W. West, "Magnetic-Field-Driven Destruction of Quantum Hall States in a Double Quantum Well," Phys. Rev. Lett. 64, 1793 (1990).

[40] A. S. Plaut, A. Pinczuk, B. S. Dennis, J. P. Eisenstein, L. N. Pfeiffer, and K. W. West, "Light-Scattering Determination of Electron Tunneling Gaps in Double Quantum Wells," Solid-State Electronics 40, 291 (1996).

[41] A. S. Plaut, A. Pinczuk, B. S. Dennis, J. P. Eisenstein, L. N. Pfeiffer, and K. W. West, "Observation of Many-Body Interactions of Electrons in Coupled Double Quantum Wells," Surf. Sci. 362, 158 (1996).

[42] H. L. Störmer, J. P. Eisenstein, A. C. Gossard, W. Wiegmann, and K. Baldwin, "Quantization of the Hall Effect in an Anisotropic Three-Dimensional Electronic System," Phys. Rev. Lett. 56, 85 (1986).

[43] L. N. Pfeiffer, K. W. West, J. P. Eisenstein, K. W. Baldwin, and P. Gammel, "Multiquantum Well Structure With an Average Electron Mobility of 4.0×10^6 cm^2/V s," Appl. Phys. Lett. 61, 1211 (1992).

[44] J. P. Eisenstein, G. S. Boebinger, L. N. Pfeiffer, K. W. West, and Song He, "New Fractional Quantum Hall State in Double-Layer Two-Dimensional Electron Systems," Phys. Rev. Lett. 68, 1383 (1992).

[45] G. S. Boebinger, Pfeiffer, and K. W. West, "Direct Observation of an Electronic Phase Transition in a Double Quantum Well," Phys. Rev. B 45, 11391 (1992).

[46] S. Q. Murphy, J. P. Eisenstein, G. S. Boebinger, L. N. Pfeiffer, and K. W. West, "Many-Body Integer Quantum Hall Effect: Evidence for New Phase Transitions," Phys. Rev. Lett. 72, 728 (1994).

[47] A. H. MacDonald, P. M. Platzman, and G. S. Boebinger, "Collapse of Integer Hall Gaps in a Double-Quantum-Well System," Phys. Rev. Lett. 65, 775 (1990).

[48] L. Brey, "Energy Spectrum and Charge-Density-Wave Instability of a Double Quantum Well in a Magnetic Field," Phys. Rev. Lett. 65, 903 (1990).

[49] T. Chakraborty and P. Pietiläinen, "Fractional Quantum Hall Effect at Half-Filled Landau Level in a Multiple-Layer Electron System," Phys. Rev. Lett. 59, 2784 (1987).

[50] D. Yoshioka, A. H. MacDonald, and S. M. Girvin, "Fractional Quantum Hall-Effect in 2-Layered Systems," Phys. Rev. B 39, 1932 (1989).

[51] S. He, X. C. Xie, S. Das Sarma, and F. C. Zhang, "Quantum Hall-Effect in Double-Quantum-Well Systems," Phys. Rev. B 43, 9339 (1991).

[52] T. Jungwirth and A. H. MacDonald, "Correlations, Compressibility, and Capacitance in Double-Quantum-Well Systems in the Quantum Hall Regime," Phys. Rev. B 53, 9943 (1996).

[53] Y. W. Suen, J. Jo, M. B. Santos, L. W. Engel, S. W. Hwang, and M. Shayegan, "Missing Integral Quantum Hall Effect in a Wide Single Quantum Well," Phys. Rev. B 44, 5947 (1991).

[54] Y. W. Suen, L. W. Engel, M. B. Santos, M. Shayegan, and D. C. Tsui, "Observation of a $\nu = 1/2$ Fractional Quantum Hall State in a Double-Layer Electron System," Phys. Rev. Lett. 68, 1379 (1992).

[55] G. S. Boebinger, A. Passner, L. N. Pfeiffer, and K. W. West, "Measurement of Fermi-Surface Distortion in Double Quantum Wells from In-Plane Magnetic Fields," Phys. Rev. B 43, 12673 (1991).

[56] J. Hu and A. H. MacDonald, "Electronic Structure of Parallel Two-Dimensional Electron Systems in Tilted Magnetic Fields," Phys. Rev. B 46, 12554 (1992).

[57] See "Physics of Quantum Electron Devices," in Springer Series in Electronics and Photonics, Vol. 28, ed. F. Capasso, Springer, Berlin (1990).

[58] J. Smoliner, W. Demmerle, G. Berthold, E. Gornik, G. Weimann, and W. Schlapp, "Momentum Conservation in Tunneling Processes between Barrier-Separated 2D-Electron-Gas Systems," Phys. Rev. Lett. 63, 2116 (1989).

[59] J. P. Eisenstein, L. N. Pfeiffer, and K. W. West, "Field-Induced Resonant Tunneling between Parallel Two-Dimensional Electron Systems," Appl. Phys. Lett. 58, 1497 (1991).

[60] J. P. Eisenstein, L. N. Pfeiffer, and K. W. West, "Independently Contacted Two-Dimensional Electron Systems in Double Quantum Wells," Appl. Phys. Lett. 57, 2324 (1990).

[61] M. V. Weckwerth, J. A. Simmons, N. E. Harff, M. E. Sherwin, M. A. Blount, W. E. Baca, and H. C. Chui, "Epoxy Bond And Stop-Etch (EBASE) Technique Enabling Backside Processing of (Al)GaAs Heterostructures," Superlattices and Microstructures 20, 561 (1996).

[62] E. H. Linfield, G. A. C. Jones, D. A. Ritchie, and J. H. Thompson, "The Fabrication of a Back-Gated High Electron-Mobility Transistor: A Novel-Approach using MBE Regrowth on an In Situ Ion-Beam Patterned Epilayer," Semicond. Sci. Tech. 8, 415 (1993).

[63] J. P. Eisenstein, T. J. Gramila, L. N. Pfeiffer, and K. W. West, "Probing a Two-Dimensional Fermi Surface by Tunneling," Phys. Rev. B 44, 6511 (1991).

[64] J. A. Simmons, S. K. Lyo, J. F. Klem, M. E. Sherwin, and J. R. Wendt, "Submicron Control of 2D-2D Magnetotunneling in Double-Well Heterostructures," Phys. Rev. B 47, 15741 (1993).

[65] S. K. Lyo and J. A. Simmons, "Linear-Response Theory of Inter-Quantum-Well Tunneling in a Double-Well Structure with In-Plane Magnetic Fields," J. Phys.: Condens. Matt. 5, L299 (1993).

[66] J. P. Eisenstein, L. N. Pfeiffer, and K. W. West, "Coulomb Barrier to Tunneling between Parallel Two-Dimensional Electron Systems," Phys. Rev. Lett. 69, 3804 (1992).

[67] K. M. Brown, N. Turner, J. T. Nicholls, E. H. Linfield, M. Pepper, D. A. Ritchie, and G. A. C. Jones, "Tunneling between Two-Dimensional Electron Gases in a Strong Magnetic Field," Phys. Rev. B 50, 15465 (1994).

[68] B. Kardynal, E. H. Linfield, D. A. Ritchie, K. M. Brown, C. H. W. Barnes, G. A. C. Jones, and M. Pepper, "Equilibrium Tunneling between Two-Dimensional and Quasi-One-Dimensional Electron Gases in Devices Fabricated by In Situ Ion Beam Lithography," Appl. Phys. Lett. 68, 826 (1996).

[69] A. Palevski, F. Bertram, F. Capasso, L. Pfeiffer, and K. W. West, "Resistance Resonance in Coupled Potential Wells," Phys. Rev. Lett. 65, 1929 (1990).

[70] A. Kurobe, I. M. Castleton, E. H. Linfield, M. P. Grimshaw, K. M. Brown, D. A. Ritchie, M. Pepper, and G. A. C. Jones, "Resonant Resistance Enhancement in Double-Quantum-Well GaAs-$Al_xGa_{1-x}As$ Heterostructures," Phys. Rev. B 50, 8024 (1994).

[71] Y. Ohno, M. Tsuchiya, T. Matsusue, T. Noda, and H. Sakaki, "Non-uniform Resonant Coupling Effect on 2D Electron Transport in Delta-Doped Double Quantum Well Structures," Surf. Sci. 305, 322 (1994).

[72] Y. Ohno, H. Sakaki, and M. Tsuchiya, "Quenching of Resonance-Induced Resistance in Double-Quantum Wells in the Presence of In-Plane Magnetic Fields," Phys. Rev. B 49, 11492 (1994).

[73] Y. Berk, A. Kamenev, A. Palevski, L. N. Pfeiffer, and K. W. West, "Resonance Magnetoresistance of Coupled Quantum Wells," Phys. Rev. B 51, 2604 (1995).

[74] T. J. Gramila, J. P. Eisenstein, A. H. MacDonald, L. N. Pfeiffer, and K. W. West, "Mutual Friction between Parallel Two-Dimensional Electron Systems," Phys. Rev. Lett. 66, 1216 (1991).

[75] P. M. Solomon, P. J. Price, D. J. Frank, and D. C. La Tulipe, "New Phenomena in Coupled Transport between 2D and 3D Electron-Gas Layers," Phys. Rev. Lett. 63, 2508 (1989).

[76] U. Sivan, P. M. Solomon, and H. Shtrikman, "Coupled Electron-Hole Transport," Phys. Rev. Lett. 68, 1196 (1992).

[77] H. Rubel, A. Fischer, W. Dietsche, K. von Klitzing, and K. Eberl, "Interaction Effects between Coupled Two-Dimensional Electron-Hole Systems," in Proceedings of the 23rd International Conference on the Physics of Semiconductors, World Scientific Publishing Co., River Edge, New Jersey (1996).

[78] X. K. Huang, G. Bazan, and G. H. Bernstein, "Observation of Supercurrent Drag between Normal-Metal and Superconducting Films," Phys. Rev. Lett. 74, 4051 (1995).

[79] K. Bollweg, T. Kurth, D. Heitmann, E. Vasiliadou, P. Grambow, and K. Eberl, "Coupled Modes and Filling Factor Dependent Edge Potentials in Double-Layered Antidot Arrays," Surf. Sci. 361/362, 766 (1996).

[80] M. Field, C. G. Smith, M. Pepper, K. M. Brown, E. H. Linfield, M. P. Grimshaw, D. A. Ritchie, and G. A. C. Jones, "Coulomb Blockade as a Noninvasive Probe of Local Density of States," Phys. Rev. Lett. 77, 350 (1996).

[81] B. Kardynal, C. H. W. Barnes, E. H. Linfield, D. A. Ritchie, K. M. Brown, G. A. C. Jones, and M. Pepper, "A Direct Measurement of the Band Structure of a One-Dimensional Surface Superlattice," Phys. Rev. Lett. 76, 3802 (1996).

[82] Y. Ohno and H. Sakaki, "Gate-Controlled Modulation of Electronic States and Conductance in Coupled Quantum Wells having an In-Plane Periodic Potential," Solid-State Electronics 40, 303 (1996).

[83] R. E. Williams, Gallium Arsenide Processing Techniques, Washington, D. C., Artech House (1984).

[84] A. S. Sachrajda, Y. Feng, R. P. Taylor, R. Newbury, P. T. Coleridge, J. P. McCaffrey, "The Topological Tranisition from a Corbino to Hall Bar Geometry," Superlattices and Microstructures 20, 651 (1996).

[85] D. C. Cook, Electrical Characterization of GaAs Materials and Devices, Wiley, New York (1989).

[86] N. E. Harff, J. A. Simmons, and J. F. Klem, "Extreme Field-Induced Cyclotron Mass Variations in Coupled Double Quantum Wells," Solid State Electronics 40, 29 (1996).

[87] Personal Communication, S. K. Lyo, Sandia National Laboratories, MS 0601 P.O. Box 5800, Albuquerque, NM 87185-0601 USA (505-844-3718).

[88] J. A. Simmons, S. K. Lyo, N. E. Harff, and J. F. Klem, "Conductance Modulation In Double Quantum Wells Due To Magnetic Field-Induced Anticrossing," Phys. Rev. Lett. 73, 2256 (1994).

[89] N. E. Harff, J. A. Simmons, S. K. Lyo, J. E. Schirber, J. F. Klem, and S. M. Goodnick, "Giant Effective Mass Deviations Near The Magnetic Field-Induced Minigap In Double Quantum Wells," in Proceedings of the 22nd International Conference on the Physics of Semiconductors, World Scientific Publishing Co., River Edge, New Jersey (1995).

[90] J. A. Simmons, N. E. Harff, and J. F. Klem, "Observation Of Extreme Field-Induced Mass Deviations In Double Quantum Wells," Phys. Rev. B 51, 11156 (1995).

[91] S. K. Lyo, "Giant Field-Induced Variation of the Cyclotron Mass in Coupled Two-Dimensional Electron Gases," Phys. Rev. B 51, 11160 (1995).

[92] S. K. Lyo, J. A. Simmons, N. E. Harff, and J. F. Klem, "Novel Magnetic-Field-Induced Minigap Transport in Coupled Double Quantum Wells," in Proceedings of Chancellor's Symposium, Riverside, California, (1995)..

[93] O. E. Raichev and F. T. Vasko, "Conductivity of Coupled Quantum Wells Under In-Plane Magnetic Field," Phys. Rev. B 53, 1522 (1996).

[94] T. Ihn, H. Carmona, P. C. Main, L. Eaves, and M. Henini, "Magnetic-Field-Induced Resonant Tunneling in Parallel Two-Dimensional Systems," Phys. Rev. B 54, R2315 (1996).

[95] P. T. Coleridge, R. Stoner, and R. Fletcher, "Low-Field Transport-Coefficients in GaAs/$Ga_{1-x}Al_xAs$ Heterostructures," Phys. Rev. B 39, 1120 (1989).

[96] L. Smrcka, P. Vasek, J. Kolácek, T. Jungwirth, and M. Cukr, "Cyclotron Effective Mass of 2D Electron Layer at GaAs/$Al_xGa_{1-x}As$ Heterojunction Subject to In-Plane Magnetic Fields," Phys. Rev. B 51, 18011 (1995).

[97] L. Smrcka and T. Jungwirth, "In-Plane Magnetic-Field-Induced Anisotropy of 2D Fermi Contours and the Field-Dependent Cyclotron Mass," J. Phys.: Condens. Matter 6, 55 (1994).

[98] M. A. Blount, J. A. Simmons, N. E. Harff, S. K. Lyo, and M. J. Hafich, "Magnetoconductance and Effective Mass of an Extremely Closely Coupled Double Quantum Well," to appear in Bull. Am. Phys. Soc. 42 (1997).

[99] N. E. Harff, J. A. Simmons, S. K. Lyo, J. F. Klem, G. S. Boebinger, L. N. Pfeiffer, and K. W. West, "Magnetic Breakdown and Landau Level Spectra of a Tunable Double Quantum Well Fermi Surface," accepted to Phys. Rev. B, Rapid Communications (1997).

[100] N. E. Harff, J. A. Simmons, J. F. Klem, G. S. Boebinger, L. N. Pfeiffer, and K. W. West, "Observation of Magnetic Breakdown in Double Quantum Wells," Superlattices and Microstructures 20, 595 (1996).

[101] E. I. Blount, "Bloch Electrons in a Magnetic Field," Phys. Rev. 126, 1636 (1961).

[102] M. H. Cohen and L. M. Falicov, "Magnetic Breakdown in Crystals," Phys. Rev. Lett. 7, 231 (1961).

[103] T. G. Matheson and R. J. Higgins, "Tunneling in Tilted Si Inversion Layers," Phys. Rev. B 25, 2633 (1982) and references therein.

[104] T. Evelbauer, A. Wixforth, and J. P. Kotthaus, "One-Dimensional Minigaps in Inversion Layer Subbands on High Index Surfaces of InSb," Z. Phys. B - Condensed Matter 64, 69 (1986).

[105] P. Streda and A. H. MacDonald, "Magnetic Breakdown and Magnetoresistance Oscillations in a Periodically Modulated Two-Dimensional Electron Gas," Phys. Rev. B 41, 11892 (1990).

[106] A. B. Pippard, "Quantization of Coupled Orbits in Metals," Proc. R. Soc. London Ser. A 270, 1 (1962).

[107] Personal Communication, S. K. Lyo, Sandia National Laboratories, MS 0601 P.O. Box 5800, Albuquerque, NM 87185-0601 USA (505-844-3718).

[108] LabVIEW Analysis VI Reference Manual, National Instruments Corp., Austin (1993).

[109] C. W. J. Beenakker and H. van Houten, "Quantum Transport in Semiconductor Nanostructures," in Solid State Physics Vol. 44, ed. H. Ehrenreich and D. Turnbull, Academic Press, New York (1991).

[110] B. J. van Wees, H. van Houten, C. W. J. Beenakker, J. G. Williamson, L. P. Kouwenhoven, D. van der Marcel, and C. T. Foxon, "Quantized Conductance of Point Contacts in a Two-Dimensional Electron Gas," Phys. Rev. Lett. 60, 848 (1988).

[111] D. A. Wharam, T. J. Thornton, R. Newbury, M. Pepper, H. Ahmed, J. E. F. Frost, D. G. Hasko, D. C. Peacock. D. A. Ritchie, and G. A. C. Jones, "One-Dimensional Transport and Quantization of Ballistic Resistance," J. Phys. C 21, L209 (1988).

[112] Personal Communication, S. K. Lyo, Sandia National Laboratories, MS 0601 P.O. Box 5800, Albuquerque, NM 87185-0601 USA (505-844-3718).

[113] C. C. Eugster, J. A. del Alamo, M. R. Melloch, and M. J. Rooks, "1D-to-2D Tunneling in Electron Waveguides," Phys. Rev. B 48, 15057 (1993).

[114] S. K. Lyo, "Magnetic Quenching of Back Scattering in Coupled Double Quantum Wires: Giant Mobility Enhancement," J. Phys.: Condens. Matter 8, L703 (1996).

[115] M. H. Degani and I. C. da Cunha Lima, "Tunneling in Double Quantum Well Wires," in Bull. Am. Phys. Soc. 41 (1996).

[116] K. M. Brown, E. H. Linfield, D. A. Ritchie, G. A. C. Jones, M. P. Grimshaw, and A. C. Churchill, "Fabrication of Independent Contacts to 2 Closely Spaced 2-Dimensional Electron Gases using Molecular-Beam Epitaxy Regrowth and *In-Situ* Focused Ion-Beam Lithography," J. Vac. Sci. Technol. B 12, 1293 (1993).

[117] D. Jérome, T. M. Rice, and W. Kown, "Excitonic Insulator," Phys. Rev. 158, 462 (1967).

[118] I. O. Kulik and S. I. Shevchenko, "Excitonic 'Superfluidity' in Low-Dimensional Crystals," Solid State Comm. 21, 409 (1977).

[119] V. I. Yudson, "Charged 'Few-Electron—Single Spatially Separated Hole' Complexes in a Double Quantum Well near a Metal Plate," Phys. Rev. Lett. 77, 1564 (1996).